Fakultät für Medizin

Characterization of microRNA-365 in cardiac rhythm control

Dena Esfandyari Shahvar

Vollständiger Abdruck der von der Fakultät für Medizin der Technischen Universität München zur Erlangung des akademischen Grades einer

Doktorin der Naturwissenschaften (Dr. rer. nat.)

genehmigten Dissertation.

Vorsitzender: Prof. Dr. Dirk H. Busch

Prüfer der Dissertation:

1. Prof. Dr. Dr. Stefan Engelhardt
2. Prof. Dr. Angelika Schnieke
3. Prof. Dr. Sabine Steffens

Die Dissertation wurde am 07.02.2022 bei der Technischen Universität München eingereicht und durch die Fakultät für Medizin am 12.07.2022 angenommen.

Abbreviations

AAV	adeno-associated virus
ACM	Arrhythmogenic cardiomyopathy
AF	atrial fibrillation
AGO	Argonaute / Ago clade protein
AP	Action potential
APD	Action potential duration
AVN	Atrioventricular node
bp	base pair
bpm	Beats per minute
CAD	Coronary artery disease
cAPD	Corrected action potential duration
cDNA	complementary DNA
CM	cardiac myocyte
CMV	Cytomegalovirus
Ctrl	control
DAD	Delayed after depolarization
DAPI	4', 6-diamidino-2-phenylindole
DCM	dilated cardiomyopathy
df	Double fluorescent
DGCR8	DiGeorge syndrome critical region 8
DNA	deoxyribonucleic acid
dNTP	deoxyribonucleoside triphosphate
DTT	1,4-dithiothreitol
E.coli	*Escherichia coli*
EAD	Early after depolarization
ECG	Electrocardiogram
ECM	extracellular matrix
EDTA	ethylenediaminetetraacetic acid
FP	Field potential
FRET	Förster (Fluorescence) Resonance Energy Transfer
GEVI	Genetically Encoded Voltage Indicator
GFP	green fluorescent protein
HCM	Hypertrophic cardiomyopathy
HEK	human embryonic kidney
hiPSC	Human induced pluripotent stem cell
hiPSC-CM	Human induced pluripotent stem cell cardiac myocytes
ICD	Implantable Cardioverter Defibrillator
IF	immunofluorescence
LA	Left atrium
LNA	locked nucleic acid
lncRNA	long non-coding RNA
LQTS	Long QT syndrome
LV	left ventricle
MI	myocardial infarction
miRNA	microRNA
MOI	Multiplicity of infection
mRNA	messenger RNA
NRCM	neonatal rat cardiac myocytes
nt	nucleotide(s)
PBS	phosphate buffered saline
PCR	polymerase chain reaction
PFA	paraformaldehyde
pre-miRNA	precursor miRNA
pri-miRNA	primary miRNA
qRT-PCR	quantitative real time polymerase chain reaction
RA	Right atrium
rcf	Relative centrifugal force
RFP	red fluorescent protein
RISC	RNA induced silencing complex
RNA	ribonucleic acid
RNAi	RNA interference
RNA-seq	RNA sequencing
RV	right ventricle
SAN	Sinoatrial node
SCD	Sudden cardiac death
scRNA-seq	Single cell RNA sequencing
SEM	standard error mean
siRNA	small interfering RNA
SQTS	Short QT syndrome
TAC	Transverse aortic constriction
TdP	Torsades de pointes
UTR	untranslated region
VSFP	Voltage-sensitive fluorescent protein
WGA	wheat germ agglutinin

Table of Contents

List of Figures

List of Tables

1 Introduction

1.1 Cardiac electrical activity and arrhythmia

Cardiovascular diseases are responsible for approximately 17 million deaths per year globally, and sudden cardiac death (SCD) accounts for about 25% of these cases (**Figure 1.1**). Arrhythmia, defined as irregularities of cardiac electrical activity, is one of the main underlying causes of SCD, especially in the younger population[1–3]. Despite considerable advancements in prevention and treatment strategies, such cardiovascular complications remain the leading cause of mortality worldwide[4]. Therefore, the development of new therapeutic interventions is demanded. To this end, an in-depth understanding of the molecular mechanisms of cardiac excitation in physiological and pathological conditions is crucial.

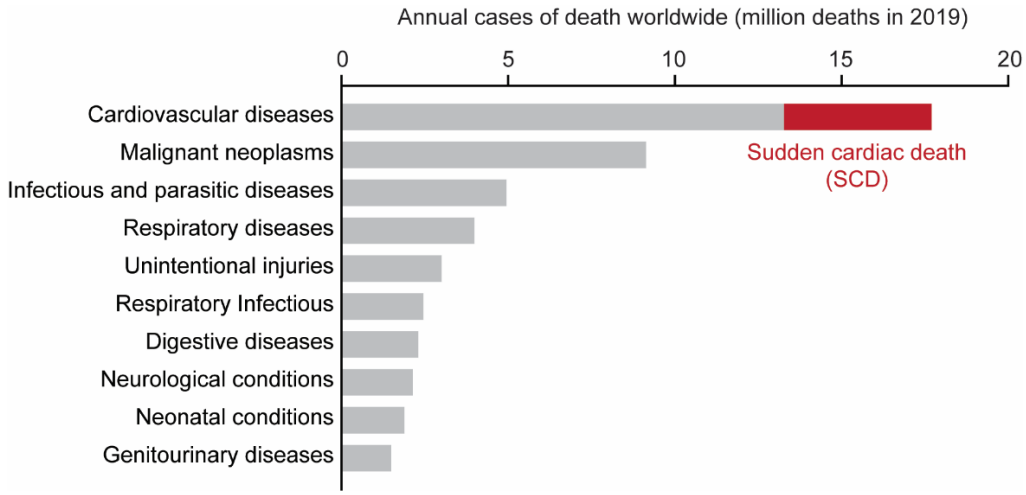

Figure 1.1. The leading causes of death worldwide. The top 10 major causes of mortality worldwide according to the data provided in the "Global Health Estimates 2019" report by World health organization[5]. Cardiovascular diseases are the leading cause of death, and sudden cardiac death significantly contributes to cardiovascular mortality.

1.1.1 Cardiac electrophysiology in healthy myocardium

1.1.1.1 Cardiac action potential

The synchronous and rhythmic contraction of the heart is essential for the pumping of blood throughout the body. Cardiac function is coordinated by a precise generation of excitation impulses in pacemaker regions of the heart and propagation of the electrical signal through the conduction system, which results in the contractile activity of the cardiac muscle. This process is known as excitation-contraction coupling (ECC) in the myocardium[6–9]. In the early embryonic stages, all cardiac cells represent pacemaking activity; however, only a small specialized fraction of cells maintain this capability after birth[10,11]. In the adult heart, the electrical activity mainly originates in the sinoatrial (SA) node, spreads through the atria, and

reaches the atrioventricular junction. This electrically insulated fibrous tissue prevents the direct and random spread of the electrical impulse from the atria to the ventricles[12,13]; therefore, the electrical signals converge at the atrioventricular (AV) node and propagate through the bundle of His to the left and right bundle branches, Purkinje fibers, and throughout the ventricles[6,14]. This follows by consecutive contractions of the atria and ventricles. The electromechanical activity of the heart relies on the action potentials (APs) generated in individual cardiac myocytes, which, similar to all excitable cells, is a result of ions trafficking across the cell membrane through specific ion channels. A healthy myocardial cell has a negative membrane potential at the resting phase. Inward Na^+ and Ca^{2+} currents result in depolarization of the myocytes while outward K^+ currents repolarize the membrane to resting condition. Heterogeneous expression, organization, and function of ion transport machinery among different regions of the human heart result in distinct AP waveforms and durations (**Figure 1.2**)[6,7,15]. Even within the ventricles, there are differences in AP characteristics across different layers of the ventricular wall (midmyocardium, endo- and epicardium). For instance, midmyocardium myocytes represent the longest AP duration[16].

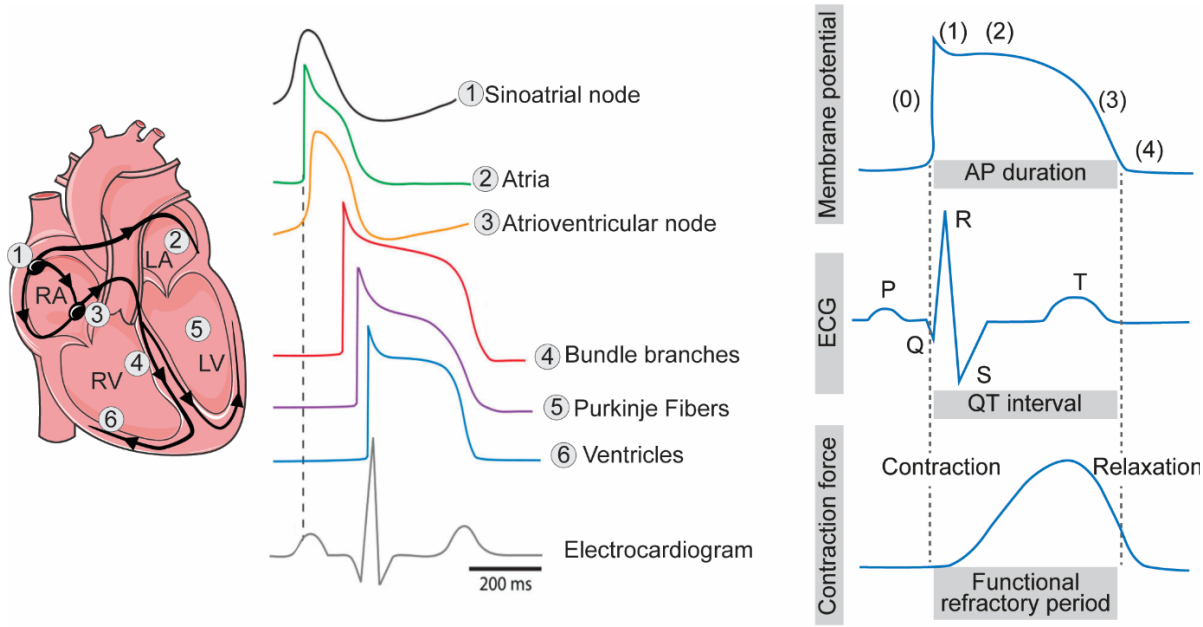

Figure 1.2. Electrical and mechanical activity of human myocardium. Schematic of the electrical conduction system in the human heart (black route), the action potential (AP) waveforms in different regions, and their contribution to different phases of a representative surface electrocardiogram (ECG, left, adapted from [16], RA, right atrium; LA, left atrium; RV, right ventricle; LV, left ventricle). The correlation between the electrical and mechanical activity of human ventricular myocardium (right). The relationship between the AP, the QT interval in a surface ECG, and the muscle contraction in the human ventricular myocardium.

Changes in membrane potential can be recorded using surface electrocardiography. In an electrocardiogram (ECG), the P-wave represents the depolarization of the atria, while the QRS complex and the T-wave depict the depolarization and repolarization of the ventricular myocytes, respectively. For instance, the full span of an AP in ventricular myocytes directly

correlates with the QT interval on an ECG and the contractile force development in the ventricular myocardium (**Figure 1.2**)[17,18].

A typical AP in ventricular myocytes consists of 5 phases. At resting conditions, the cells have a membrane potential of approximately -80 to -90 mV due to a higher concentration of Na^+ and Ca^{2+} outside the cell and a higher cytosolic concentration of K^+ ions (**Figure 1.3**). An electrical stimulation, e.g., from adjacent cells, triggers depolarization by an initial activation (opening) of voltage-gated sodium channels and a rapid influx of Na^+ into the cardiac myocytes (inward I_{Na} current). If the stimulus is strong enough to cause the membrane potential to reach higher than -65 mV, the inward sodium channels will be activated, leading to further influx of Na^+ and initiation of the AP in an all-or-none manner. The upstroke at Phase 0 of the AP brings the membrane potential to 20-40 mV. At the tissue level, this accompanies by the beginning of the systolic activity of the myocardium[19–22].

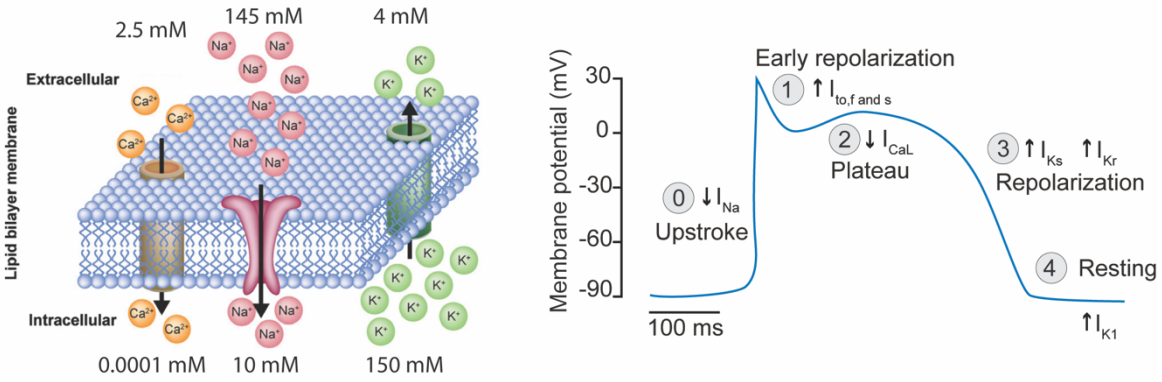

Figure 1.3. Molecular basis of AP formation in the heart. Scheme showing the concentration of Na^+, Ca^{2+}, and K^+ cations in the two sides of a cardiac cell membrane at resting equilibrium (left). In the resting condition, the membrane potential is about -90 mV. However, an electrical stimulus activates the voltage-gated Na^+ channels, and the resulting inward Na^+ currents (I_{Na}) initiate the AP (right panel) by depolarizing the membrane and breaking this equilibrium (phase 0, upstroke). This follows by a sequential activation and inactivation of Ca^{2+} and K^+ ion channels, which direct the early repolarization (phase 1), plateau (phase 2), and final repolarization (phase 3) phases of the cardiac AP. Finally, the membrane reaches the resting potential (phase 4) again until the next stimulus triggers the next AP. Outward currents are depicted as outward arrows, whereas inward currents are shown with downward arrows. Adapted from[15,23].

The AP continues by a rapid inactivation of Na^+ channels and early repolarization (Phase 1) of the membrane due to a brief and slow opening of voltage-gated K^+ channels that mediate transient outward potassium currents (I_{to}). After slight repolarization, the transient K^+ channels start to close with different inactivation (closing) kinetics (fast inactivating, $I_{to,\,f}$ and slow inactivating $I_{to,\,s}$ currents). Membrane depolarization at Phase 0 also activates the voltage-gated L-type Ca^{2+} channels, which mediate a steady influx of Ca^{2+} ($I_{Ca,\,L}$) into the cells. The function of these channels reaches a maximum in Phase 2 of the AP, where at the same time, rapidly-activating delayed rectifying K^+ currents (I_{Kr}) and slowly-activating delayed rectifying currents (I_{Ks}) come into play, resulting in a delicate balance between repolarizing outward K^+

currents and depolarizing inward Ca^{2+} currents. This phase of the AP is known as the plateau phase (Phase 2), which lasts for 180-200 ms at a membrane potential of 0–20 mV and is the primary determinant of AP duration in ventricular myocytes. The influx of Ca^{2+} is a prerequisite for activation of ryanodine receptors in the sarcoplasmic reticulum membrane, Ca^{2+}-dependent Ca^{2+} release, and thereby excitation-contraction coupling. As the Ca^{2+} channels inactivate at the end of the plateau phase, continuous I_{Kr} and I_{Ks} currents and the addition of inwardly rectifying K^+ currents (I_{K1}) repolarize the membrane further (Phase 3) and bring the membrane potential back to the resting equilibrium (Phase 4). This accompanies by the diastolic function of the muscle. The resting phase continues until the next electrical stimulus triggering the initiation of the next AP[6,21,23–25]. The ion channels contributing to each current during a human ventricular AP are listed in **Table 1.1**.

1.1.1.2 Cardiac ion channels

Two fundamental characteristics of all ion channels are selective permeability to specific ions and their gating properties. Typically, ion channels are comprised of pore-forming subunits (α-subunits, **Figure 1.4**) that provide selective binding sites for ions and transport them across the lipid bilayer of the membrane at ultrarapid rates (10^6 ions/s). The ion channels' selectivity depends on the size, valency, and hydration energy of the ions they transport. In the myocardium, Na^+, $Ca^{2+,}$ and K^+ channels are highly selective, whereas gap junctional channels are classified as non-selective. For instance, Na^+ channels are 10-12 times more selective to Na^+ than K^+ although both cations have the same valency, or Ca^{2+} channels are 1000 times more permeable to Ca^{2+} compared to K^+ or Na^+. The opening and closing of ion channels, also known as gating, result from conformational changes in the channel protein structure. This can happen in response to changes in membrane voltage (voltage-gated ion channels), in response to a specific ligand (ligand-dependent ion channels), or as a result of mechanical stimuli (mechanosensitive ion channels). The transition of the channel proteins between the activated (open) and the inactivated (close) forms occurs with a kinetic that is characteristic of each ion channel. Apart from the pore-forming α-subunits, other auxiliary subunits (usually denoted as β, δ, …) have been identified for many of the ion channels. These proteins can interact with cytosolic or extracellular linker parts of the α-subunits and regulate the gating kinetics and the membrane density of the ion channels (**Table 1.1**)[7,8,22,26,27].

Although in humans, cardiac myocytes have a minimal proliferation and regeneration capacity and thereby last for the entire lifespan, the half-life of a typical ion channel is only a few hours. Thus, to maintain a stable electromechanical phenotype in cardiac myocytes and in response to pathological stimuli, the “channelome” of these cells is continuously being replenished.

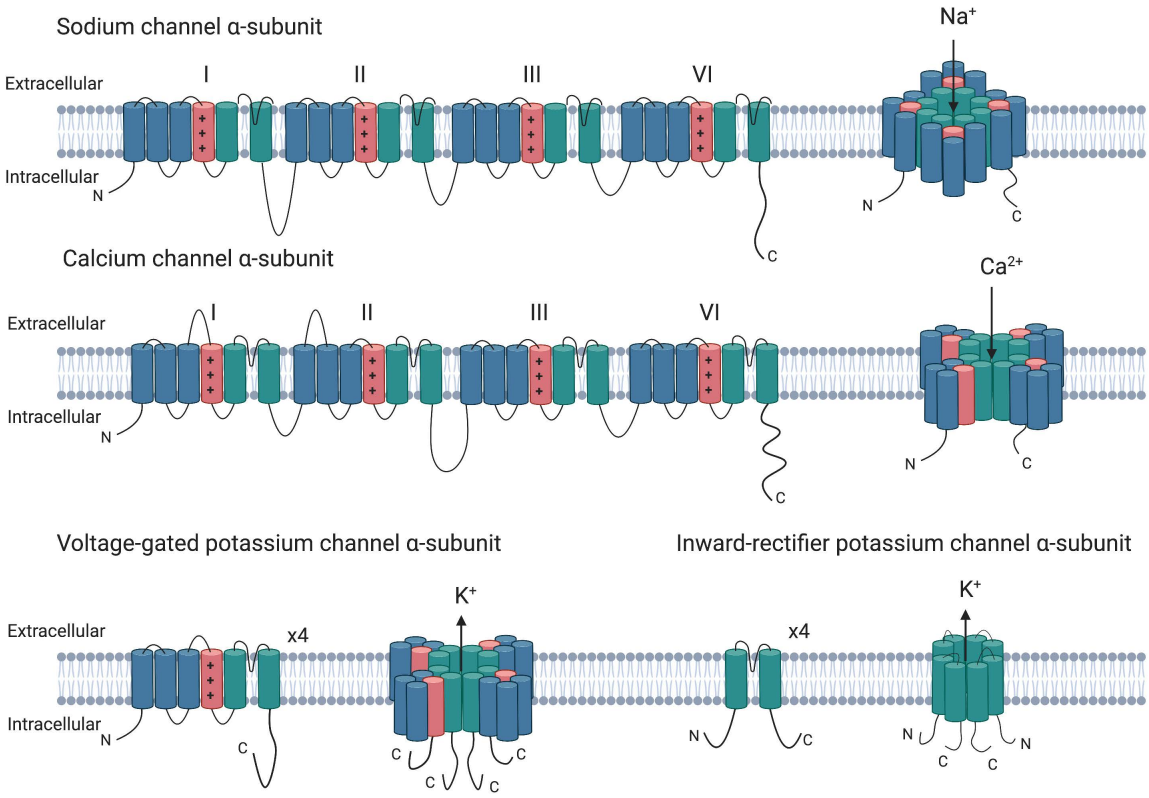

Figure 1.4. Pore-forming subunits of cardiac ion channels. Primary sequences and membrane topology of the pore-forming α-subunits of cardiac Na^+, Ca^{2+}, and K^+ ion channels. Voltage-gated Na^+ and Ca^{2+} channels are comprised of 4 domains (I-VI) that form one pore. Each domain consists of 6 α-helical transmembrane repeats. Voltage-gated and inwardly rectifying K^+ channels, on the contrary, are tetrameric complexes. Each constructing monomer contains 6 or 2 transmembrane α-helices in voltage-gated and inward-rectifier K^+ channels, classifying them as 6TM and 2TM tetramers, respectively. The direction of ion transfer is depicted as inward and outward arrows. Redrawn after [8,15,22,28] using Biorender.

Expression and function of cardiac ion channels are under a tight regulation at different processing steps, namely transcription, translation, protein modification, oligomerization, and channel assembly, transport to the cell membrane (forward trafficking), and finally internalization, degradation, and recycling (retrograde trafficking)[8,29–31]. For instance, β-adrenergic signaling enhances both I_{Kr} and I_{Ks} currents by protein phosphorylation and subsequent recruitment of auxiliary domains (minK and AKAP9, **Table 1.1**)[32]. Another example is the functional link between the main three repolarizing currents, I_{Kr}, I_{Ks}, and I_{K1}, which together form a safeguard mechanism to prevent the loss of repolarizing power. This mechanism is known as the repolarization reserve and represents as compensatory upregulation of each of these three currents or, more precisely, their α-subunits (KCNH2, KCNQ1, and KCNJ2, respectively), when the other one is reduced[33,34].

Family	Subunit	Gene	Current	AP phase	Accessory subunits
Voltage-gated inward ion channels					
Na_v	**$Na_v1.5$**	***SCN5a***	**I_{Na}**	Phase 0	β1 (*SCN1B*) β2 (*SCN2B*) β3 (*SCN3B*)
	$Na_v1.1$	*SCN1A*	Unknown		
	$Na_v1.3$	*SCN3A*	Unknown		
Ca_v	**$Ca_v1.2$**	***CACNA1C***	**I_{CaL}**	Phase 2	β2 (*CACNB2*) α2δ-1,2,3 (*CACNA2D1,2,3*) γ4,6,7 (*CACNG4,6,7*)
	$Ca_v1.3$	*CACNA1D*	Unknown		
	$Ca_v2.1$	*CACNA1A*	Unknown		
	$Ca_v3.1$	*CACNA1G*	I_{CaT}		
Voltage-gated potassium channels					
K_v1	**$K_v1.1$**	***KCNA1***	**$I_{to,s}$**	Phase 1	K_vβ1 (*KCNAB1*) K_vβ2 (*KCNAB2*) K_vβ3 (*KCNAB3*)
	$K_v1.2$	*KCNA2*	Unknown		
	$K_v1.4$	***KCNA4***	**$I_{to,s}$**	Phase 1	
	$K_v1.7$	***KCNA7***	**$I_{to,s}$**	Phase 1	
K_v3	$K_v3.1$	*KCNC1*	Unknown		
	$K_v3.3$	*KCNC3*	Unknown		
K_v4	$K_v4.1$	*KCND1*	Unknown		
	$K_v4.2$	***KCND2***	**$I_{to,f}$**	Phase 1	KchIP2 (*KCNIP2*) *DPP6* *DPP10*
	$K_v4.3$	***KCND3***	**$I_{to,f}$**	Phase 1	
K_v7	**$K_v7.1$**	***KCNQ1***	**I_{Ks}**	Phase 3	Mink (*KCNE1*) MiRP1,2,4 (*KCNE2,3,5*)
K_v11	$K_v7.2$	*KCNQ2*	Unknown		
	K_v11	***KCNH2***	**I_{Kr}**	Phase 3	MiRP1,2 (*KCNE2,3*)
Inwardly rectifying potassium channels					
Kir1	Kir1.1	*KCNJ1*	Unknown		
Kir2	**Kir2.1**	***KCNJ2***	**I_{K1}**	Phase 3, 4	
	Kir2.2	***KCNJ12***	**I_{K1}**	Phase 3, 4	
	Kir2.3	***KCNJ4***	**I_{K1}**	Phase 3, 4	
	Kir2.4	*KCNJ14*	Unknown		
Kir3	**Kir3.1**	***KCNJ3***	**I_{KAch}**	Phase 4	
	Kir3.4	***KCNJ5***	**I_{KAch}**	Phase 4	
Kir6	Kir6.1	*KCNJ8*	Unknown		
	Kir6.2	***KCNJ11***	**I_{KATP}**	Phase 1, 2	

Table 1.1 Diversity of ventricular ion channels. For each of the Na^+, Ca^{2+}, and K^+ ion channels, the pore-forming protein subunits expressed in the ventricular myocardium and their corresponding encoding genes are listed. The isoforms that contribute to the main known currents in ventricular AP are shown in bold. The resulting currents in different phases of a typical AP and the accessory subunits identified to be associated with each ion channel are listed. Adapted from [6–8,22,35]

1.1.2 Electrical disorders of the heart

Cardiac arrhythmia is one of the main contributors to cardiovascular mortality. Arrhythmias are defined as any irregularity in the electrical activity of the heart and thereby, cardiac rhythm, and encompass a wide variety of phenotypes, depending on the location of arrhythmogenicity (supraventricular or ventricular), the alteration in heart rate (lower or higher than normal, also known as bradycardia and tachycardia, respectively), the underlying electrophysiological mechanism (automaticity, triggered activity or reentry), and severity (palpitations or flutter to blockade and fibrillation). Arrhythmias stem from abnormal impulse generation (AP depolarization or repolarization) or conduction due to inherited mutations or acquired malfunctioning of cardiac ion channels or regulators, or as a result of structural heart diseases that interrupt the propagation of AP[7–9,22].

1.1.2.1 Ventricular arrhythmia and sudden Cardiac death

Ventricular arrhythmias, typically observed as tachycardias (VT), are the primary risk factor leading to ventricular fibrillation (VF) and sudden cardiac death (SCD). SCD affects 4-5 million individuals annually and accounts for approximately 25% of all mortalities in the general population[3,36,37]. In adults (> 45 years old), coronary artery disease (CAD), ischemia, and infarction are major risk factors for SCD, whereas in younger populations, typically, inherited cardiac disorders, including primary electric disorders and structural heart diseases, or acquired arrhythmogenic conditions result in SCD. In individuals with inherited structural cardiac diseases, namely the dilated-, hypertrophic- and arrhythmogenic cardiomyopathies (DCM, HCM, and ACM, respectively), and in patients with acquired structural remodeling following an ischemic episode, acute heart failure or infarction, the structural abnormalities such as impaired conduction or ECC due to myocytes disarrays and fibrosis, have been suggested to form the substrate for arrhythmogenesis. Although the exact mechanisms are incompletely understood, the underlying cause of lethality comes down to the arrhythmic events accompanied by these disorders (**Figure 1.5**) [8,38–42].

On the other hand, the primary electrical disorders are defined as arrhythmias occurring in the absence of any structural defects in the myocardium[38,43]. The long QT syndrome (LQTS), short QT syndrome (SQTS), Brugada syndrome, and catecholaminergic polymorphic ventricular tachycardia (CPVT) are different types of such arrhythmias. These disorders are inherited channelopathies, which cause characteristics alterations in ECG patterns and lead to malignant forms of VT and a higher incidence of SCD. The Brugada syndrome is accompanied by dysfunction in multiple ion channels, mainly in the right ventricle, resulting in an elevation of the ST segment on an ECG[44,45]. The CPVT accompanies by mutations in the components of Ca^{2+} handling machinery, which result in abnormal QRS and QT segments of ECG (known as polymorphic VT) and is an important cause of cardiac syncope[46,47].

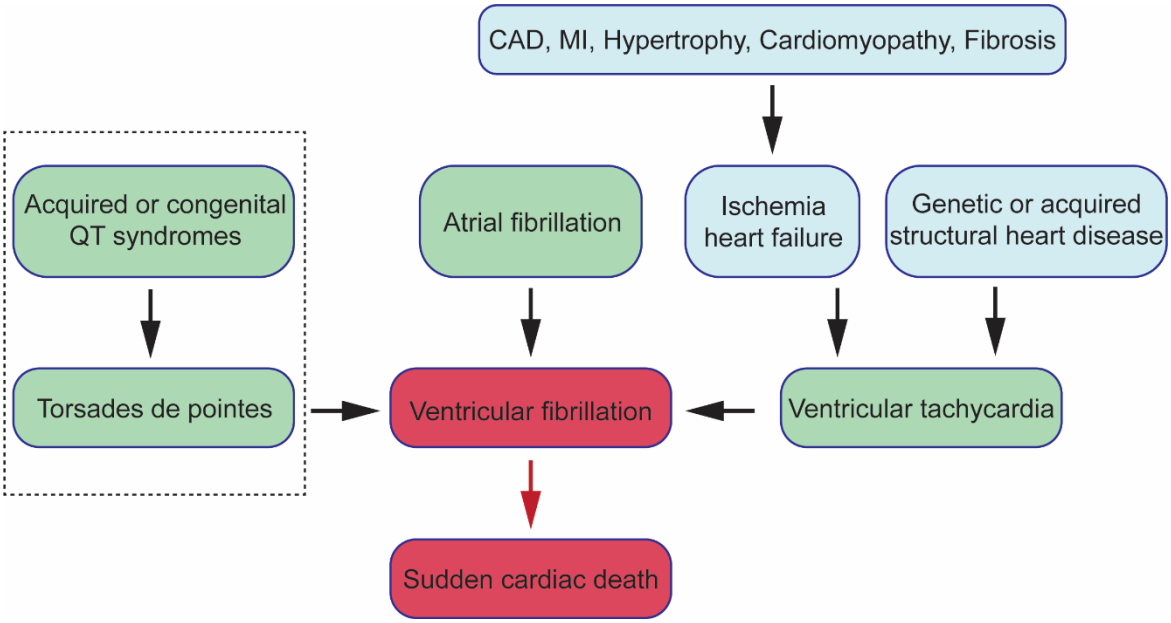

Figure 1.5. Etiology of ventricular arrhythmias and sudden cardiac death. The underlying causes of ventricular fibrillation and SCD are classified as various types of structural heart diseases (depicted in blue), and ion channel irregularities that induce abnormal AP characteristics (depicted in green). These phenotypes can be congenital or occur through acquired conditions. CAD, coronary artery disease; MI, myocardial infarction. Simplified from[4,48] and redrawn after[36].

The LQTS is an inherited cardiac channelopathy that represents as prolonged repolarization of ventricular myocytes and an increased risk of triggered cardiac events (namely, early or delayed afterdepolarizations, EAD, and DADs) and torsade de pointes (TdP), which causes ventricular fibrillation and SCD, in otherwise structurally normal myocardium. First characterized in 1957, LQTS is diagnosed by ECG, where the corrected QT intervals are longer than 500 ms or even longer than 445 ms in the presence of other risk factors such as family history and specific phenotypes after cardiac exercise tests [1,2,25,49]. A prevalence of 0.2-1.5% has been estimated for this type of channelopathies[50,51]. To date, molecular studies suggested more than hundreds of mutations in 17 different genes as an underlying cause of LQTS (**Table 1.2**). These mutations are located in genes coding for ion channel subunits and channel-associated structural proteins and have been implicated in disrupting ion channel protein synthesis, posttranslational processing such as ion channel protein folding, assembly, glycosylation and trafficking to the cell membrane, and ion channels gating or permeation properties. The majority of known mutations are autosomal dominant loss-of-function mutations resulting in a reduction of outward K^+ currents[19,52–57]. These mutations disrupt I_{Ks} and I_{Kr} and account for up to 90% of LQTS patients tested positive for genetic markers. Gain-of-function mutations in pore-forming or accessory subunits of Na^+ channels[58] and the pore-forming subunit of Ca^{2+} channels[59,60] that explain 5-10% of the mutations in genetically positive LQTS cases. Loss-of-function mutations in calmodulin genes (calmodulinophathy)[61,62] and TRDN (encoding Triadin protein)[63] are also responsible for the prolongation of QT interval since these are proteins that regulate Ca^{2+}-dependent inactivation

of Ca^{2+} channels, and their mutation elevates the $I_{Ca,L}$ current. Ankyrin-B is also an essential structural protein that facilitates the localization of ion channel proteins in the cell membrane and sarcoplasmic reticulum. Thus, the clinical phenotypes associated with ANK2 mutations are not limited to LQTS and may lead to severe and lethal arrhythmias[8,64].

In addition to inherited LQTS, certain drugs can also generate a pathologically prolonged AP and even SCD as a side-effect. This phenotype is known as drug-induced LQTS (diLQTS) and is the main reason for the withdrawal of many cardiovascular and non-cardiovascular pharmacotherapies. Mechanistically, inhibition of inward rectifying K+ channels is the primary etiology for diLQTS. However, among different individuals, there is a variation of prolongation and the severity of the reaction to the same LQT-inducing drug, which is thought to be due to more complex underlying genetic causes[65–67]. The SQTS is a highly arrhythmogenic channelopathy that mainly affects younger individuals and manifests as a constant shortening of QT interval (corrected QT < 370 ms), which accompanies by syncope and SCD. The SQTS was first described in 2000 and only in very few families worldwide, and therefore, the molecular studies on this channelopathy are still limited. To date, gain-of-function mutations in the three main K^+ channels[68–70] and loss-of-function mutations in α-, β2-, and α2δ-subunits of the L-type Ca^{2+} channel[71,72] have been linked to SQTS. Rare mutations in SLC4A3 and SCN5A genes have also be linked to a shorter QT interval concomitant with Brugada syndrome implications[73]. However, these mutations have been reported only a minor fraction (23%) of all SQTS patients (**Table 1.2**)[74].

1.1.2.1 Antiarrhythmic interventions

A better understanding of the molecular basis of ventricular arrhythmias had resulted in a significant advancement of the intervention options for the clinical management of such arrhythmias and prevention of SCD. Pharmacotherapy is often the first choice of treatment due to the feasibility of administration and non-invasiveness. To date, many antiarrhythmic drugs have been described that are classified into different classes according to their mechanism of action (**Figure 1.6**). The Class I drugs are Na^+ channel blockers and, depending on the degree of blockage, might induce QT alterations. Quinidine is an example of Class Ia drugs that lead to a substantial blockage of the Na^+ channel and seem to be the only effective medication in prolongation of QT in STQS patients. The Class II of antiarrhythmic drugs, comprised of modulators of the autonomous nervous system, alter the heart rate and, due to their large safety margin and effectiveness, are the first option for managing ventricular arrhythmias. Therapy with beta-blockers has been shown to reduce cardiac events in LQTS (53-64%) and CPVT. The K^+ channel blockers are the Class III of drugs that are mainly effective in case of atrial arrhythmias and not the ventricular ones.

Channelopathy	Affected gene	Mutation	Affected current
Long QT syndromes			
LQT1	*KCNQ1*	AD, LoF	↓ I_{Ks}
LQT2	*KCNH2*	AD, LoF	↓ I_{Kr}
LQT3	*SCN5A*	AD, GoF	↑ I_{Na}
LQT4 (Ank-B syndrome)	*ANK2*	AD, LoF	Multiple currents
LQT5	*KCNE1*	AD, LoF	↓ I_{Ks}
LQT6	*KCNE2*	AD, LoF	↓ I_{Kr}
LQT7 (Andersen-Tawil syndrome)	*KCNJ2*	AD, LoF	↓ I_{K1}
LQT8 (Timothy syndrome)	*CACNA1C*	AD, GoF	↑ $I_{Ca,L}$
LQT9	*CAV3*	AD, GoF	↑ I_{Na}
LQT10	*SCN4B*	AD, GoF	↑ I_{Na}
LQT11	*AKAP9*	AD, LoF	↓ I_{Ks}
LQT12	*SNTA1*	AD, GoF	↑ I_{Na}
LQT13	*KCNJ5*	AD, LoF	↓ I_{KACh}
LQT14	*CALM1*	AD, LoF	↑ $I_{Ca,L}$
LQT15	*CALM2*	AD, LoF	↑ $I_{Ca,L}$
LQT16	*CALM3*	AD, LoF	↑ $I_{Ca,L}$
LQT17 (Triadin knockout syndrome)	*TRDN*	AR, LoF	↑ $I_{Ca,L}$
JLN1	*KCNQ1*	AR, LoF	↓ I_{Ks}
JLN2	*KCNE1*	AR, LoF	↓ I_{Ks}
Short QT syndromes			
SQT1	*KCNH2*	AD, GoF	↑ I_{Kr}
SQT2	*KCNQ1*	AD, GoF	↑ I_{Ks}
SQT3	*KCNJ2*	AD, GoF	↑ I_{K1}
SQT4	*CACNA1C*	AD?, LoF	↓ $I_{Ca,L}$
SQT5	*CACNB2B*	AD?, LoF	↓ $I_{Ca,L}$
SQT6	*CACNA2D1*	AD?, LoF	↓ $I_{Ca,L}$

Table 1.2 Molecular basis of long and short QT syndromes. For each of the Na+, Ca2+ and K+ ion channels LoF, loss of function; GoF, gain of function; AD, autosomal dominant; AR, autosomal recessive; Adapted from 6–8,22,35

The Class IV antiarrhythmic drugs decrease conduction through blockage of Ca^{2+} channels and have limited application in managing severe supraventricular arrhythmias[48,75]. The modern classifications consider additional classes of antiarrhythmic drugs, namely Class 0 (HCM modulators), Class V (mechanosensitive channel modulators), Class VI (gap junction

modulators), and Class VII (upstream target modulators)[76,77]. However, these medications are not always effective in modulating ventricular arrhythmias since the underlying channelopathy is not directly targeted, and furthermore, there is a high degree of unspecific effects on the other channels for each of these drugs. In these cases, more invasive treatments must be perused. For instance, for both LQTS and SQTS, the implantable cardioverter-defibrillator (ICD) is the option of choice, and in LQTS patients with reoccurring syncopal episodes left (or bilateral) cervicothoracic sympathetic denervation is the recommended option. These interventions are effective but are associated with relevant device-related complications[78–80].

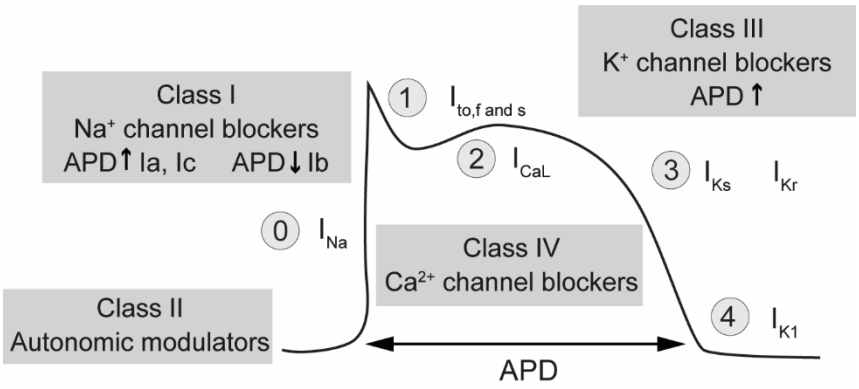

Figure 1.6. Classification of cardiac antiarrhythmic medications. Scheme depicting the classic antiarrhythmic drugs and the corresponding ionic currents affected by each class of these medications.

1.2 MicroRNAs and arrhythmia

Completion of the human genome project and extensive transcriptome analyses revealed that protein-coding genes make up only 2% of the genome and more than 70% of our transcribed genes are non-coding[81–84]. MicroRNAs (miRNA or miRs) are a class of non-coding RNAs distinguished with their small (21-23 nucleotides) size and are shown to repress the expression of their target genes post-transcriptionally[85–87]. The research on this class of non-coding RNAs initiated by the discovery of *lin-4*, a gene in *Caenorhabditis elegans* that encoded a small, non-protein coding RNA with the capability of binding to *lin-14* gene in an antisense complementary manner, repressing its expression and therefore controlling developmental timing in this organism[88,89]. This was followed by another report on RNA-based gene expression regulation, where *let-7* negatively regulated *lin-41* in *C. elegans*[90]. Interestingly, *let-7* was found to be evolutionarily conserved in mammals, leading to the idea that this class of non-coding RNAs might have functional relevance in higher metazoans as well[91]. Since then, miRNAs were recognized as a class of regulatory RNAs[92–94], and thousands of these molecules were identified and characterized as regulators of development, metabolism, cellular differentiation, proliferation, and apoptosis in various tissues of humans and other eukaryotes upon health and disease. Due to their crucial role in the regulation of gene expression, as well feasibility of

manipulation of their intracellular levels, miRNA emerged as an attractive therapeutic venue. In the cardiovascular field, for instance, miRNAs miR-21[95], miR-29[96], miR15b[97], miR199a, miR-328[98], miR-208[99], and miR-206[100] have been translated to large animal models, and *miR-92a* and *miR-132* have already progressed to clinical developments[101].

1.2.1 MicroRNA biogenesis and regulatory mechanism

In metazoans, miRNA genes are often encoded from the non-coding regions of the genome; however, they may also lie within an intron or the untranslated regions of a protein-coding genes[102]. MiRNA genes are canonically transcribed in the nucleus by RNA polymerase II in mammalians. The resulting transcript is known as primary (pri-) miRNA and contains a long hairpin region[103–106]. The double-stranded structure of the hairpin is the substrate for a heterotrimeric endonuclease complex called Microprocessor. This complex is comprised of one molecule of Drosha, which has two RNase III domains, and two molecules of DGCR8 that recognize the hairpin structure and orient the Microprocessor complex to cleave the pri-miRNA hairpin. This cleavage yields in a 60-70 nucleotide long stem-loop structure called the precursor miRNA (pre-miRNA) and is subsequently exported from the nucleus to the cytosol by a nucleocytoplasmic shuttler Exportin 5[107,108]. Once in the cytoplasm, the pre-miRNA is further cleaved by another RNase, Dicer, which removes the loop structure and generates the miRNA duplex. This duplex contains the mature miRNA and its passenger strand (miRNA*)[85,109,110]. The miRNA duplex is then loaded into the Argonaute (AGO) protein, where the miRNA* is driven out and gets degraded, while the mature miRNA strand and the AGO protein form the active RNA-induced silencing complex (RISC)[111,112]. After incorporation in RISC, miRNAs guide the complex toward their target transcripts (**Figure 1.7**).

Complementary binding sites for miRNAs are often found in 3' untranslated regions (3' UTRs) of mRNA molecules. Nucleotides 2-7 at the 5' end of the miRNA are known as the seed region and initially interact with target mRNAs. For a mammalian miRNA to effectively regulate its target, this 6-mer seed matching is often accompanied by one or two additional matchings at miRNA nucleotides 1 or 8, resulting in 7- or 8-mer binding sites[85,113,114]. Depending on the degree of complementarity between a miRNA's seed region and its binding site in the 3' UTR of the target miRNA, two modes of action are reported for RISC-mediated regulation. In case of more extensive complementarity, the AGO protein acts as an endonuclease and cleaves the target mRNA. This repression through slicing the mRNA is also the basis of siRNA-based knockdown strategies[115]. This mode of action is mainly observed in plants, whereas, in humans and other mammals, miRNA-target complementarity is mostly partial. Upon partial pairing between miRNA and target mRNA, the AGO protein recruits a panel of other proteins that either act through destabilization of the target mRNA by deadenylation and shortening of its

polyA tail or by inhibiting mRNA translation or decreasing the efficiency of translation. Both of these phenomena result in repression of target gene expression [85,116,117].

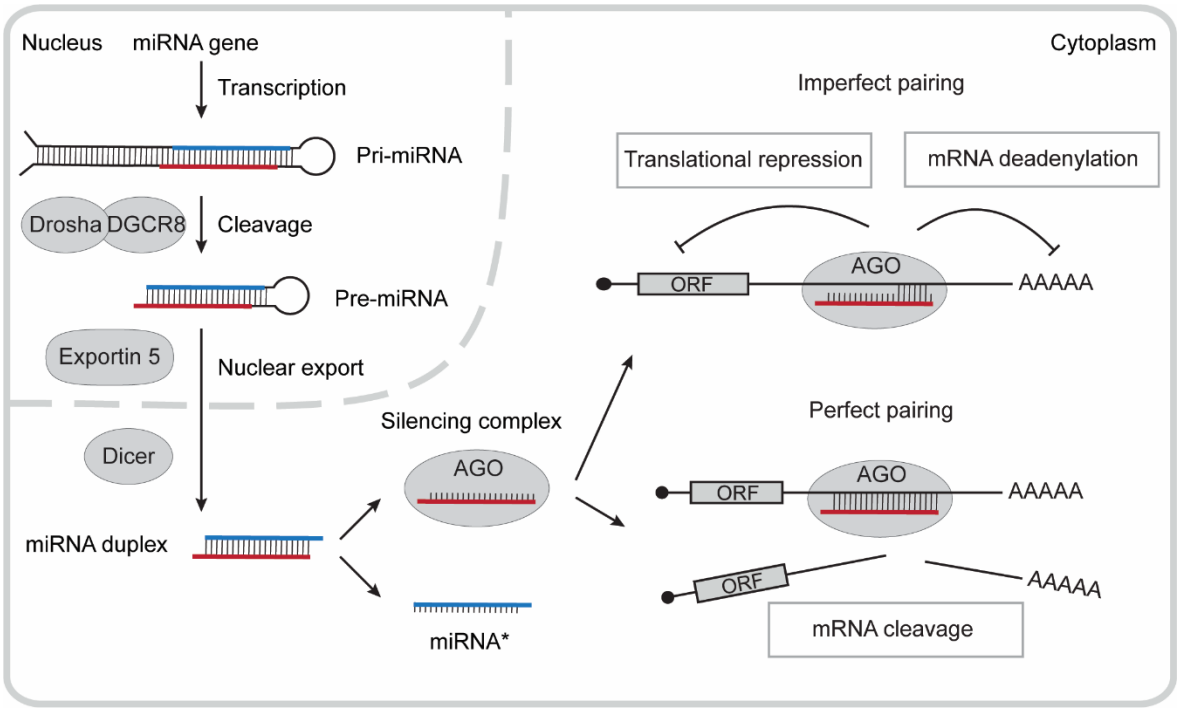

Figure 1.7. Canonical miRNAs Biogenesis and modes of action. The miRNA gene is transcribed by RNA Polymerase II, yielding a stem-loop structure known as the primary (pri)-miRNA. Microprocessor cleaves pri-miRNA, forming the precursor (pre)-miRNA, which is then exported to the cytoplasm by Exportin 5. In the cytoplasm, Dicer cleaves the loop structure of the pre-miRNA, producing the miRNA:miRNA* duplex. The mature miRNA strand (in red) is incorporated into an Argonaute protein (AGO) and form the RISC complex, whereas the miRNA* strand (in blue) is degraded. MiRNA directs the RISC to target mRNAs through the complementary matching of miRNA's seed sequence and miRNA binding sites within the 3' UTR of the target mRNAs. Highly complementary interaction results in mRNA cleavage by AGO (lower right), whereas an imperfect interaction causes translational repression or mRNA destabilization as a result of 5' deadenylation. Redrawn after[85].

Based on their seed sequence, miRNAs are grouped into hundreds of miRNA families, some of which are highly conserved throughout the evolution. Each of these broadly conserved miRNA families has more than 300 7- or 8-mer binding sites within the 3' UTR human mRNA, and approximately 60% of human mRNAs carry binding sites for miRNAs[85,118]. Since miRNA-mRNA targeting is highly dependent on the relatively short miRNA seed sequence, one miRNA may target multiple mRNA targets, and as well, one mRNA may carry binding sites for multiple miRNAs. A high abundance of intracellular miRNA (hundreds to thousands of molecules) is required for effective miRNA-mediated mRNA repression [85,119,120]. MiRNA activity is also impacted by the abundance of target mRNAs and their competition for binding to free miRNA molecules since the higher expression of individual targets may result in de-repression of other targets as a consequence of lowering the number of free miRNAs within the cell. This is known as the competing endogenous RNA hypothesis (ceRNA) [85,120,121].

The identification of miRNA target genes (targetome) involves *in silico* predictions and computational methods based on the complementarity of their seed region and the binding sites within the 3' UTRs, as well as the conservation of miRNA and mRNA targets. To date, several tools are available that implement these approaches[113,122]. In addition, *in vitro* approaches based on RNA-sequencing (RNA-seq) combined with immunoprecipitation of AGO protein crosslinked to miRNA and mRNA proved to be revealing[123,124]. The regulatory role of miRNAs on its targetome can be validated by quantifying the target's mRNA or protein levels and by performing reporter assays (such as luciferase assays or double fluorescent reporter assays)[125].

Many miRNAs are deregulated during diseases, and restoration of their expression can provide a therapeutic strategy. Therefore, various manipulation methods have been developed for robust modulation of the endogenous levels of a miRNA. To inhibit miRNAs, antisense oligonucleotides against miRNAs (antimiRs)[126,127] or miRNA sponges (constructs including multiple miRNA binding sites)[128] can be employed. Synthetic antimiRs are especially effective due to their small size and thereby higher uptake, as well as the feasibility of chemical modifications that provide higher stability against nucleases. For instance, antimiRs with locked nucleic acids (LNA) modification have an increased binding affinity and stability[129,130]. For elevation of miRNA levels, synthetic miRNA mimics have are widely used, Mimics are typically double-stranded RNA molecules with stabilizing modifications, and can incorporate into the RISC complex and imitate the regulatory function of a miRNA[131,132].

1.2.2 MicroRNAs and cardiac arrhythmia

Since their identification, many regulatory roles for miRNAs have been described in homeostasis and pathogenesis of the cardiovascular system. Many reports have shown deregulation of miRNAs in cardiac tissue upon various cardiac pathogenic conditions, such as CAD, hypertrophy, HF, MI, and cardiomyopathies compared to healthy individuals (reviewed in[133–137]). Moreover, the circulating miRNAs in the bloodstream of these patients have been suggested as biomarkers for the diagnosis and prognosis of various cardiovascular diseases[138,139].

Regarding arrhythmias, miRNA-target prediction algorithms[113,140,141] suggest that most cardiac ion channels contain binding sites for miRNAs in their 3' UTR, and therefore, a regulatory role of distinct miRNAs is expected in various aspects of cardiac rhythm control and arrhythmias. Due to the higher prevalence of supraventricular arrhythmias, namely atrial fibrillation (AF), there are more detailed studies on these types of arrhythmias (reviewed in[142–145]). For instance, miR-208b, miR-483, miR-23a, and miR-26a have been reported as circulating RNAs that can be used as biomarkers of AF in different stages of the disease. MiR-29 and miR-21 have been reported to contribute to AF by targeting genes involved in cardiac fibrosis[146,147]. Upregulation

of miR-328 and potential targeting of α- and β1 subunits of the L-type Ca^{2+} channel (CACNA1C and CACNB2) by this miRNA have been reported in the atrial tissue of AF patients[98]. A reduced amount of CACNA1C and KCNJ3 mRNA and protein concomitant with an elevation of miR-30 has been observed in the cardiomyocytes from AF patients[148]. MiR-1, an established cardiac miRNA, is reported to be decreased in AF, resulting in increased levels of I_{K1} current and KCNJ2[149]. On the contrary, miR-1 levels are reported to be increased in the setting of ventricular arrhythmias. This differential expression in atria versus ventricles, next to the vast targetome attributed to miR-1, challenges its application as a therapeutic miRNA[150].

In contrast to AF, only a few miRNAs have been shown to regulate ventricular repolarization and arrhythmias, and even fewer are known to exert this regulation through direct targeting of the relevant ion channels[150,151]. For instance, a reduction of miR-1 and miR-133a, another established cardiac miRNA, has been reported to cause a prolongation of QT interval in mice through modulation of beta-adrenergic signaling and, thereby, indirect activation of L-type Ca^{2+} channels[152]. In contrast, opposite results has been observed in mice with increased miR-133 levels, where QT interval was prolonged due to decreased $I_{to,f}$ currents, and repression of *Kcnip2* gene. However, *Kcnip2* lacks binding sites for miR-133 and the exact mechanism of miR-133-mediated regulation of this gene is unknown[153]. In guinea pig, overexpression of miR-1 and miR-133 has been reported to induce QT prolongation through downregulation of *KCNJ2* (I_{K1})[154]. Upregulation of miR-212 and subsequently downregulation of *KCNJ2* has also been reported in QT prolongations in heart failure[155]. In zebrafish, miR-19 has been associated with ventricular arrhythmia, where deficiency of this miRNA resulted in reduced cardiac contractility and conduction and prolonged AP duration through targeting gap junction mRNAs and KCNE4[156]. The miR-221/222 cluster has also been implicated in hypertrophy-induced arrhythmia in mouse myocardium by targeting CACNA1C and KCNJ5[157].

1.2.3 MicroRNA-365

MiR-365 is a conserved miRNA that, together with miR-193b, creates a distinct miRNA seed family. In humans, miR-365 is located in two genomic loci: hsa-miR-365a on chromosome 16 and hsa-miR-365b on chromosome 17. While the pre-miRNA sequences of hsa-miR-365a and b differ in a few nucleotides, the sequence of the mature functional miRNA is identical and is predicted to target approximately 377 broadly conserved transcripts[158–160]. In humans, the highest expression of miR-365 has been observed in muscle and adipose tissue[161], yet an involvement of miR-365 has also been reported in many biological functions in various tissues and diseases. Sufficient expression of this miRNA is necessary for differentiation and proliferation of chondrocytes and osteogenesis based on *in vitro* studies as well as the reported downregulation of miR-365 in human osteoarthritic cartilage[162–168]. MiR-365 has been reported to be involved in the differentiation and formation of brown adipose tissue in vitro; however,

this could not be confirmed *in vivo* in mice[169–171]. In cancer, deciphering the role of miR-365 is more complex since this miRNA has been reported as both an oncogenic miRNA (oncomiR, e.g., in lung adenocarcinoma, cutaneous squamous cell carcinoma)[172–176] and a tumor suppressor (namely in breast and ovarian cancer, human hepatocellular carcinoma)[177–184]. However, in most of the reports, miR-365 was found to act as a tumor suppressor by inhibiting proliferation and migration and facilitating cell apoptosis[185–187]. MiR-365 is reported to be involved in interleukin-6 (IL6)-mediated inflammation, which is found in the setting of many inflammatory diseases such as coronary atherosclerosis[188] and active tuberculosis[189]. In the central nervous system, miR-365 has been reported to affect the excitability of neurons by targeting *Kcnh2*, the channel responsible for I_{Kr} in the myocardium[190]. In the cardiovascular field, miR-365 was first identified in high-throughput screening for hypertrophic miRNAs. This screening was performed based on an automated cell size assessment in neonatal rat cardiomyocytes (NRCMs), and miR-365 was reported as one of the top pro-hypertrophic miRNAs (**Figure 1.8**)[191]. This finding was substantiated in another study on mice[192]. In humans, miR-365 has been found to be downregulated in endomyocardial biopsies from enterovirus-induced cardiomyopathy [193]. In heart failure patients, miR-365 levels were upregulated in plasma, whereas a downregulation was observed in diseased myocardium compare to non-failing controls [194].

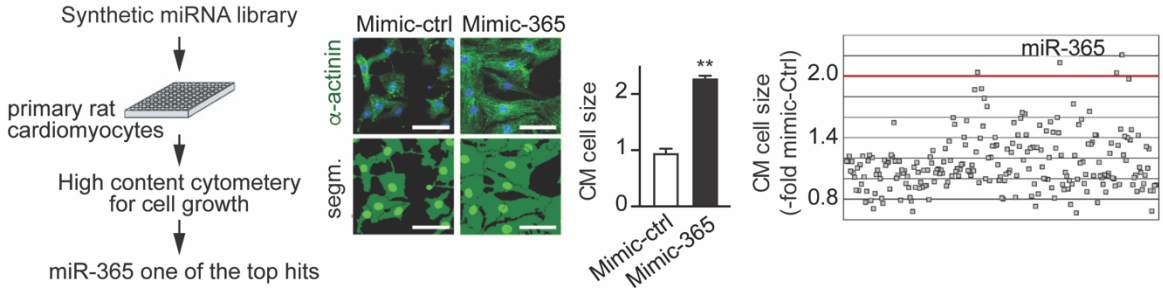

Figure 1.8. The implication of miR-365 in cardiac hypertrophy. A high-throughput phenotypic screening to identify miRNAs involved in cardiac hypertrophy. The neonatal rat cardiomyocytes (NRCMs) were transfected with a synthetic library of 230 miRNA mimic, fixed, and stained with cardiac myocyte marker α-actinin. Subsequently, an automated cell size assessment algorithm was performed, leading to identification of miR-365 as one of the top miRNA mimics inducing hypertrophy. segm., segmentation; CM, cardiac myocyte. Adapted from[191].

1.3 Models to study cardiac arrhythmia

To date, significant progress has been made toward the identification of the genetic, cellular, and molecular basis of cardiac arrhythmias. For instance, the identification and cloning of individual genes encoding for the ion channels pore-forming and auxiliary subunits enabled ion current measurements in different expression systems (*e.g.*, the oocytes of *Xenopus laevis*) and provided important insights into the essential characteristics of cardiac ion channels, such as gating properties and drug sensitivities[195]. This was followed by the ongoing

development of the novel *in vitro*, *ex vivo,* and *in vivo* disease models and AP measurement tools in recent years, which are the prerequisites to fully decipher the complex pathophysiology of cardiac arrhythmias and to evaluate the underlying AP regulatory mechanisms.

1.3.1 Animal models of cardiac arrhythmia

Various animal species have been employed for disease modeling, and such models have significantly contributed to our current knowledge of cardiovascular pathophysiology and arrhythmogenesis. For instance, transverse aortic constriction (TAC) causes left ventricular pressure overload, and subsequently, cardiac hypertrophy. This structural abnormality of the myocardium has been reported in mouse, rat, rabbit, and guinea pig models, and in some cases, increases the susceptibility of the animal to ventricular tachycardia and AF[196–199]. MI is also one of the major risk factors for arrhythmogenesis in humans. Therefore, animal models of MI have also been used for arrhythmia studies. In rodent models, ligation of the left anterior descending (LAD) coronary artery or cryoinjury can induce ventricular ischemia and increased risk of ventricular tachycardia and fibrillation[200,201]. Since rhythm abnormalities are a consequence of the structural remodeling in these animal models, the occurrence and extent of arrhythmogenicity are not consistent.

To model ventricular tachycardia, canine and porcine models have been stimulated with ventricular tachypacing to reach 2-3-fold higher heartbeats per minute (bpm). This approach typically results in repolarization abnormalities in the myocardium of large animal models; however, smaller animals (such as rodents) are typically insensitive[199,202]. A considerable class of arrhythmia models, especially in modeling QT abnormalities such as LQTS, are the transgenic animal models. Predominantly in mice, but also in rabbits, loss- or gain-of-function modifications in ion channel gene loci have been introduced in a heterozygous or homozygous manner, resulting in LQTS-like phenotypes. In mice, *Scn5a*, *Cacna1c,* and *Kcna5* transgenes and *Kcnd2*, *Kcna4*, *Kcnh2*, *Kcnq1*, and *Kcnj2* knockout mice have been characterized to show a variety of QT and AP duration abnormalities (reviewed in[203,204]). In addition to *in vivo* studies, the myocardium of these animal models can be perfused for *ex vivo* studies. *ex vivo* heart preparations (*e.g.*, Langendorff-perfused heart preparations) allow for functional and electrophysiological measurements at the organ level; however, the maintenance is limited to a short time, and the systemic neurohormonal effects on the myocardium are absent[199,205,206].

Although providing a valuable platform for arrhythmia studies, the primary limitations of rodent arrhythmia models are the fundamental electrophysiological and contractile differences compared to the human myocardium (**Figure 1.9**). Substantial differences regarding the heart rate at resting conditions (600 bpm in mouse versus 60 bpm in humans), Ca^{2+} handling properties and ion channel composition (*e.g.,* absence of I_{Ks} and I_{Kr} currents in mice), and consequently, incomparable QT intervals (30-100 ms in mice compared to 400 ms in human),

limit the extrapolation of findings obtained in these models to humans[151,199,207]. Relatively, the AP durations in rabbits resemble more closely to humans. Although the heart rate in rabbits is 2- to 5-fold quicker than humans (130-300 bpm versus 60 bpm), these small animals are considered as suitable models to study repolarization abnormalities. However, genetically modified rabbit models of arrhythmia are not as readily available as the murine ones[208,209].

Larger animal models, such as dogs, pigs, sheep, and non-human primates, recapitulate the structural and functional aspects of human myocardium more closely, making these animals the preferred models for early-stage clinical studies. On the downside, translational failures still occur with large animal models, and the feasibility of experiments in such animals is much lower than rodent models, especially with respect to the availability of transgenic arrhythmia models. Therefore, currently available animal model systems are not capable of fully recapitulating the human cardiovascular system[199,206,210].

1.3.2 Human-based models for arrhythmia studies

Native human myocardial tissue or isolated human cardiac myocytes are ideal platforms for studying the molecular basis of arrhythmogenesis. However, accessing the myocardial tissue from patients with ventricular channelopathies is not only invasive but is almost impossible due to the rare nature of this class of cardiac disorders. Furthermore, the long-term culture of isolated adult cardiac myocytes is very challenging. The discovery of induced pluripotent stem cell (iPSC) technology created a great opportunity for circumventing these issues. In order to generate human iPSCs (hiPSCs), somatic cells can be obtained in a non-invasive manner from blood, skin, fat, or urine specimen and are subsequently reprogrammed to a pluripotent state by introducing pluripotency-inducing genes. Classically, this was achieved by overexpression of *OCT4*, *SOX2*, *KLF4,* and *MYC* genes in the somatic cells using retroviruses[211]; however, novel safer reprogramming approaches have been developed based on non-integrating vectors such as Sendai-viruses (reviewed by[212]). Using several strategies, hiPSCs can then be differentiated into various lineages, including mesodermal and cardiac ones. The current cardiac differentiation protocols are mainly based on modulation of the WNT-signaling pathway and produce beating cells within 1-2 weeks. After prolonged cultivation and further maturation, the resulting hiPSC-derived cardiac myocytes (hiPSC-CMs) can be used for functional and molecular analysis[213–217]. These protocols predominantly result in ventricular-like hiPSC-CMs; however, electrophysiological studies on AP morphology have shown that a minority of atrial-like and nodal-like cardiac myocytes are also generated following these protocols [21,216,218,219]. HiPSC-CMs express the typical cardiac marker genes, such as genes encoding for sarcomeric filament proteins and various ion channels that are present in the human adult cardiomyocytes, although differences in the expression levels have been observed. For instance, comparable I_{Na}, $I_{Ca,L}$, I_{to}, I_{Kr}, and I_{Ks} currents (ion channels encoded by

SCN5A, *CACNA1C*, *KCND3/KCNC3*, *KCNH2,* and *KCNQ1*) have been recorded from hiPSC-CMs (**Figure 1.9**)[206,216,219]. Therefore, the AP morphology and duration of a hiPSC-CM resemble those of a human cardiomyocyte closely, making these cells a versatile model for arrhythmia studies[24,217].

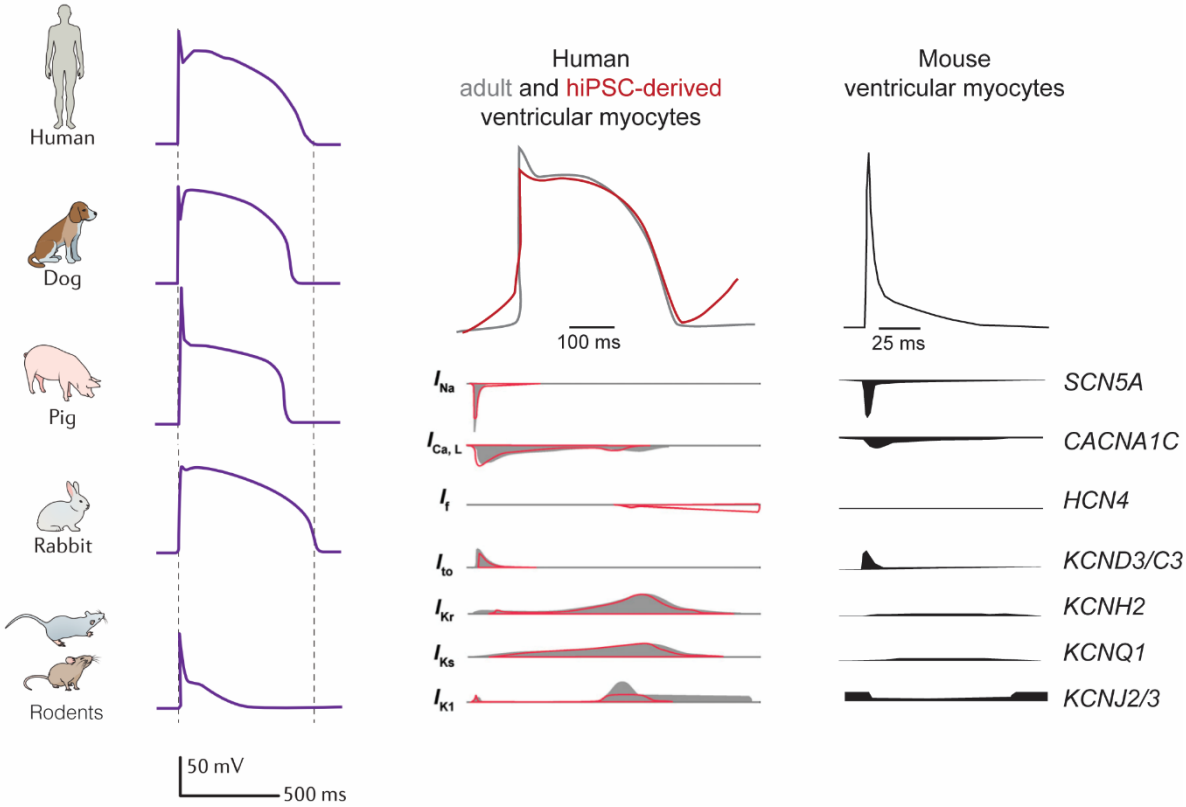

Figure 1.9. Cardiac AP waveform and characteristics in animal models of arrhythmogenesis. The scheme represents the ventricular AP recorded from isolated cardiac myocytes corresponding to animal models commonly used in arrhythmia studies (left). The AP and composition of expressed ion channels in human adult and hiPSC-derived ventricular myocytes are compared to mouse ventricular myocytes. Adapted from [23,199,220].

The hiPSCs carry the genome of the donor and, when differentiated to hiPSC-CMS, interestingly, recapitulate the cardiac phenotype of the donor. This enables for *in vitro* modeling of the cardiac disease phenotypes in a dish and provides a platform to elucidate the underlying molecular basis of the disease. Interestingly, the very first patient-specific hiPSC models reported in the cardiovascular field were the cells modeling an inherited channelopathy, namely LQTS type 1 (LQT1)[221]. The hiPSC-CMs models of LQT1 represented a comparable prolongation of APD as to the QT intervals of the donor patient. To date, many hiPSC lines derived from LQTS, SQTS, Brugada syndrome, Timothy syndrome, and familial hypertrophic cardiomyopathy have been generated[24,205,206,221–225]. The application of hiPSC-CMs can be extended to test novel disease-specific therapeutics, patient-specific drug toxicity, and cardiac regeneration that are leading into the concept of personalized medicine[67,206,217,226,227].

Like any other platform, hiPSC-CMs also have several limitations. These cells exhibit lower densities of I_{K1} current (encoded by *KCNJ2* and *KCNJ3*), and on the other hand, express I_f ion channels (encoded by HCN genes family), which are only present in fetal cardiac myocytes and the nodal cells of the adult myocardium. The I_f current is responsible for the automaticity and the spontaneous contractile activity in embryonic cardiac cells that are also observed in hiPSC-CMs. These, together with substantial differences in Ca^{2+}-handling properties and underdeveloped sarcomeric protein organization (*e.g.*, absence of the T-tubule network and the characteristic rod-shaped morphology of adult myocytes), resulted in hiPSC-CMs to be considered as less electrophysiologically mature compared to adult cardiac myocytes[226,228,229]. Another limitation of hiPSC-CMs is that, as single-cell models, the complex multicellular interactions in cardiac tissue, as well as organ-level and systemic interactions, cannot be replicated [205,206,216].

A model that circumvents this limitation is the myocardial slice prepared from human ventricular tissue[230–233]. Myocardial slices are living, 100-400 µm thick sections of adult myocardium that were first prepared decades ago. However, with recent developments of organotypic and biomimetic slicing and cultivation conditions, this platform is being increasingly regarded as a clinically relevant model representing human myocardium. Structurally, myocardial slices provide the multicellular composition of the tissue and preserve the extracellular matrix (ECM), and therefore, the regulatory effects of cell-cell and cell-ECM interactions are maintained. By proper oxygenation and constant electrical and mechanical stimulation, myocardial slices maintain the native contractile and electrophysiological properties of the myocardium over a long period of time (up to several months). Therefore, myocardial slices can be used for long-term arrhythmogenesis studies as well as safety-screening of various drugs.

1.3.3 Action potential recording techniques

The current methods for measuring the AP are patch-clamp, multi-electrode arrays, optical recording techniques, and indirect determination of AP based on the contractile activity of the myocytes (**Figure 1.10**). Patch-clamp is a conventional electrophysiology method for recording the membrane potential (or AP) and different ion currents. In this method, a small patch of the cell membrane is captured by a micropipette to form a very high resistance (known as the giga-ohm seal). Then by applying suction, the clamped part of the membrane is ruptured, exposing the inside of the cell to a recording electrode inside the micropipette. Another electrode in the solution outside the cell serves as a reference. This technique is known as the whole-cell patch-clamp that allows measurement of the changes in voltage by applying a certain current (useful for determining AP) or by applying a fixed voltage in the presence of specific ion channel blockers enables recordings of the desired ion current. A similar approach can be

used for myocardial slices by penetrating a sharp recording electrode into the tissue. However, its low-throughput and the technically complex and challenging procedure are limitations of the patch-clamp technique[23,49,234]. Automated patch-clamp systems partially improve the throughput of this technique; however, since the cell is ruptured in the process, no further assessments can be performed on the same cell. Multi-electrode array (MEA), on the contrary, is a non-invasive method that allows measurement of the field potential (FP) in cells and tissue slices using special plates containing recording electrodes on the bottom. The FP correlates to the AP duration and the QT interval on an ECG; however, analyzing individual ion currents is not possible by this approach[235].

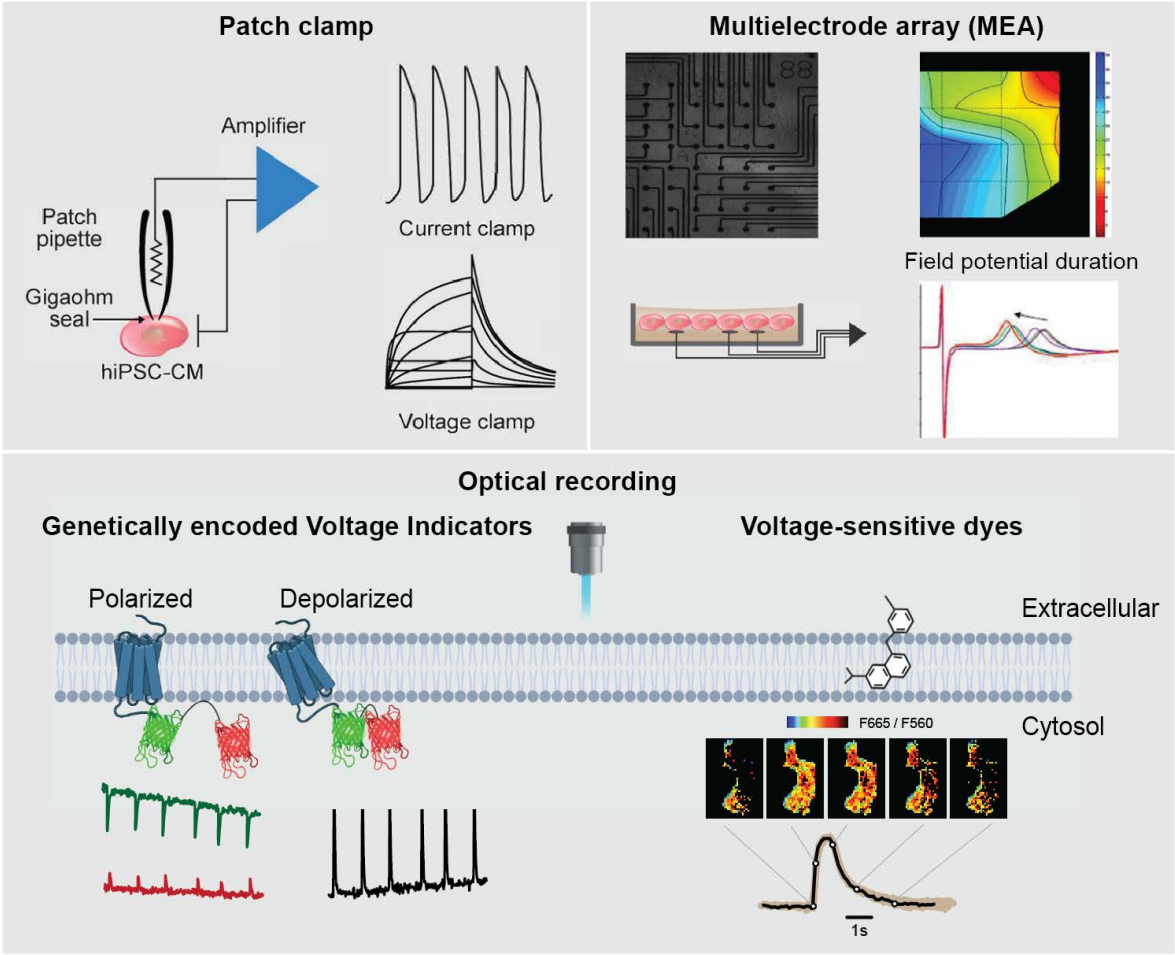

Figure 1.10. Platforms for assessment of action potential properties. Scheme representing the current methods for measuring AP duration and ion currents. Patch-clamp is an invasive method for measuring AP or ion currents, whereas multielectrode array (MEA) and fluorescent microscopy methods are non-invasive and provide the AP duration. The patch-clamp and MEA parts are redrawn after [23].

For AP recordings based on fluorescent microscopy, either voltage-sensitive dyes or genetically encoded voltage indicators (GEVIs) can be employed. Voltage-sensitive dyes (*e.g.*, amino naphthyl ethenyl pyridinium or ANEP family dyes) typically bind to the phospholipids comprising the cell membrane and respond to changes in membrane potential by shifting their fluorescent emission spectra. These dyes provide higher throughput and real-time AP

recording with sub-milliseconds precision; however, they cause a certain level of cytotoxicity. To overcome this problem, GEVIs were recently developed that enable the recording of voltage changes across a membrane in a non-invasive and biocompatible manner. GEVIs consist of a voltage-sensing domain that is fused to one or two fluorescent proteins. The optical properties of these fluorescent proteins alter following conformational changes in the voltage-sensing domain upon depolarization of the membrane. The sensory domain of the existing GEVIs are either based on light-driven ion pumps (such as bacterial opsins) [236–239] or are driven from the voltage-sensing domain of the ion channels that typically contain several positively charged amino acids and therefore react to de- or hyperpolarization of the membrane [236,239]. Subsequently, the relative changes in the membrane voltage can be recorded as a shift in the fluorescence quantum yield in case only one fluorescent protein is fused to the sensory domain. In GEVIs comprising two fluorescent proteins, voltage changes are determined as a real-time alteration of the Förster resonance energy transfer (FRET) efficacy between the two proteins [236,238]. Photostability, adequate fluorescent response, and signal-to-noise ratio, as well as specific incorporation to the plasma membrane, are the important parameters to be considered for an optimized function of GEVIs. High throughput recording and the possibility of cell or tissue-specific expression make GEVIs a versatile tool for AP measurements[237–239].

1.4 Scientific questions

The aim of this study was to identify miRNAs that regulate the expression ion channels in human cardiac myocytes, and to determine whether their manipulation enables therapeutic modulation of AP abnormalities.

The first objective was to investigate miRNA and gene expression profiles of human hiPSC-derived cardiac myocytes and human left ventricular myocardium and to identify the primary miRNAs that regulate cardiac ion channels and thereby cardiac AP.

Analyzing miRNA-targets and targets-disease enrichments lead to the identification of miR-365 as a crucial regulator of cardiac repolarizing ion channels. Therefore, the second aim of this study was to determine the functional relevance of miR-365 in cardiac rhythm control and the applicability of this miRNA in modulating pathologically altered AP duration. For this, isolated primary rat cardiac myocytes and patient-specific hiPSC-CM models of inherited arrhythmias, namely long QT syndrome type 1 (LQT1) and short QT type 1 (SQT1) were employed. After manipulating the endogenous levels of miR-365 in these models, the effects were determined by performing optical AP measurements using a voltage-sensitive dye or a genetically encoded voltage sensor.

Delineating the mechanism through which miR-365 exerts its regulatory role on AP was the next objective of the present study. To this end, hiPSC-CMs treated with miR-365 mimics and antimiRs were subjected to a detailed analysis of their transcriptome to determine the pattern of differential mRNA expression upon manipulation of miR-365.

The final goal of this study was to evaluate whether the regulatory role of miR-365 can be further extended to adult human cardiac myocytes and in the presence of other cardiac cell types. For this, myocardial slices were prepared from human left ventricular tissue, and after establishing means to alter miR-365 levels in this model, the response of adult human myocardium was determined by assessing the refractory period.

2 Materials

2.1 Chemicals, reagents and consumables

Substance or consumable	Source
1 kb DNA Ladder	New England Biolabs GmbH, Frankfurt, Germany
10% Tween 20	Bio-Rad (Hercules, CA, USA)
100 bp DNA Ladder	New England Biolabs GmbH, Frankfurt, Germany
2-mercaptoethanol	AppliChem (Darmstadt, Germany)
2-propanol	Roth (Karlsruhe, Germany)
2,3-butanenione monoxime (BDM)	Sigma Aldrich (Taufkirchen, Germany)
4-(2-hydroxyethyl)-1-piperazineethanesulfonic acid (HEPES)	Sigma Aldrich (Taufkirchen, Germany)
4′,6-diamidino-2-phenylindole (DAPI)	Sigma Aldrich (Taufkirchen, Germany)
96-well µPlate, black walls	Ibidi GmbH (Gräfelfing, Germany)
Acetic acid glacial	Roth (Karlsruhe, Germany)
Agar	AppliChem (Darmstadt, Germany)
Agar Bacteriology grade	AppliChem GmbH, Darmstadt, Germany
Agarose Standard Roti®garose for DNA/RNA-electrophoresis	Carl Roth GmbH + Co. KG, Karlsruhe, Germany
Agarose, low melt	Roth (Karlsruhe, Germany)
Agarose, standard	Roth (Karlsruhe, Germany)
Albumin, human recombinant	Merck KGaA, Darmstadt, Germany
Ammonium acetate	Sigma Aldrich (Taufkirchen, Germany)
Ampicillin	Roth (Karlsruhe, Germany)
AMPure XP beads	Beckman Coulter (Munich, Germany)
B-27™ Supplement (50X), serum free	Thermo Fisher Scientific Inc., Waltham, USA
BeadBug prefilled tubes, 2.0 mL capacity with Zirconium beads, triple-pure, high impact, 1 mm diameter	Sigma Aldrich (Taufkirchen, Germany)
Benzonase 25 KU	Merck KGaA, Darmstadt, Germany
Bromodeoxyuridine (BrdU)	Sigma Aldrich (Taufkirchen, Germany)
Bromophenol blue	Roth (Karlsruhe, Germany)
Cell Factory (Nunc), 10-Tray	Thermo Fisher Scientific (Darmstadt, Germany)
Chloroform (Trichloromethane, $CHCl_3$)	Roth (Karlsruhe, Germany)
CutSmart buffer 10x	New England Biolabs GmbH, Frankfurt, Germany
Deoxy-thymine nucleotides (oligo dTs)	Roth (Karlsruhe, Germany)
Deoxynucleotide triphosphates (dNTPs)	Thermo Fisher Scientific (Surrey, United Kingdom)
Dimethyl sulfoxide (DMSO)	AppliChem (Darmstadt, Germany)

Substance or consumable	Source
distilled DNase-/ RNase-free water	Thermo Fisher Scientific Inc. (Waltham, USA)
Dithiothreitol (DTT)	Roth (Karlsruhe, Germany)
DMEM/F-12, GlutaMAX™ Supplement	Thermo Fisher Scientific Inc. (Waltham, USA)
DNA loading dye (5x)	Qiagen (Hilden, Germany)
DNase/RNase-free water	Gibco (Karlsruhe, Germany)
dNTPs	Carl Roth GmbH + Co. KG, Karlsruhe, Germany
Dulbecco's modified eagle medium (DMEM)	Gibco (Karlsruhe, Germany)
DynaBeads MyOne Silane Beads	Thermo Fisher Scientific (Darmstadt, Germany)
Essential 8™ Flex Medium Kit	Thermo Fisher Scientific Inc. (Waltham, USA)
Ethanol	Roth (Karlsruhe, Germany)
Ethidium bromide	Roth (Karlsruhe, Germany)
Ethylenediaminetetraacetic acid (EDTA)	Roth (Karlsruhe, Germany)
Fetal calf serum	Sigma Aldrich (Taufkirchen, Germany)
Geltrex™ LDEV-Free, hESC-Qualified, Reduced Growth Factor Basement Membrane Matrix	Thermo Fisher Scientific Inc., Waltham, USA
Glycerol 100%	AppliChem (Darmstadt, Germany)
Glycogen, RNA grade	Thermo Fisher Scientific (Darmstadt, Germany)
GSK-3 Inhibitor XVI	Merck KGaA, Darmstadt, Germany
Hydrochloric acid 6 M (HCl)	Roth (Karlsruhe, Germany)
Insulin-Transferrin-Selenium-Ethanolamine (ITS -X) (100X)	Thermo Fisher Scientific (Darmstadt, Germany)
L-Ascorbic Acid 2-Phosphate	Merck KGaA, Darmstadt, Germany
L-Ascorbic Acid 2-Phosphate	Merck KGaA, Darmstadt, Germany
Leica Microsystems™ Immersion Type G, 10 ml	Leica Microsystems GmbH, Wetzlar, Germany
Lipofectamine 2000	Thermo Fisher Scientific (Darmstadt, Germany)
Lipofectamine RNAiMAX	Thermo Fisher Scientific (Darmstadt, Germany)
Magnesium sulfate heptahydrate ($MgSO4.7H_2O$)	Merck (Darmstadt), Germany
Medium 199, Earle's Salts	Gibco (Karlsruhe, Germany)
Microseal B adhesive seals	Bio-Rad (Hercules, CA, USA)
Minimum Essential Eagle (MEM)	Gibco (Karlsruhe, Germany)
Murine RNase inhibitor	Thermo Fisher Scientific (Darmstadt, Germany)
Opti-MEM™ I Reduced Serum Medium, no phenol red	Thermo Fisher Scientific Inc., Waltham, USA

Substance or consumable	Source
Optical Flat 8-cap strips	Bio-Rad (Hercules, CA, USA)
OptiPrep	Sigma Aldrich (Taufkirchen, Germany)
Pap Pen	Vector Laboratories (Burlingame, USA)
Paraformaldehyde (PFA)	Sigma Aldrich (Taufkirchen, Germany)
PEI MAX - Transfection Grade Linear Polyethyleneimine Hydrochloride (MW 40,000)	Polysciences Inc., Warrington, USA
Penicillin / Streptomycin	Gibco (Karlsruhe, Germany)
Penicillin-Streptomycin (5,000 U/mL)	Thermo Fisher Scientific Inc., Waltham, USA
peqGOLD Trifast	PeqLAB (Erlangen, Germany)
Phosphate buffered saline (PBS)	Gibco (Karlsruhe, Germany)
Potassium acetate	Roth (Karlsruhe, Germany)
Potassium bicarbonate ($KHCO_3$)	Sigma Aldrich (Taufkirchen, Germany)
Potassium chloride	Merck KGaA, Darmstadt, Germany
Potassium ferricyanide ($K_3[Fe(CN)_6]$)	Roth (Karlsruhe, Germany)
Potassium ferrocyanide ($K_4[Fe(CN)_6]$)	Roth (Karlsruhe, Germany)
Ringer-Lactat nach Hartmann B. Braun	B. Braun Melsungen AG, Melsungen, Germany
RNase Zap	Sigma Aldrich (Taufkirchen, Germany)
RPMI 1640 with HEPES with GlutaMax	Thermo Fisher Scientific Inc., Waltham, USA
RPMI 1640 without Glucose	Thermo Fisher Scientific Inc., Waltham, USA
Saccharose	Roth (Karlsruhe, Germany)
Sodium acetate ($NaCH_3COO$)	Merck (Darmstadt, Germany)
Sodium chloride (NaCl)	Sigma Aldrich (Taufkirchen, Germany)
Sodium dihydrogen phosphate dihydrate ($NaH_2PO_4.2H_2O$)	Roth (Karlsruhe, Germany)
Sodium dodecyl sulfate (SDS)	Roth (Karlsruhe, Germany)
Sodium hydrogen phosphate dibasic (Na_2HPO_4)	Roth (Karlsruhe, Germany)
Sodium hydroxide (NaOH)	Roth (Karlsruhe, Germany)
Sodium hydroxide (NaOH)	Roth (Karlsruhe, Germany)
Sodium orthovanadate (Na_3VO_4)	Sigma Aldrich (Taufkirchen, Germany)
SPRIselect beads	Beckman Coulter (Munich, Germany
Taurine	Sigma Aldrich (Taufkirchen, Germany)
Tris base	Roth (Karlsruhe, Germany)
Trisodium-citrate (dihydrate)	Roth (Karlsruhe, Germany)
Triton-X 100	Sigma Aldrich (Taufkirchen, Germany)
TRIzol reagent	Thermo Fisher Scientific (Darmstadt, Germany)
Trypan blue	AppliChem (Darmstadt, Germany)

Substance or consumable	Source
Tryptone-peptone	AppliChem (Darmstadt, Germany)
Vectashiled mounting medium H-1000	Vector Laboratories (Burlingame, USA)
Versene Solution	Thermo Fisher Scientific Inc., Waltham, USA
Vitamin B12	Sigma Aldrich (Taufkirchen, Germany)
Wnt antagonist II, IWP-2	Merck KGaA, Darmstadt, Germany
Yeast extract	AppliChem (Darmstadt, Germany)
Zeiss Immersion oil 518 F	Carl Zeiss Microscopy GmbH, Jena, Germany

2.2 Buffers and media

Solution	Composition
For Cell and tissue culture	
BrdU solution	230 mg BrdU, 74.8 ml ddH_2O, filtered, aliquots stored at -20°C
Cardio Culture Medium (CCM)	500 ml RPMI with HEPES and GlutaMAX, 10 ml B27 Supplement, 5 ml Pen/Strep, storage for up to 1 month at 4°C
Cardio Culture Medium without antibiotics	500 ml RPMI with HEPES and GlutaMAX, 10 ml B27 Supplement, storage for up to 1 month at 4°C
Cardio Differentiation Medium (CDM)	500 ml RPMI with HEPES and GlutaMAX, 250 mg Albumin, 100 mg L-Ascorbic Acid 2 Phosphate, filtered, storage for up to 1 month at 4°C
Cardio Digestion Medium	80 ml Cardio Culture Medium, 20 ml FBS, 100 µl Thiazovivin (2 mM), filter, storage for up to 2 weeks at 4°C
Cardio Selection Medium (CSM)	500 ml RPMI 1640 w/o Glucose and HEPES, 2 ml Lactate/HEPES (1 M), 250 mg Albumin, 100 mg L-Ascorbic Acid 2 Phosphate, filtered, storage for up to 1 month at 4°C
CBFHH	137 mM NaCl, 5.36 mM KCl 0.81, mM $MgSO_4.7H_2O$, 5.55 mM Dextrose, 0.44 mM KH_2PO_4, 0.34 mM $Na_2HPO_4.7H_2O$, pH adjusted to 7.3 with NaOH, filtered
CHIR99021 (12 mM)	5 mg CHIR99021 was dissolved in 894 µl DMSO, aliquots storage at -20°C
Collagenase II Solution in RPMI	7 ml RPMI with HEPES and GlutaMAX, 9 mg Collagenase II (310 U/mg), filtered
Collagenase/Pancreatin solution	120 mg Collagenase II, 80 mg Pancreatin, filled up tp 200 ml with warm CBFHH, filtered
Cryo Preservation Medium	2 ml DMSO, 8 ml E8-flex Medium, 20 µl Thiazovivin (2 mM)
E8-flex + Thiazovivin (2 µM)	1 µl Thiazovivin (2 mM) per 1 ml E8-flex Medium
Geltrex Solution	133 µl Geltrex and 12 ml cold DMEM-F12
HEK culture-medium	450 ml DMEM, 50 ml FCS (10 %), 5 ml Pen/Strep

Solution	Composition
IWP2 (5 mM)	10 mg IWP2 was dissolved in 4.28 ml DMSO, aliquots storage at -20°C
Lactate/HEPES (1M)	3 ml sodium DL-lactate, 18 ml HEPES (1M), aliquot, store for up to 1 year at -20°C
NRCM culture medium	25 ml FCS, 5 ml Penicillin/Streptomycin, 5 ml BrdU, filled up to 500 ml with NRCM incomplete medium
NRCM incomplete medium	10.7 g MEM, 0.35 g $NaHCO_3$,1 ml vitamin B12 67% (w/v), filled up to 1 l with ddH_2O, pH adjusted to 7.3, filtered
Slice culture medium	Medium 199, 1% penicillin/streptomycin, 1x insulin/ transferrin/ selenium (ITS), 50 µM 2-mercaptoethanol, storage at 4°C
Slicing buffer	136 mM NaCl, 5.4 mM KCl, 1 mM $MgCl_2$, 0.33 mM NaH_2PO_4,10 mM glucose, 0.9 mM $CaCl_2$, 30 mM 2,3-butadione-2-monoxime, 5 mM HEPES, pH adjusted to 7.4, filtered
Thiazovivin	10 mg Thiazovivin dissolved in in 16.06 ml DMSO, aliquots stored at -20°C for up to 1 year
For molecular cloning	
15% Iodixanol:	12 ml OptiPrep, 36 ml PBS-MKN
25% Iodixanol:	20 ml OptiPrep, 28 ml PBS-MK, 120 µl Phenol Red (0.5%)
4 % PFA	20 g paraformaldehyde was dissolved in 480 ml 1xPBS (pH 7.4), heated to 60°C, 500 µl 1 M NaOH was added, pH adjusted to 7.2, fill up to 500 ml with PBS, aliquots stored at -20°C
40% Iodixanol:	30 ml OptiPrep, 15 ml PBS-MK
60% Iodixanol:	50 ml OptiPrep, 62.5 µl Phenol Red (0.5%)
AAV lysis buffer	50 mM TRIS-base, 150 mM NaCl, 5 mM $MgCl_2$.6 H_2O, fill up to 1 l with double-distilled water
Ampicillin (100 ng/ml, 1000x)	5 g Ampicillin in 50 ml dH_2O, storage at -20°C
DNA loading buffer	0,025 g Xylene Cyanol, 1.4 ml EDTA (0.5 M), 3.6 ml Glycerol, 7.0 ml H_2O
Kanamycin (10 mg/ml, 300x)	500 mg Kanamycin in 50 ml dH_2O, storage at -20°C
LB Agar plates with ampicillin	LB-Agar dissolved microwave, cooled down, ampicillin (1/1000) was added and mixed. 10 cm culture dishes were filled with 20 ml LB-agar on a clean working surface, when agar solidified, plates were stored at 4°C.
LB medium	50 g Tryptone-Peptone, 25 g Yeast extract, 25 g NaCl, 5 ml NaOH (1M), fill up to 5 l with dH_2O, aliquot in glass bottles, autoclave, store at 4°C
LB medium + ampicillin	400 µl Ampicillin in 400 ml LB-Medium

Solution	Composition
LB-Agar	40 g Tryptone-Peptone, 20 g Yeast extract, 20 g NaCl, 4 ml NaOH (1M), 60 g Agar, fill up to 4 l with dH_2O, aliquot in glass bottles, autoclave, store at 4°C
PBS-MK solution	101.7 mg MgCl2.6H2O (1 mM), 93.2 mg KCl (2.5 mM), filled up to 500 ml with PBS, pH adjusted to 7.4, filtered
PBS-MKN solution	101.7 mg MgCl2.6H2O (1 mM), 93.2 mg KCl (2.5 mM), 29.22 g NaCl (1 M), filled up to 500 ml with PBS, pH adjusted to 7.4, filtered
PEI solution	50 mg PEI “MAX” in 45 ml dH_2O, adjust pH to 1.9, stir for 2 h at RT, adjust pH to 7.1, full up to 50 ml with dH_2O, sterile filter, aliquot
TAE (1x)	20 ml 50x TAE, fill up to 1 l with double-distilled water
TAE (50x)	242 g Tris, 57.1 ml Acetate, 37.2 g $Na_2EDTA.2\ H_2O$
For functional assays	
FRET-buffer 1x	4 g NaCl, 0.2 g KCl, 1.2 g HEPES, 0.15 g $CaCl_2$, 0.047 g $MgCl_2$, 0.9 g Glucose, filled up to 500 ml with H_2O, pH adjusted to 7.4, filtered
50 % glycerol in PBS	10 ml glycerol (100 %), 10 ml PBS
ANEPPS solution	10 µl di-8-ANEPPS (2 mM), 4 µl Pluronic F127, 4 µl CCM
ANEPPS stock (2 mM)	5mg di-8-ANEPPS, 5 ml DMSO, aliquots stored at 4°C protected from light

2.3 Enzymes

Enzyme	Source
AccuPrime Pfx DNA polymerase	Invitrogen (Karlsruhe, Germany)
Antarctic phosphatase	New England Biolabs (Ipswich, MA, USA)
Benzonase	Merck (Darmstadt, Germany)
Collagenase type II (310 U/mg)	Worthington Biochemical Corporation (Lakewood, USA)
DNase I	Sigma Aldrich (Taufkirchen, Germany)
Murine RNase inhibitor	New England Biolabs (Ipswich, MA, USA)
Pancreatin	Sigma Aldrich (Taufkirchen, Germany)
Phusion High-Fidelity DNA polymerase	New England Biolabs (Ipswich, MA, USA)
Restriction endonucleases	New England Biolabs (Ipswich, MA, USA)
Superscript II reverse transcriptase	Invitrogen (Karlsruhe, Germany)
T4 DNA Ligase	New England Biolabs (Ipswich, MA, USA)
Trypsin-EDTA (0.05%), phenol red	Gibco (Karlsruhe, Germany)
Trypsin-EDTA (0.25%), phenol red	Gibco (Karlsruhe, Germany)

2.4 Antibodies

Antibody	Dilution	Application	Manufacturer/ Catalogue No.
Primary antibodies			
Mouse monoclonal Anti-α-Actinin (Sarcomeric)	1:800	IF	Sigma Aldrich (A7811)
Ventricular myosin Light Chain 2 (MYL2), Rabbit polyclonal	1:400	IF	Proteintech (10906-1-AP)
wheat germ agglutinin (WGA), Alexa Fluor-647 conjugate	1:400	IF	Invitrogen (W32466)
Secondary antibodies			
Alexa Fluor 488, goat anti-mouse IgG H+L	1:400	FACS	Thermo Fisher (A28175)
Alexa Fluor 594, goat anti-rabbit IgG H+L	1:400	FACS	Thermo Fisher (A11037)

2.5 Cell lines and primary cells

Abbreviation	Cell Type	Source
NRCM	neonatal rat cardiac myocytes	isolation described in methods
Control hiPSC	Healthy control human induced pluripotent stem cell	AG Moretti [240]
LQT1 hiPSC	adult mouse cardiac myocytes	AG Moretti [221]
SQT1 hiPSC	adult mouse cardiac fibroblasts	AG Borggrefe [225]
HEK293	human embryonic kidney cell line	ATCC (Manassas, VA, USA)
HEK293T	HEK293 cells transformed with the SV40 large T antigen	ATCC (Manassas, VA, USA)

2.6 Bacterial strains

Strain	Genotype	Source
DH10B	F$^-$*mcr*A Δ(*mrr-hsd*RMS-*mcr*BC) Φ80*lac*ZΔM15 Δ*lac*X74 *rec*A1 *end*A1 *ara*D139Δ(*ara*, *leu*)7697 *gal*U *gal*K λ$^-$*rps*L *nup*G	Invitrogen (Karlsruhe, Germany)
Stbl2	F− endA1 glnV44 thi1 recA1 gyrA96 relA1 Δ(lac-proAB) mcrA Δ(mcrBC-hsdRMS-mrr) λ−	Invitrogen (Karlsruhe, Germany)

SURE	e14– (McrA–) Δ(mcrCB-hsdSMR-mrr)171 endA1 supE44 thi-1 gyrA96 relA1 lac recB recJ sbcC umuC::Tn5 (Kanr) uvrC [F' proAB lacIqZΔM15 Tn10 (Tetr)]	Stratagene (San Diego, CA, USA)

2.7 Oligonucleotides and plasmids

Synthetic oligonucleotides designed for manipulations o miR-365 levels were produced commercially:

Synthetic oligonucleotide	Identifier	Source
Ambion® FAM3™ Dye-Labeled Pre-miR Negative Control #1	AM17121	ThermoFisher Scientific (Darmstadt, Germany)
hsa-miR-365a-3p Ambion® Pre-miR™ miRNA Precursor	PM11133	ThermoFisher Scientific (Darmstadt, Germany)
LNA-antimiR-365a-3p Sequence: 5‘- ATTTTTAGGGGCATT -3‘	500150	Exiqon (Vedbaek, Denmark)
LNA-antimiR-control Sequence: 5‘- TGATTTACACCCGGTG -3‘	339147YCI0200562-FFA	Exiqon (Vedbaek, Denmark)
Pre-miR™ miRNA Precursor Negative Control #1	AM17110	ThermoFisher Scientific (Darmstadt, Germany)

Specific primers for determining mRNA and miRNA expression levels using qPCR were designed and were synthesized commercially as following:

Primer name	Sequence (5’ to 3’)	Source
hsa-miR-365a-3p miRCURY LNA miRNA PCR Assay	NA	Exiqon, Vedbaek, Denmark
miRCURY LNA miRNA PCR Assay for U6	NA	Exiqon, Vedbaek, Denmark
Human *KCNQ1* forward	AGCCAGCCAAACACACAGAAG	This work, synthesized by Sigma Aldrich
Human *KCNQ1* reverse	GAAGGAACCCCTGTCCTGTGTA	This work, synthesized by Sigma Aldrich
Human *GAPDH* forward	TCCTCTGACTTCAACAGCGA	This work, synthesized by Sigma Aldrich
Human *GAPDH* reverse	GGGTCTTACTCCTTGGAGGC	This work, synthesized by Sigma Aldrich

Rat *Kcnq1* forward	GCATCACACCTCCCAGAAAT	This work, synthesized by Sigma Aldrich
Rat *Kcnq1* reverse	CTGGCATGTCCCAGCTTTAT	This work, synthesized by Sigma Aldrich
Rat *Kcnh2* forward	GCTTCCTGTGTTTGGTGGAT	This work, synthesized by Sigma Aldrich
Rat *Kcnh2* reverse	CCCTACCATGTCCTTCTCCA	This work, synthesized by Sigma Aldrich
Rat *Kcna1* forward	ATGAGGGAGTTAGGGCTGCT	This work, synthesized by Sigma Aldrich
Rat *Kcna1* reverse	TCGGGGATACTGGAGAAGTG	This work, synthesized by Sigma Aldrich
Rat *Cacna1c* forward	TCTGCTCTGCCTGACTCTGA	This work, synthesized by Sigma Aldrich
Rat *Cacna1c* f reverse	CACACAATTGGCAAAAATCG	This work, synthesized by Sigma Aldrich
Rat *Kcnj2* forward	CATACCCGACAACAGTGCAG	This work, synthesized by Sigma Aldrich
Rat *Kcnj2* reverse	GTCCGCCAGGTACCTCTGT	This work, synthesized by Sigma Aldrich

Cloned plasmids and cloning oligonucleotides

Complete details of the cloning procedure for various constructs are explained in section 3.2. The genetically encoded FRET sensor, known as voltage sensitive fluorescent protein-Clover GFP/mRuby2 RFP (in short, VSFP-CR) under control of CAG promoter was purchased from Addgene (#40257) and was cloned in an Adeno Associated Virus (AAV) backbone (namely pTREK1). For ventricular-specific measurements, the ubiquitous CAG promoter was then substituted by the ventricular specific MYL2 promoter:

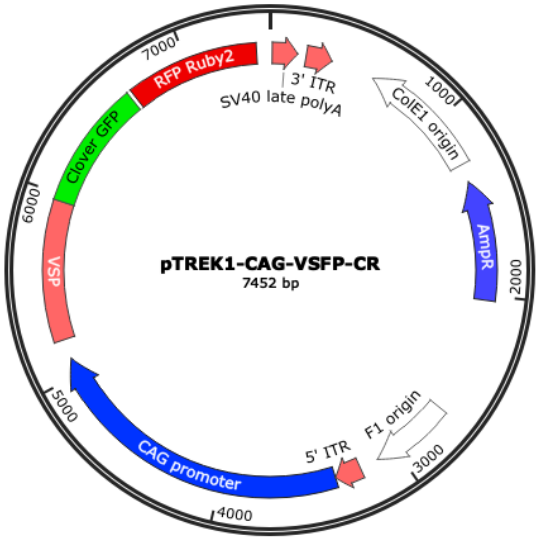

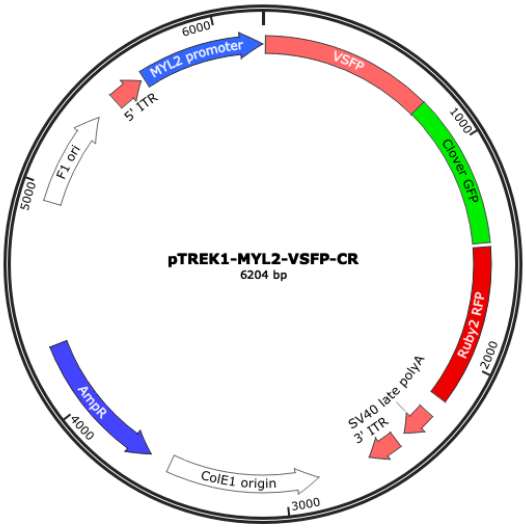

The double fluorescent (df-) reporter constructs for miR-365 activity and for miR-365-target validation:

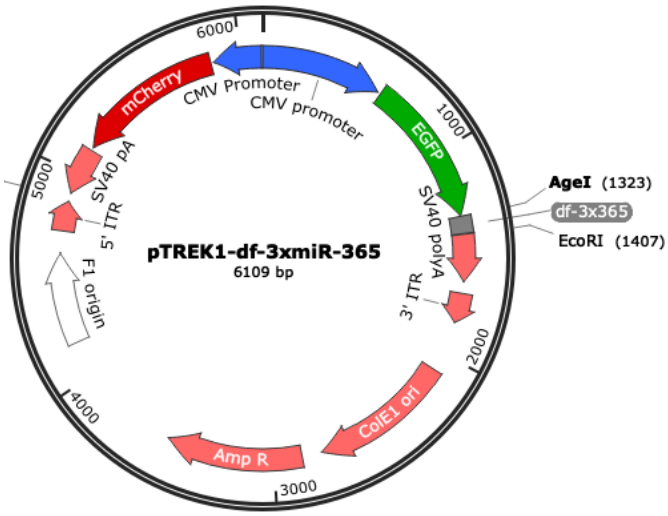

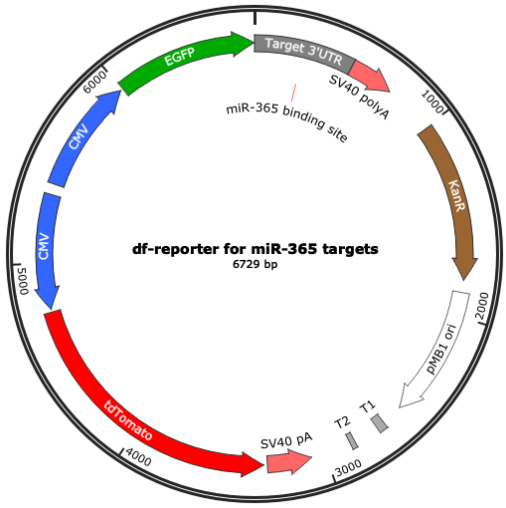

The df-reporter construct for miRNA activity (left, reported in PhD thesis of Petros Avramopoulos, 2017) was sub-cloned in an AAV backbone for enhanced delivery into hiPSC-CMs. Three repetetive miR-365 binding sites were cloned in this plasmid by anealing oligonucleotides containing the corresponding sequence binding sites and restriction enzyme cutting sites (section 3.2.4). The df-reporters for *KCNA1*, *KCNQ1*, *KCNH2*, *KCNJ2*, and *CACNA1C* were cloned in a previous work (B. Sc. thesis of Anna Näger, 2014). For *SCN4B*, *SCN5A*, *KCNE1*, *KCNC3,* and *KCNJ3* the constructs carrying 3' UTRs with native or mutated binding sites for miR-365 were cloned using the following primers. In the following table, the cutting sites are underlined, the seed sequence of miR-365 binding sites are depicted in bold letters, and the introduced mutations are marked in red.

Primer name	Sequence (5' to 3')
KCNC3 mutagenesis Reverse	AAAAA ATGGGGGGGACTCAA**A**G**T**T**C**G**C**CTTGCATAGGAATCGTTG
KCNC3 wild type Forward1 with AgeI	AAAAAA CCACACCGGTCCCAGACT
KCNC3 wild type Reverse1 with EcoRI	AAAAAA GAATTC ATTGACTTGGGGGATGGGGT
KCNE1 mutagenesis Forward1	CCTGAAAGCTCAGCTGCCT**G**C**G**A**A**C**T**CCTGAAGAGTATGG AATAT
KCNE1 wild type Forward1 with AgeI	AAAAAA ACCGGT TGAAGCCACCCAGCTTAG
KCNE1 wild type Reverse1 with EcoRI	AAAAAA GAATTC GGTGGGGCAAAGATCACAG
KCNJ3 mutagenesis Forward1 for the 1st binding site with AgeI	AAAAAA ACCGGT CAAAGCACTCCCTTA**C**G**A**A**C**T**A**TTTAATGTTTGATTTAGTAA
KCNJ3 mutagenesis Forward2 for the 2nd binding site	AAAAAA CTTTATTAGAGTAGGAAGGCTACT**C**G**A**A**C**T**A**ATTATTAATAC CAA
KCNJ3 wild type Forward1 with AgeI	AAAAAA ACCGGT CAAAGCACTCCCTTAGGCAT
KCNJ3 wild type Reverse1 with EcoRI	AAAAAA GAATTC GCCTCCCAAGACCTTAAACAG
SCN4B mutagenesis Forward1	GTGACTGAGATTGTAGGGG**G**C**G**A**A**C**T**TTTGGTTGCCCCCA TGCGT
SCN4B wild type Forward1 with AgeI	AAAAAA ACCGGT GGAAAGGGATCTGGGAAGC
SCN4B wild type Reverse1 with EcoRI	AAAAAA GAATTC TGGCCAGGTCTCTCAAGAT
SCN5A mutagenesis Forward1	TGTGGCAGTGCTGAAGG**G**C**G**A**A**C**T**GCCGGCGAGTAAAGTA TTATG
SCN5A wild type Forward1 with AgeI	AAAAAA ACCGGT CAGCTGCTGACAATCCTATTT
SCN5A wild type Reverse1 with EcoRI	AAAAAA GAATTC CTGTGTAGCAGGCGGTGAG
DF-3x365 top oligo	AAAA ACCGGT ATAAGGATTTTTAG**GGGCATT**A AAATTT ATAAGGATTTTTAG**GGGCATT**A AAATTT ATAAGGATTTTTAG**GGGCATT**A G
DF-3x365 bottom oligo	AAAAA GAATTC T**AATGCCC**CTAAAAATCCTTAT AAATTT T**AATGCCC**CTAAAAATCCTTAT AAATTT T**AATGCCC**CTAAAAATCCTTAT A

2.8 Kits

Kit name	Source
Agilent RNA 6000 pico kit	Agilent Technologies (Böblingen, Germany)
Chromium single cell 3' kit (v2 chemistery)	10x genomics (Pleasanton, CA, USA)
FastStart Universal SYBR Green Master (Rox)	Merck (Darmstadt, Germany)
NEBNext Multiplex Small RNA Library Prep Set for Illumina® (Set 1)	New England Biolabs (Ipswich, MA, USA)
PureLink HiPure plasmid filter gigaprep kit	Thermo Fisher Scientific (Darmstadt, Germany)
PureLink HiPure plasmid filter maxiprep kit	Thermo Fisher Scientific (Darmstadt, Germany)
PureLink HiPure plasmid filter midiprep kit	Thermo Fisher Scientific (Darmstadt, Germany)
Q5 Site-directed mutagenesis kit	New England Biolabs (Ipswich, MA, USA)
QIAprep spin miniprep kit	Qiagen (Hilden, Germany)
QIAquick gel extraction kit	Qiagen (Hilden, Germany)
TapeStation high sensitivity D1000 kit (ScreenTape and reagents)	Agilent Technologies (Böblingen, Germany)
TapeStation high sensitivity D5000 kit (ScreenTape and reagents)	Agilent Technologies (Böblingen, Germany)
TapeStation high sensitivity RNA kit (ScreenTape and reagents)	Agilent Technologies (Böblingen, Germany)
TapeStation RNA kit (ScreenTape and reagents)	Agilent Technologies (Böblingen, Germany)
TruSeq Stranded mRNA Sample Preparation	Illumina (San Diego, CA, USA)
Universal cDNA Synthesis Kit II (for microRNA PCR)	Exiqon (Vedbaek, Denmark)

2.9 Instruments

Devices	Source
10x chip holder (type A)	10x genomics (Pleasanton, CA, USA)
10x Magnetic Separator	10x genomics (Pleasanton, CA, USA)
10x Vortex adapter	10x genomics (Pleasanton, CA, USA)
Agilent 2100 bioanalyzer	Agilent Technologies (Böblingen, Germany)
Agilent 4200 TapeStation	Agilent Technologies (Böblingen, Germany)
Barnstead NanoPure water purification system	Thermo Fisher Scientific (Darmstadt, Germany)
Beam splitter 565dcxr	Chroma Technology Corporation (Bellows Falls, USA)
Centrifuge 5417R	Eppendorf (Hamburg, Germany)

Centrifuge 5702R	Eppendorf (Hamburg, Germany)
Centrifuge 5804R	Eppendorf (Hamburg, Germany)
Centrifuge GS-6KR kneewell refrigerated	Beckman Coulter (Brea, CA, USA)
Chromium controller	10x genomics (Pleasanton, CA, USA)
Countess automated cell counter	Thermo Fisher Scientific (Darmstadt, Germany)
Countess II automated cell counter	Thermo Fisher Scientific (Darmstadt, Germany)
Electrophoresis power supply – EPS 301	GE Healthcare (Munich, Germany)
Evolve-EM512 EMCCD digital camera	Visitron Systems GmbH (Puchheim, Germany)
FastPrep-24 classic bead beating grinder and lysis system	MP biomedicals (Eschwege, Germany)
Gel electrophoresis chamber	Peqlab (Erlangen, Germany)
Inverted fluorescence microscope Axio Observer Z1	Zeiss (Oberkochen, Germany)
Invitrogen EVOS FL Auto 2 Cell Imaging System	Thermo Fisher Scientific Inc. (Waltham, USA)
Jumo iTRON I6 Temperature controller	JUMO GmbH (Fulda, Germany)
Leica SP5 confocal microscope	Leica (Wetzlar, Germany)
Mastercycler pro PCR system, 96-well	Eppendorf (Hamburg, Germany)
MicroPublisher 5.0 RTV CCD camera	QImaging (Surrey, Canada)
MicroPulser electroporator	Bio-Rad (Hercules, CA, USA)
MiniSpin plus microcentrifuge	Eppendorf (Hamburg, Germany)
Mixers thermomixer comfort	Eppendorf (Hamburg, Germany)
MR Hei-Standard magnetic stirrer	Heidolph Instruments (Schwabach, Germany)
MyoDish setup	AG Dendorfer, LMU (Munich, Germany)
Nanodrop ND-1000	Thermo Scientific (Surrey, England)
Optima L-80 XP type 75 Ti rotor	Beckman Coulter (Brea, CA, USA)
Optima L-80 XP ultracentrifuge	Beckman Coulter (Brea, CA, USA)
QuantStudio 5 Real-Time PCR system, 384-well	Thermo Fisher Scientific (Darmstadt, Germany)
Retiga-4000DC CCD camera	QImaging (Surrey, Canada)
S3 cell sorter	Bio-Rad (Hercules, CA, USA)
StepOnePlus Real-Time PCR system, 96-well	Applied Biosystem (Foster City, USA)
T 10 basic ULTRA-TURRAX	IKA Works (Wilmington, NC, USA)
TILL Photonics Polychrome V monochromator	Thermo Fisher Scientific (Martinsried, Germany)
Vortex-Genie 2	Scientific Industries (Bohemia, NY, USA)

2.10 Software and packages

Software of package	Source
Adobe Acrobat Pro DC, version 2020.013.20064	Adobe Systems Incorporated (San Jose, CA, USA)
Adobe Illustrator CS6, version 25.0.1	Adobe Systems Incorporated (San Jose, CA, USA)
CellRanger, version 1.3.6	10x Genomics
ClueGO, version 2.5.6	Bindea et al[241]
Cytoscape, version 3.8.0	Shannon et al[242]
DESeq2, version 2.11.40.2	Love et al[243]
Galaxy	Afgan et al[244]
Leica Application Suite Advanced Fluorescence, version 2.7.9723	Leica Microsystems GmbH (Wetzlar, Germany)
MacVector, version 13.5.5	MacVector Inc. (Apex, NC, USA)
Metafluor imaging, version 7.6.5.0	Molecular Devices (San Jose, CA, USA)
MetaMorph Offline, version 7.10.1	Molecular Devices (San Jose, CA, USA)
MetaMorph Premier imaging system, version 7.10.1	Molecular Devices (San Jose, CA, USA)
Microsoft Office, version 16.43	Microsoft (Redmond, WA, USA)
miRDeep2, version 2.0.0	Friedländer et al[245]
Prism 6 for Mac OS, version 6.0c	GraphPad Software (La Jolla, CA, USA)
Prism 8 for Mac OS, version 8.4.1	GraphPad Software (La Jolla, CA, USA)
Python, version 2.7 and 3.8	Python Software Foundation
Seurat, version 3.1.5 and 3.2.6	Butler et al[246,247]
STAR, version 2.6.0	Dobin et al[248]
StepOne software v2.1	Applied Biosystems (Foster City, CA, USA)
StringTie, version 1.3.6	Pertea et al[249]
Trim Galore!, version 0.4.2	Babraham Bioinformatics institute

3 Methods

3.1 Cell and tissue culture

3.1.1 Cultivation of hiPSCs and cardiac differentiation

3.1.1.1 Recovery of cryopreserved hiPSCs

The patient-specific hiPSC lines generated from a healthy control[240], and patients suffering from LQT1[221] and SQT1[225] were obtained as frozen aliquots. The family pedigrees and genetic mutations of the donors, as well as the generation and characterization of the hiPSCs, were described previously[221,225,240]. Each cell line was recovered in a cultivation condition identical to those prior to the cryopreservation. The SQT1 hiPSCs were maintained in a feeder-free cultivation system, thus for their recovery, 6-well plates were covered with cold Geltrex solution and were incubated for 1 hour at 37 °C. The frozen SQT1 hiPSCs were directly transferred from the nitrogen tank (or -80 °C storage) to 37 °C water bath and were gently swirled until partially thawed. The cell suspension was transferred to a 15 ml tube, and 1 ml of E8-flex medium warmed to room temperature and supplemented with Thiazovivin (2 µM) was added dropwise to the cell suspension. While adding the medium, the tube was mixed by shaking in order to avoid osmotic shock. Then, the cryovial was washed with 1 ml of E8-flex with Thiazovivin and the medium was added to the cell suspension. After adding approximately 5 ml medium with a pipette, the mixture was centrifuged at 200 rcf for 5 min (centrifuge sat at room temperature). The supernatant was then removed, the cells were resuspended in 2 ml E8-flex with Thiazovivin, and after removing the Geltrex solution from the well, the hiPSCs were seeded. Homogenous distribution was achieved by gently shaking the plate in all directions, and with minimal movement, the plate was placed in a 37 °C incubator with 5% CO_2. The day after the recovery, 1 ml additional E8-flex medium supplemented with Thiazovivin was added to the cells and after 2 days medium was completely replaced with fresh E8-flex.

The healthy control and LQT1 hiPSCs were cultivated in a feeder-dependent system; therefore, one day prior to the recovery of these hiPSC lines, the feeder cells were prepared. For that, inactivated mouse embryonic fibroblasts (MEF) were thawed on a 35 mm plate that was coated with 0.1% gelatin and was incubated at 37 °C for 15 min. The thawing procedure was done as described above, while in each step, the pre-warmed MEF medium was added to the cells instead. After centrifugation and resuspension, the feeder cells were counted using Countess automated cell counter and approximately 300,000-500,000 cells were seeded in the gelatin-coated plate. After overnight incubation of the feeder cells in a 37 °C incubator with 5% CO_2, the hiPSCs were thawed similarly, whereas the hiPSCs were resuspended in 2 ml

hiPSC medium supplemented with human bFGF (10 ng/ml) and Thiazovivin (2 µM) and were seeded on feeder-coated plates. The medium was exchanged to fresh hiPSC medium with human bFGF every other day.

3.1.1.2 Feeder-free cultivations and maintenance of hiPSCs

The SQT1 hiPSCs were maintained in the E8-flex medium. Every other day the medium was exchanged. At 90-95% of confluency, the cells were replated. To do so, the cells were washed once and then were incubated with Versene (1 ml per 1 well of a 6-well plate) either at room temperature or at 37 °C for 5-10 min. Before the cells detached completely, Versene was aspirated and the cells were washed away by the addition of 1 ml E8-flex with Thiazovivin (2 µM). The cells were seeded in the desired ratio in Geltrex-coated plates and E8-flex medium with Thiazovivin was supplemented (2 ml per 1 well of a 6-well plate). The next day after splitting, the medium was exchanged to E8-flex without Thiazovivin.

The control and LQT1 hiPSC lines were cultured in a feeder-dependent manner after the recovery until reaching about 90% of confluency. Then, the cells were passaged from the feeder layer onto a Geltrex-coated plate as described for SQT1 cells. For the adaptation of the cells to the feeder-free culture system and to omit the carry-over of feeder cells, the hiPSCs were kept and passaged at least 3 times on Geltrex before starting the subsequent experiments (e.g., the cardiac differentiation).

3.1.1.3 Cryopreservation of hiPSCs

For cryopreservation of the hiPSCs, the cells (at 90-95% confluency in a well of a 6-well plate) were detached as described above and were collected in 1 ml of E8-flex medium. Subsequently, 1 ml of the freezing medium was added dropwise to the cell suspension while shaking the mixture to avoid osmotic shock. The cells were then distributed in cryovials (0.5-1 ml per vial, yielding the splitting ratio of 1:2 to 1:4) and were transferred to a freezing container and stored at -80 °C for at least 24 h before transferring to into a liquid nitrogen tank for long-term storage.

3.1.1.4 Cardiac differentiation of hiPSCs

For chemically defined monolayer differentiation of hiPSCs into cardiac myocytes, the cells from 2 wells of a 6-well plate were passaged (as described in 3.1.1.2) and seeded into a full 12-well-plate coated with Geltrex priorly. After 2-5 days, when the cells reached 70 to 95 % of confluency, the differentiation was initiated. The confluency of the cells is critical for a successful outcome and needs to be optimized for each cell line accordingly. For C6, LQT1 and SQT1 cells the optimal confluency on Day 0 was approximately 85-90%, 90-100%, and 70-80%, respectively. The differentiation protocol used here was based on modulation of Wnt

signaling pathway [214,215,250]. For The control and LQT1 hiPSC lines, at Day 0 the medium was changed to Cardio Differentiation Medium (CDM, 2 ml per well) supplemented with GSK-3 inhibitor XVI (CHIR99021, 4 µM). After 48 hours (on Day 2). The medium was changed to CDM with Wnt antagonist II (IWP2, 5 µM). On Day 4 and Day 6 of the differentiation, CDM without any supplements was added to the cells and from Day 8 onward, the medium was exchanged every 2-3 days to Cardio Culture Medium (CCM). For SQT1 cells, a higher concentration of CHIR99021 (6 µM instead of 4 µM) was added on Day 0. The medium was exchanged to CDM without any supplements on Day 1 and CDM with 5µM IWP2 was added on Day 3. On Day 5 the cells were incubated with CDM without supplements for 2 days and on Day 7 the differentiation protocol was concluded by replacing the medium to CCM. The appearance of the first hiPSC-derived cardiac myocytes (hiPSC-CMs) between Day 8-15 was evaluated by monitoring the spontaneous contraction of the cells, as evidence for successful cardiac differentiation. The hiPSC-CMs were then maintained in CCM and the medium was changed every 2-3 days (1.5-2 ml for each well of a 12-well plate) for further maturation.

3.1.1.5 Metabolic selection and digestion of hiPSCs

The metabolic selection was performed between Days 25-40 in order to enrich the cardiomyocyte population. This is based on the substitution of the energy source from glucose to lactate due to the fact that only hiPSC-CMs would be able to metabolize lactate. To do so, the medium was exchanged to Cardio Selection Medium (CSM) for 2 consecutive medium changes (4 days in total). After selection, the medium is changed back to CCM and after 1-2 weeks the hiPSC-CMs were enzymatically dissociated to be seeded for carrying out the experiments. For this purpose, the cells were washed twice with pre-warmed versene solution and were then incubated at 37 °C with Collagenase II solution (400 U/ml, 500 µl per each well of a 12-well plate) for up to 2 hours, until the majority of beating areas detach. The rest of the beating areas were gently washed afterward using a 1000 µl pipette and the cells suspension was transferred to a 15 ml tube for centrifugation (at room temperature, 200 rcf, 5 min). After removing the supernatant, the cell pellets were resuspended in Trypsin solution (0.25%, approximately 500 µl for contents of each well), mixed gently by a 1000 µl pipette and were incubated at 37 °C for 8-10 min. After 4-5 minutes, the cells were mixed by shaking the tube. The digestion was monitored by collecting about 10 µl of the suspension, spreading on a 10 cm plate and observing the singularized cells under the microscope. When the majority of the cells were singularized, Trypsin was neutralized by adding double the volume Cardio Digestion Medium. Subsequently, the cells were centrifuged (at room temperature, 200 rcf, 8 min), resuspended in Cardio Digestion Medium and passed through a 40 µm cell strainer to remove the matrix residuals. The hiPSC-CMs were then counted using an automated cell counter and

the desired cell numbers were seeded in proper plates for experiments. Typically, 40,000-50,000, 300,000-500,000 and 1-1.5 million cells were seeded in a 96-, 24- and 12-well plates.

3.1.2 Cultivation of HEK293

HEK293 cell line were cultured in DMEM medium, containing 10% FBS, 1% Penicillin (10000 U/ ml)/ Streptomycin (10000 µg/ ml) in 10 cm culture dishes (Sarstedt, Germany) at 37 °C in a 5% CO_2 incubator. For splitting, the cells were washed with DPBS and were incubated with 0.05% Trypsin for 2-5 min at 37 °C, until the cells detached. Then Trypsin was neutralized by adding double the amount of culture medium and the cell clamps were singularized by pipetting. The cells were centrifuged at 400 rcf for 5 min, counted using an automated cell counter (Countess, Thermo Fisher Scientific, Darmstadt, Germany), and the desired number of cells were seeded in a new plate.

3.1.3 Preparation and cultivation of neonatal rat cardiac myocytes

Newborn Sprague-Dawley rats (0-1 day old, minimum 10 pups) were euthanatized by decapitation, the heart was then extracted with forceps, the atria were removed, and the ventricles were transferred to a 6 cm dish containing CBFHH on ice. The ventricles were further minced into small pieces, were transferred to a cell stirrer with 15 ml of the collagenase II and pancreatin solution and the first digestion was performed for 20 min. The supernatant was collected and discarded, since most cells at this step are erythrocytes. Subsequently, five digestion steps with 20, 25, 25, 15 and 10 min were followed and each time, the digested cells were collected in 2 ml FBS, centrifuged at 200 rcf for 5 min, resuspended in 4 ml FBS and kept in the incubator till all the steps were completed. Afterward, the cell suspensions were pooled, centrifuged at 200 rcf for 5 min and were resuspended in 10 ml of pre-plating medium. After passing through a 40 µm filter, the cells were pre-plated for 75 min on a 10 cm dish in a 1% CO_2 incubator at 37 $^{\circ}C$. Pre-plating resulted in the attachment of the fibroblasts (NRCF) to the dish, whereas the medium containing the NRCMs was then collected and the cells were counted using a countess automated cell counter (Thermo Fisher Scientific, Darmstadt, Germany). The desired number of cells were seeded in a new plate and maintained in a 1% CO_2 incubator at 37 $^{\circ}C$.

3.1.4 Preparation and cultivation of human myocardial slices

The preparation of slices was performed in collaboration with Prof. Andreas Dendofer (Walter-Brendl center, LMU). Myocardial tissue specimens were obtained from the Clinic of Thoracic and Cardiovascular Surgery (Bad Oeynhausen, Germany) or by the Clinic of Cardiac Surgery (University Hospital of Munich, Germany). Recipients of heart transplantation surgeries had provided informed consent to the scientific use of the explanted tissue, and the procedure has

been approved by the respective ethics boards. Left ventricular sections were cleaned of the residual artery or fat tissue and cut to 1x1 cm^2 block using a razor blade. The tissue was embedded in 4% low-melt agarose gel and cut into 300 µm slices using a vibratome (VT1200s, Leica) with 1.5 mm vibration amplitude, 0.07 mm/s advancing rate and 80 Hz vibration frequency in cooled (4 °C) slicing buffer. Prepared slices were transferred one by one to a 10 cm dish using sterile forceps and the agarose gel was removed from the surroundings using a scalpel. The orientation of cardiac myocyte fibers was determined and the autoclaved plastic triangles were glued to the two ends of the muscle fibers using Histoacryl surgery glue. The extra parts of the tissue were then trimmed and the slices were transferred to the cold slicing solution in a 50 ml tube and were transported to the Institute of Pharmacology and Toxicology on ice. Meanwhile, the biomimetic culture chambers were filled with 2.4 ml slice culture medium and were mounted to the MyoDish setups inside a 37°C incubator with 5% CO_2. The chambers were previously sterilized by rinsing with pure isopropanol and placing under UV light overnight. Upon mounting the chambers, the baseline was determined and if not in the range of -7000 to -12000 units, the position of the recording magnet was adjusted accordingly. The chambers were incubated for at least 30 min at 37°C prior to mounting the slices inside. The slices were transferred one by one into the culture chambers by picking up one of the triangles using sterile forceps and then the proper holes on the triangles were hooked in the elastic and fixed wires, respectively (**Figure 3.1**). Subsequently, the chamber was mounted into the MyoDish setup, the pre-defined stimulation program (50 mA, 1 pulse with 1ms duration, 0.5 Hz frequency) was initiated, and the preload was adjusted to 1 mN. To do so, first the linear drive screw was loosened using an Allen key until no contraction was visible, then it was tightened until a stable contraction was seen and tightening continued to the point that the baseline shifted 1000-1200 units upwards.

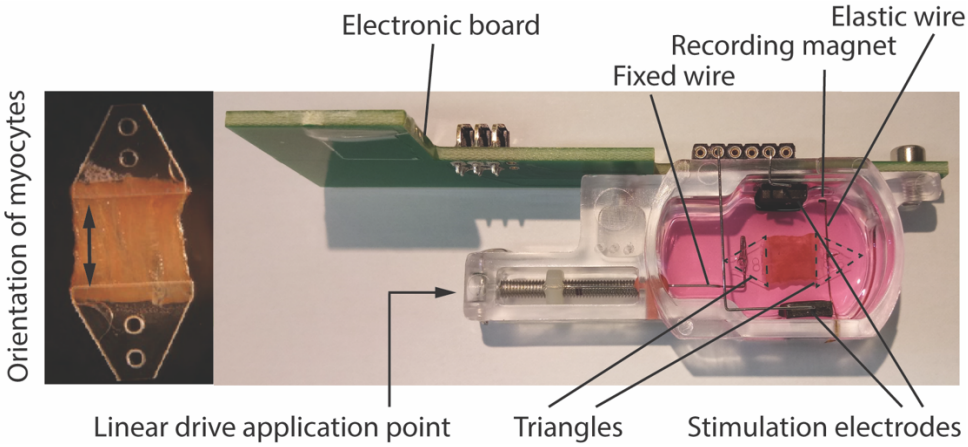

Figure 3.1 Biomimetic tissue culture chambers for cultivation of human myocardial slices.

A detailed view of the tissue structure and the biomimetic tissue culture chamber are depicted. The tissue was glued to the triangles (left) and was mounted into the culture chambers (right).

The slices were cultured under constant mechanical and electrical stimulation with rocking at 60 rpm to agitate the medium. After 24 hours, the preload was adjusted to 1 mN again as described above. The medium was changed every other day with slice culture medium and the slices were maintained in biomimetic chambers for at least 2 weeks before starting the experiments.

3.2 Molecular Biology and cloning techniques

3.2.1 Polymerase chain reaction

Polymerase chain reaction (PCR) was performed in order to amplify any intended DNA fragment, to add restriction enzyme cutting sites or to introduce point mutations during cloning procedures. Specific primers were designed using the Primer3 (v4.1) web tool and the specificity and melting temperature (T_m) were checked using NCBI Primer blast. Depending on the size and GC content of the desired DNA fragment, different enzymes and buffers were used. For usual purposes, AccuPrime *Pfx* DNA polymerase was used in the following reaction:

Component	**Volume**	**Final concentration**
10X AccuPrime *Pfx* reaction mix	2 µl	1x
Specific forward and reverse primer mix (10 µM each)	0.6 µl	0.3 µM each
AccuPrime *Pfx* DNA polymerase	1 µl	2.5 U
Template DNA (100-200 ng)	X µl	
DMSO (optional)	1 µl	
Nuclease-free water	Fill up to 20 µl	

Then the reaction was mixed by pipetting, briefly centrifuged, and were incubated for a 3-step or 2-step (preferred for long primers with high T_m) PCR in the following temperatures using a thermocycler:

Step	**3-step PCR**		**2-step-PCR**	
	Temp.	Time	Temp.	Time
Initial denaturation at 95°C for 2 min, followed by 35 cycles:				
Denaturation	95°C	15 s	95°C	15 s
Annealing	55-64°C	30 s	-	-
Extension	68°C	1 min/kb	68°C	1 min/kb
Final extension at 68°C for 10 min, followed by holding at 4°C.				

For complex fragments with a higher rate of error or mutation, Phusion DNA polymerase was used in combination with the High Fidelity (HF) or GC-rich buffer depending on the GC content of the target DNA:

component	Volume	Final concentration
5x Phusion HF or GC Buffer	4 µl	1x
10 mM dNTPs	0.4 µl	200 µM
Forward and reverse primer mix (each 10µM)	2 µl	0.5 µM each
Template DNA (100-200 ng)	X µl	
DMSO (optional)	0.6 µl	3%
Phusion DNA polymerase	0.2 µl	1 U
Nuclease-free water	Fill up to 20 µl	

After mixing, the tubes were incubated as the following:

	Temp.	Time
Initial denaturation at 98°C for 30 seconds, followed by 35 cycles:		
Denaturation	98°C	10 s
Annealing	45-72°C	30 s
Extension	72°C	30 seconds/kb
Final extension at 72°C for 10 min, followed by holding at 4°C.		

3.2.2 Agarose gel electrophoresis

For purification of an expected PCR product or a cut fragment, agarose gel electrophoresis was performed. For separation of larger fragments (>1 kb), 0.7-1% agarose gels and for the shorter fragments 1.5-2% agarose gels were prepared by dissolving the proper amount of agarose powder in approximately 80 ml TAE buffer. The solution was boiled in a microwave until the agarose was completely dissolved. The solution was then cooled down under running water and ethidium bromide was added at a final concentration of 0.5 µg/ml. The gel was cast by pouring the solution into the gel tray with the proper combs inserted. After 15-30 minutes the gel was transferred to an electrophoresis chamber filled with TAE buffer and the combs were removed. After adding the loading buffer to the DNA samples, the samples as well as 100 bp and 1000 bp ladders were pipetted into the gel. By applying 120-140 V and 400 mA to the gel, the DNA was migrated for the intended duration and then using a UV transilluminator (excitation at 254-366 nm), the ethidium bromide-DNA complex was visualized (emission at a visible range of orange-red, 590 nm).

3.2.3 Gel extraction

In order to prevent UV-induced mutations, low intensity of UV light (higher wavelength, about 366 nm) was used to visualize the DNA bands. The gel piece including the desired DNA band was excised using a sterile scalpel and collected in a 1.5 ml tube. For DNA extraction, the QIAquick gel extraction kit was used according to the provided protocol. Briefly, depending on the weight of the gel, the proper amount of QG buffer (3 times the weight/volume of the gel)

was added and the tube was incubated in a thermo-shaker block at 50 °C and shaking rate of 500 rpm, until the gel was completely dissolved. Then, 1 time the weight/volume of the gel isopropanol was added and after brief mixing the solution was transferred to a QIAquick column placed inside a 2 ml collection tube. After centrifugation for 1 min at 13000 rpm, the flow-through was discarded and 0.5 ml QG buffer was added to the column to remove residual agarose by another centrifugation step. After discarding the flow-through, 0.75 ml PE buffer was added to the column and incubated for 2-5 mins to wash the DNA. Then the PE buffer was removed by centrifugation, the column was transferred to a new 1.5 ml tube, and 20 µl of DNase/RNase-free H_2O was added to the center of the membrane inside the column to elute the DNA. After 1 min incubation, the column was centrifuged for 1 min and the flow-through containing the purified DNA was collected. DNA concentration was determined by measuring the absorbance at 260 nm using a Nanodrop.

3.2.4 Oligonucleotide annealing

To clone small (<100bp) synthetic fragments (such as a repetitive complementary sequence of miR-365) into a vector plasmid, the intended oligonucleotides (top and bottom strands) including cutting sites for the desired restriction enzymes as overhangs, were ordered to be synthesized. The oligonucleotides were first dissolved in nuclease-free water (100 µM concentration) and the annealing was performed as follows:

Component	Volume
10X annealing buffer (T4 DNA ligase buffer)	5 µl
Top strand (100 µM)	5 µl
Bottom strand (100 µM)	5 µl
Nuclease-free water	Fill up to 50 µl
Mixed, incubated at 95°C for 3 mins, gradually cooled down to 25°C (2% ramp) and held at 4°C.	

Subsequently, 1 µl of the annealed oligonucleotide was diluted in 1:100 ratio with nuclease-free water and 1 µl of the dilution (final amount of 100 fmol) was then used for ligation.

3.2.5 Endonuclease restriction digestion

Digestion using specific restriction enzymes was performed either for cloning purposes or for determining the integrity of a region of interest. For this, 1 µg DNA was digested with 5-10 units of one or two enzymes for a single- or double- digestion, respectively. For each enzyme, an optimized buffer and incubation condition (time and temperature) was used according to the company's instructions. When possible, high-fidelity enzymes were used preferably. After cutting, either the enzymes were heat-inactivated, or the sample was run on a gel was extracted as described above (3.2.3).

3.2.6 Antarctic phosphatase treatment of digested DNA

To prevent the self-ligation of the vector during cloning, especially when the plasmid was cut with only one restriction enzyme or with enzymes that create blunt ends, dephosphorylation of the 5' ends of the vector was carried out as following:

Component	Volume
DNA (1 µg)	X µl
Antarctic phosphatase	5 U
Antarctic phosphatase reaction buffer (10x)	2 µl
Nuclease-free water	Fill up to 20 µl
Mixed, incubated at 37°C for 30 mins, heat inactivation at 80°C for 2 min.	

3.2.7 DNA ligation

For combining two DNA fragments that were previously digested with identical restriction enzymes, DNA ligation was performed using T4 DNA ligase. This enzyme facilitates the formation of a phosphodiester bond between a 5' phosphate and a 3' hydroxyl ends of two DNA fragments, in this case the insert and vector. For an efficient ligation, the amount of insert and vector in the ligation reaction was calculated using the formula below:

Required insert mass (ng) = (3-5)* insert length (bp) * vector mass (ng) / vector length (bp)

Component	Volume
T4 DNA ligase buffer (10x)	1 µl
Vector DNA	10 - 50 ng
Insert DNA	As calculated above, for 1:3 or 1:5 vector to insert ratio
T4 DNA ligase	1 µl
Nuclease-free water	Fill up to 10 µl
Mixed, incubated at room temperature for 10 min for cohesive ends, or 2 hours for blunt ends, alternatively, incubated at 16°C overnight. Followed by heat inactivation at 65°C for 10 min.	

The ligated plasmid was then transformed into a proper bacterial strain for amplification.

3.2.8 DNA precipitation with glycogen

After ligation, to achieve higher DNA recovery and therefore enhanced transformation efficiency, ligated plasmid was purified by precipitation. To do so, 2 µl of glycogen (molecular biology grade), 6 µl of 7.5 M ammonium acetate and 45 µl 100% ethanol were added to 10 µl of ligation reaction (prepared in 3.2.7). The solution was mixed by pipetting and centrifuged at 12000 rcf and 4°C for 20 min. The supernatant was discarded and the DNA pellet was washed twice with approximately 100 µl 70% ethanol. After final centrifugation at 14000 rpm for 10 min and at 4°C, the pellet was air-dried, was resuspended in 10 µl nuclease-free water and was directly transformed into the intended bacterial strain.

3.2.9 Mutagenesis of plasmid DNA

After cloning of df-reporter constructs carrying the 3' UTR of the miR-365 targets, specific mutations were introduced within the binding sites of this miRNA using a 2-step site-directed mutagenesis PCR strategy. To do so, a specific forward primer (F1) containing the mutated binding site and a few nucleotides upstream of the binding site was designed (approximately in the middle of the inserted 3' UTR). The first PCR was then carried out with the wild type df-reporter as the template, the F1 primer and a reverse primer (R1), binding to the end of the 3' UTR and bearing the desired restriction site at its end. The product of this PCR was isolated after running on an agarose gel and was used as a reverse primer in the second PCR reaction. The forward primer in this reaction (F2) was designed to bind to the other end of the cloned 3' UTR and contained another restriction enzyme cutting site at its 5' end. The wild type df-reporter was used again as the template. Therefore, the product of the second PCR was the full-length 3' UTR with specific mutations within the miR-365 binding site (PCR was done as described in 3.2.1). After purification, the product and the native vector were cut using the intended restriction enzymes and ligation was carried out as described previously.

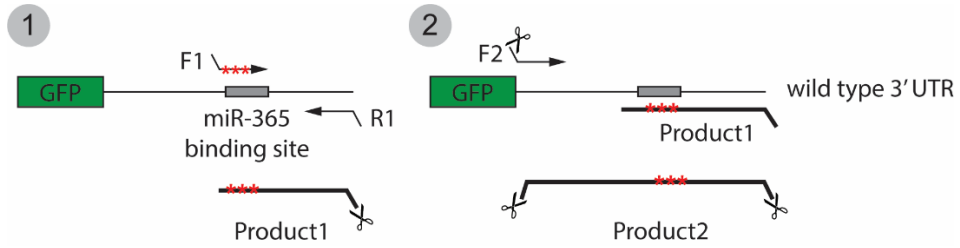

Figure 3.2 Site-directed mutagenesis strategy

Scheme representing the 2-step mutagenesis PCR strategy. A first PCR (1) was performed using primers F1 and R1 and the wild type df-reporter as a template. The primer F1 contained 3 mutations (red stars) within the binding site of the miR-365 seed region. The R1 primer contained a restriction site in its 5' (marked with scissors icon). The product of the first PCR was then used as a reverse primer for a second PCR. F2 primer included another cutting site in the 5' region. The second PCR yielded the full length of the intended 3' UTR with a mutated binding site for miR-365 and can be cut using the introduced restriction enzyme cutting sites at the two ends.

3.2.10 Transformation of bacteria

For amplification of plasmids, different strains of electrocompetent *E. coli* were used. For common plasmids, DH10B or Stbl2 strains were used, whereas for unstable plasmids prone to recombination (such as AAV vectors), SURE cells were preferred. Frozen aliquots of electrocompetent cells (50 µl) were thawed on ice for approximately 30 minutes. Subsequently, 2 µl of the ligated plasmid was added to the cells, mixed gently by only one time pipetting and the mixture was immediately transferred to a Gene Pulser 0.1 cm cuvette. The cuvette was placed in a Bio-Rad MicroPulser and the cells were stimulated by applying a brief 1.8 kV electric pulse. Afterward, 200 µl LB medium was added to the electroporated cells and the

mixture was transferred to a 1.5 ml tube. The tubes were incubated in a thermomixer at 37°C for 45-60 min shaking at 500 rpm for initial growth. The bacteria were then plated on LB agar plates containing the proper antibiotic following a 4-step culture method in order to obtain single bacterial colonies. The plates were then incubated at 37°C overnight for further bacterial growth and colony formation.

3.2.11 Amplification and purification of plasmids

After overnight culture in antibiotic-containing plates, only the bacteria that were properly transformed with the plasmid (containing antibiotic resistance gene) were able to survive and form colonies. To determine the integrity of the transformed plasmid, 3-10 colonies were picked from the LB agar plates and were sub-cultivated in 5 ml LB medium containing the proper antibiotic for miniprep. The cultures were incubated in a shaker-incubator overnight at 37°C and 180 rpm. For sensitive constructs susceptible to recombination, instead, bacteria were first cultured in 50 µl LB medium incubated in a thermomixer for 1 hour at 37°C and 500 rpm and only 20 µl of this pre-culture was used for sub-culturing step in 5 ml LB. The additional 30 µl was stored at 4°C to be used for further propagation, in case the colony was validated to have the correct construct. For common plasmids, only after the overnight incubation of the sub-culture, 100 µl were transferred to a 1.5 ml tube and kept as a backup at 4°C.

The mini culture was then centrifuged at 10000 rcf for 5 min. The LB medium was removed and the bacterial pellet was lysed for extraction of plasmid DNA using a column-based miniprep kit. To do this, the pellet was resuspended in the proper buffer and after adding the lysis buffer, the sample was mixed by inverting and the cells were lysed for 5 min at room temperature. Then the lysis buffer was neutralized and the samples were centrifuged for 10 min at 10000 rcf to sediment the cell debris. Subsequently, the supernatant containing the DNA was transferred to a DNA capturing column. These columns were positively charged and had an affinity to absorb negatively charged DNA. The extraction followed by washing steps and centrifugation to remove residual RNA and proteins. The column was finally transferred to a new 1.5 ml microcentrifuge tube, and the DNA was eluted using the proper amount of nuclease-free water (e.g., 20 µl for miniprep). The concentration of the plasmid DNA was determined using the Nanodrop. For validation of the plasmid, either specific restriction digestions were performed or the samples were sequenced using specific sequencing primers. Sanger sequencing was performed by Eurofins Genomics (Ebersberg, Germany) and the results were blasted against the desired sequence using NCBI BLAST tool or MacVector or SnapGene software. After validation of the plasmid DNA, the backup bacterial cultures were used in order propagate the plasmid DNA on larger scales. For various purposes, midi (200 ml LB, about 0.2 mg yield), maxi (800 ml LB, 1-2 mg yield) or giga (1600 ml, 5-7 mg yield) cultures were prepared and after overnight incubation at 37°C and 180 rpm plasmid DNA was

isolated using the proper column-based kit (PureLink, Invitrogen) following the manufacturer's instructions.

3.2.12 Adeno-associated virus (AAV) production

For the production of AAVs, the intended DNA fragment was first cloned into an AAV backbone. After validation of the construct, maxiprep was performed to obtain at least 450 µg of the plasmid. Specific helper plasmids were used to obtain various serotypes of AAV (e.g., in this study pDP6rs for AAV6). For propagation of the helper plasmids gigaprep was performed. For packaging, HEK293T cells were grown as described before (3.1.2) and were plated cell factories in the HEK culture medium. After reaching 70% of confluency (usually 1-3 days after seeding), the cells were co-transfected with the following transfection mix:

	Component	**Amount**
Mix 1	transgene AAV plasmid helper plasmid DMEM	445 µg 1525 µg 466.40 ml
Mix 2	PEI transfection agent DMEM	3.94 mg 466.4 ml
Mixed separately, combined together, mixed by vortexing and incubated at room temperature for 15 min.		

The mix was then added to the cell factory along with 500 ml fresh HEK culture medium and the factories were transferred to the incubator for 72 hours. Afterwards, the cells were harvested by shaking the cell factory and collection of the cells and medium in 500 ml conical tubes. The cell factories were washed once with PBS to ensure transferring of any remaining cells to the collection tubes. After centrifugation at 250 rcf for 15 min, the medium was removed and the cells were washed twice with PBS to remove the residual medium. The cells were then lysed by adding the AAV lysis buffer and repeated freeze-thaw cycle. To do so, the tube containing the cells was placed in liquid nitrogen and was then thawed in a 37°C water bath 3 times. Then, the cells were treated with benzonase (0.5 µl per 1 ml cell lysate, incubation at 37°C for 30 min). Subsequently, the viruses purified from the cell lysate using an iodixanol density gradient ultracentrifugation. For this purpose, 15%, 25%, 40%, and 60% iodixanol OptiPrep gradients were prepared and were pipetted gently on top of the solution containing viruses, into a QuickSeal tube consecutively. After balancing the tubes with a precision of 0.01 g, ultracentrifugation was performed at 60,000 rpm and 4°C for 2 hours using an Optima L-80 XP Rotor, Type 75 Ti, with the acceleration rate adjusted to maximum and deceleration sat at 7. After centrifugation, AAVs were collected by insertion of a syringe into the 40% iodixanol phase. Another needle was inserted in the uppermost phase in order to avoid a vacuum.

Since iodixanol might cause cytotoxicity, the collected AAVs were then purified in lactate and were simultaneously further concentrated using a Vivaspin 20 (MWCO 100000). To do so, the column was washed and equilibrated with lactate followed by 5 min centrifugation at 4000 rcf

and room temperature. The virus was then diluted in lactate in a 1:6 ratio and was transferred to the equilibrated Vivaspin column. The solution was centrifuged at room temperature and 4000 rcf, until the liquid above the filter was reduced to 1 ml. Then the flow-through was discarded, an additional 9 ml lactate was added to the remaining viruses and centrifugation was continued until 500-1000 µl AAVs remained. AAVs were transferred to cryovials and were stored at -80°C for long-term storage.

3.2.13 AAV titration

In order to quantify the concentration of the AAVs, a quantitative PCR was performed on the viral DNA as well as DNA standards with known concentrations. For the preparation of the standards, either the same transgene plasmid DNA used for AAV production, or a plasmid with a similar size was selected and the copy numbers and the concentration of DNA were correlated using the following formula:

$$\text{concentration } (g/ml) = \frac{\text{plasmid molecular weight } (g/mol) * \text{standard copies } (ml^{-1})}{6.022 * 10^{23}\ (mol^{-1})}$$

Then, serial dilutions in the range of 10^9-10^{14} were prepared. For the AAVs, first the capsid was digested to release the viral DNA. To do so, 10 µl of the produced AAV was mixed with 10 µl of TE buffer and 20 µl of 2 M NaOH. After mixing, the solution was incubated at 56°C for 30 min and then 960 µl of 40 mM HCl was added to neutralize the reaction. Subsequently, 1 µl of the DNA was used for qPCR as indicated:

Component	Volume	Final concentration
AAV lysate or standard	1 µl	
Primer mix (10 µM each, usually SV40)	1 µl	0.4 µM each
SYBR Green Mix (2x)	12.5 µl	1X
Nuclease free water	10.5 µl	

The following PCR program was performed in a StepOne Plus real-time PCR machine:

	Temp.	Time
Initial denaturation at 95°C for 10 min, followed by 40 cycles:		
Denaturation	95°C	15 s
Extension	60°C	1 min

The Ct values (defined as the number of cycles required for the fluorescent signal to exceed the threshold of the background fluorescence) were then exported and a standard curve was generated using the obtained Ct values for the standards and the copies of the viral genome was determined by comparing the Ct values of the AAV to the standards (**Figure 3.3**). Typical AAV yield using the abovementioned protocol was 10^{12}-10^{13} viral genomes per 1 ml (vg/ml).

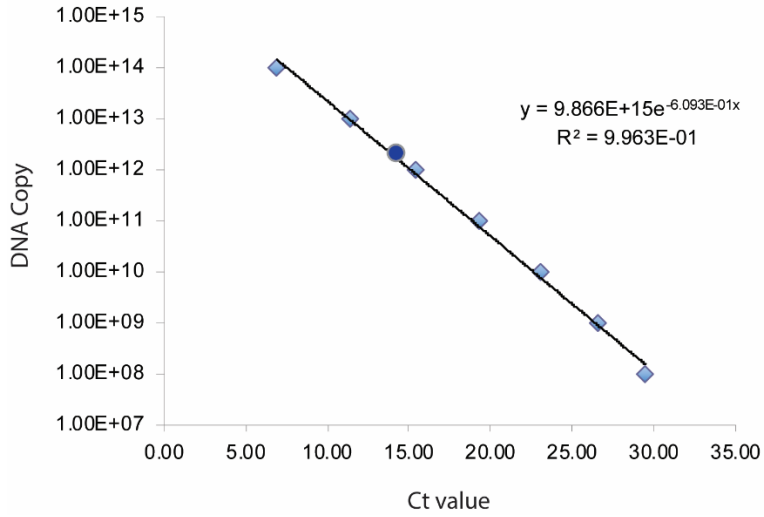

Figure 3.3 Representative AAV titration curve

DNA copy number (log scale, x-axis) against the ct value of the qPCR (y-axis). Seven samples with known amounts of plasmid copy number were used to generate this titration curve (squares) and the unknown AAV titer (circle) was then extrapolated.

3.3 MiR-365 manipulation and functional assays

3.3.1 MiR-365 manipulation in NRCMs

NRCMs were treated one day after seeding, either by transfection of oligonucleotides or by infection via AAVs. This way, the dead cells and debris were removed by washing. For transfection, approximately 40,000-50,000, 500,000 or 1 million cells were seeded per one well of 96-, 12- or 6-well plates, respectively. The next day, lipofection mix was prepared by diluting mimic-ctrl or -365 (at a final concentration of 25-50 nM) as well as Lipofectamine 2000 in OptiMEM. These two solutions were mixed properly and the mixture was incubated at room temperature for 15-20 min (total lipofection mix volume was 50, 250, or 500 µl for 96-, 12- or 6-well plates, respectively). Meanwhile, the cells were washed twice with pre-warmed PBS and similar volumes of NRCM culture medium without antibiotics were added to each well. After incubation time, lipofection mix was added to the wells and was mixed by shaking the plates. The cells were incubated in a 37°C incubator with 1% CO_2 for 6-8 hours before the medium was changed to a normal NRCM culture medium and the cells were further incubated for 48 hours before fixation, RNA isolation or functional assays. For infection of NRCM, the next day after seeding, the proper amount of AAVs was mixed with the NRCM culture medium to reach a concentration of 10^3-10^5 viral genomes per cell (vg/cell). If necessary, the mixture was filtered using a 0.2 µm filter and the AAV-containing medium was added to each well after the cells were washed two times with PBS. The next day, the medium was exchanged to remove the residual viruses and the cells were further incubated for 3-7 days so that a robust expression of the transgene was achieved.

3.3.2 Transfection of HEK293 cells for df-reporter assay

Double fluorescent (df-) reporter assays were performed to validate the direct interaction between miR-365 and its corresponding binding sites in the 3' UTR of the predicted target genes. For this, HEK293 cells were seeded in a 96 well µ-plate with black walls (IBIDI) at the density of 40,000 cells per well and were co-transfected with 0.1 µg of df-reporter DNA plasmid and mimic-365 or -ctrl at a final concentration of 50 nM per well. For transfection, oligonucleotides as well as Lipofectamine 2000 were mixed separately with OptiMEM. Then the solutions were combined, properly mixed and were incubated at room temperature for 15-20 min for liposomes to generate. Meanwhile, fresh HEK medium without antibiotics was added to the plates and the lipofection mix was added to the cells after the incubation. The medium was replaced with antibiotics-containing medium 6-8 hours post-transfection. After 48 hours, the cells were fixed by 10 min incubation with 4% PFA, washed 3 times with PBS and a mixture of 50% Glycerol containing DAPI was added to the cells. The plate was covered with an aluminum seal and stored at 4°C.

3.3.3 MiR-365 manipulation in hiPSC-derived cardiac myocytes

After Day 60, hiPSC-CMs were replated in 96 well µ-plates (IBIDI) for optical AP recordings and immunofluorescent staining, or in 24- or 12-well plates, for RNA extraction. After re-plating, hiPSC-CMs were cultured for at least 7-10 days prior to the experiments to regain the contractility. To increase the intracellular levels of miR-365, the cells were transfected with synthetic mimic-365. Inhibition of the endogenous miR-365 was achieved by transfection of LNA-antimiR-365. Non-targeting oligonucleotides with the same chemistry (mimic-ctrl and antimir-ctrl) were used as negative controls. The cells were transfected using Lipofectamine RNAiMAX to reach a final concentration of 25 nM oligonucleotides and the effects were measured 48 hours later. Infection with AAV6 was performed by mixing 10^3-10^5 vg/cell in CCM and passing the mixture through a 0.2 µm filter. The filtered virus-containing medium was added to the cells and the cells were incubated for 24 hours before exchanging the medium to fresh CCM. After 3-5 days, the effect of the transgene was evaluated.

3.3.4 Transfection of Myocardial slices

Myocardial slices were transfected with mimic-ctrl or -365, antimiR-ctrl or -365 and a Fluorescein amidite (FAM)-labeled mimic-control. For transfection of myocardial slices, 40 µl of oligonucleotides (stock concentration 20 µM, 1 nmol in total) and 30 µl Lipofectamine RNAiMAX were separately diluted in 150 and 170 µl of pre-warmed OptiMEM (volumes for transfection of one slice in a biomimetic culture chamber). These two solutions were combined and completely mixed by pipetting and were incubated at room temperature for 15-20 min so that the liposomes form in the solution. Shortly before the end of the incubation time, the

biomimetic culture chamber was removed from the MyoDish setup, the entire volume of medium was removed, and 1.6 ml of the pre-warmed slice culture medium without antibiotics was added to the slice. Then the lipofection mix was added to the chamber and the chamber was immediately transferred back to the MyoDish setup inside the incubator. The medium was replaced with fresh and warm slice culture medium after 6-8 hours and the changes were monitored for the next 48 hours.

3.3.5 Reporter activity assay

In the present study, df-reporter assays were performed for two purposes: first, for validation of the interaction between miR-365 and its binding sites within the 3' UTR of the predicted target genes. This experiment was done in HEK293 cells, by co-transfection of df-reporter plasmids and mimic-ctrl or -365. The plasmids comprised of tdTomato gene deriving RFP expression as an internal control, and eGFP followed by 400–600 base pairs of the 3′ UTRs of the ion channel genes. The second experiment was carried out in hiPSC-CMs, in order to determine the efficiency of miR-365 manipulation in these cells. For this, different df-reporters were used that contained 3 repetitions of miR-365 binding site after eGFP sequence (df-3xmiR-365). In these constructs, mCherry was used as an internal control. Since transfection of such large plasmids into the hiPSC-CMs was not robust, these constructs were re-cloned into an AAV backbone and AAV6 viruses carrying df- constructs with either 3xmiR-365 binding sites or a scrambled binding site were produced as described above. The hiPSC-CMs were first transduced with these viruses and after three days, were transfected with miR-365 mimics or antimiRs as described above. In both experiments, 48 hours after transfection, the cells were washed with PBS, fixed using 4% PFA and mounted with 50% Glycerol containing 1:100 DAPI. After 30 min to ensure incorporation of DAPI in the nucleus, the fluorescent intensities of GFP, RFP and DAPI were measured using an automated program in Metamorph software which controlled a Zeiss Axio Observer Z1 inverted microscope equipped with a 10x Plan-Apochromat objective and a digital camera. The program included the acquisition of images in GFP, RFP and DAPI channels from 4 different regions per well and with two different exposure times (high and low). After the acquisition, the images were analyzed using another automated program in Metamorph software. The analysis program identified the single cells (based on DAPI signal) and extracted a reliable GFP and RFP intensity per cell by comparing the emission after higher or lower excitation time. The GFP/RFP ratio was then calculated for control and miR-365 manipulated cells by averaging the values acquired from hundreds to thousands of cells per condition.

3.3.6 Immunofluorescence

For staining the cells, 96-well µ-plate with black walls (IBIDI) was used. The cells were washed 2-3 times with PBS and were fixed with 100 µl 4% PFA in PBS for 10 min at room temperature. The cells were then permeabilized using 100 µl 0.2% Triton-X for 10 min, washed once and were incubated with the primary antibody (100 µl, for the proper dilutions refer to section 2.4) for 30 min at 37°C. The secondary antibody and DAPI were then diluted in PBS and after washing the cells 2-3 times with PBS, were added to the plate. The plate was incubated for 30 min inside a 37°C incubator protected from light. After incubation, the secondary antibody was washed away with PBS and 200 µl of 50% glycerol was added to each well. The plate was covered with an aluminum seal and was either kept at 4°C for up to 1 week or was proceeded for acquisition directly. For staining of human myocardial slices, the tissue was first embedded in OCT in the proper orientation depending on the types of sections intended afterward, and the cryomold was then placed on dry ice for instant freezing. Subsequently, 5µm longitudinal or transverse sections were prepared using a cryotome (Leica) sat at -20°C, were placed on microscopic glass slides and were incubated with wheat germ agglutinin (WGA) conjugated to a proper secondary antibody. The slides were incubated for 30 min at room temperature in a dark humid chamber in order to mark the plasma membrane. This was followed by DAPI staining for 15 min and Sudan Black treatment to reduce autofluorescence of the tissue. In both cases, images were acquired using the confocal microscope Leica TCS SP II.

3.3.7 Action potential recording using AAV-VSFP-CR

To measure the AP specifically in ventricular hiPSC-CMs, a genetically encoded FRET sensor was utilized. The plasmid carrying the sensor (pcDNA3.1/Puro-CAG-VSFP-CR, Addgene #40257) was purchased, the existing CAG promoter was exchanged to the ventricular-specific promoter MYL2 and the MYL2-VSFP-CR was re-cloned into an AAV backbone to produce AAV6, for robust delivery and expression in NRCMs and hiPSC-CMs [218,251]. The cells were seeded in 96-well µ-plates with black walls and transduced with 10^5 vg/cell of AAV6-MYL2-VSFP-CR. Since the MYL2 promoter was not very strong, the cells were monitored 5-10 days after infection to evaluate the expression of the sensor prior to miR-365 manipulation. When Clover-GFP and Ruby2-RFP were expressed visibly, the cells were transfected with miR-365 mimics and antimiRs. 48 hours post-transfection, the cells were washed with PBS and 200 µl pre-warmed (37°C) FRET buffer was added to each well and to an empty well for monitoring the temperature. The RFP and GFP intensities were acquired using an inverted microscope (Zeiss AxioObserver Z1) equipped with an oil immersion 40x objective. After choosing a region of interest, the perimeters of single cells were determined by drawing a line around and inside the cell (typically 1-5 cells per region, and 4-5 regions per well). A polychrome V light source (Till Photonics) and a 488 nm excitation filter were used to excite the cells at 480 nm. After

passing through a beam splitter (cxr565), the emission spectra at 560 nm (Clover GFP) and 656 nm (mRuby2 RFP) were detected independently using an Evolve 512 EMCCD camera (Visitron Systems). The setup was controlled using MetaFluor software (Visitron Systems). The temperature was kept above 30°C throughout the experiment using a manually-built heating system. For analysis and determining AP duration, the fluorescent intensities were first preprocessed using a custom-written Microsoft Excel macro to calculate the RFP/GFP ratios and separate the data acquired from each cell. The ratios and time for each cell were then imported to a custom-written Python script, where the AP duration at 50 or 90% of repolarization was calculated for each cell and Bazett's formula was applied for correcting the differences in beating frequency.

3.3.8 Action potential recording using ANEPPS

For AP recordings from the whole population of hiPSC-CMs, a voltage-sensitive dye di-8-ANEPPS was used. Similar to the AP recording via the FRET sensor, the cells were seeded in 96-well µ-plates and were transfected with mimics and antimiRs for 48 hours. Directly before the measurements, hiPSC-CMs were incubated with di-8-ANEPPS (5 µM final concentration) at room temperature for 10 minutes. Pluronic F-127 (at a final ratio of 0.05%) was added to improve the solubilization of the dye. After incubation, the cells were washed 2-3 times and warm FRET buffer was added to each well. The measurement was done similar to section 3.3.7 and the cells were excited at 488 nm while the changes in the dye's emission were measured at 620 and 560 nm. In depolarized membranes, F620/F560 was decreased. The analysis of AP duration was done with a different Excel macro and the same Python script to determine APD90 upon miR-365 manipulation.

3.3.9 Refractory period measurements in myocardial slices

The refractory period of slices was regularly recorded before and after transfection every 12 hours. This was done, using an automated stimulation protocol consisting of a second pacing impulse at defined intervals after each regular stimulus. The interval between the two stimulations (inter-stimulus interval) was gradually decreased from 1000 to 250 ms in scheduled steps of 30 s duration. The longest interval that failed to induce two distinct contractions was noted as the refractory period. The functional refractory period in ventricular myocytes closely correlates with AP duration, and therefore was used as a readout for changes in AP duration upon miR-365 manipulation in the slices.

3.4 RNA methods

3.4.1 RNA isolation from cultured cells

For RNA isolation, first, all the surfaces were sprayed with RNaseZap. Then, 1 ml TriFast (or Trizol, in case RNA was intended to be used for library preparation) was added to 0.4-1.5 million cells (the volume was adjusted for different cell numbers accordingly) and the cells were detached from the plates using cell scrapers. After detaching, the solution was pipetted a few times, was transferred to a clean nuclease-free 1.5 ml tube and was incubated at room temperature for 5 min to ensure complete cell lysis. Afterward, chloroform was added to the tubes (200 µl per 1 ml TriFast), the tubes were vortexed for 50 seconds, and were centrifuged at 4°C and 12000 rcf for 5 min. After centrifugation, an aqueous phase (upper phase, containing RNA), an interphase (containing DNA) and an organic phase (lower part, containing protein and lipids from the cell lysates) were observed. The aqueous phase was carefully transferred to a clean 1.5 ml microcentrifuge tube without disturbing the other phases. Then 0.5 µl RNA-grade glycogen and 500 µl of isopropanol (per 1 ml of TriFast) were added in order to precipitate the RNA. The solution was mixed and was incubated either at 4°C for 10 min or at -20°C overnight for maximum RNA yield. The samples were then centrifuged at 13000 rcf for 10 min in a precooled (4°C) centrifuge and then the supernatant was discarded. The pellet was washed two times with 1 ml of 75% Ethanol and centrifuged for 10 min at 4°C and 13000 rcf. After discarding the supernatant, the RNA pellet was air-dried for 5-10 min and was resuspended in 10-20 µl of nuclease-free water depending on the expected RNA amount. To facilitate the resuspension, the samples were heated for up to 2 min at 55°C in a thermomixer and were then kept on ice. The concentration of isolated RNA was determined using either a Nanodrop, or a gel-based method such as Bioanalyzer or TapeStation. For quantification of RNA using Nanodrop, after calibration with water, one drop of the RNA sample was placed on the device. The absorbance at 260 nm determined the RNA concentration, while 260/280 and 260/230 ratios reported the purity of RNA. Bioanalyzer and TapeStation were run according to the manufacturer's protocols and in addition to the concentration, providing information about the integrity of the RNA by reporting RNA Integrity Number (RIN). The RNA samples were then kept at -80°C for long-term storage.

3.4.2 RNA isolation from tissue

Snap frozen tissue was first homogenized by transferring into a BeadBug prefilled bead homogenization microtubes (1.0 mm diameter) and the addition of 1 ml TriFast (or Trizol). The tubes were then tightly closed and were placed in an MP FastPrep-24 homogenizer to be beaten at 4.0 m/s shaking rate for two rounds of 20 s with 1 minute rest in between. Complete

lysis was ensured when no tissue debris was observed. The supernatant was then transferred to a clean 1.5 ml tube and the RNA isolation steps were followed as described above (3.4.1).

3.4.3 Reverse transcription and qPCR of total mRNAs

In order to determine the gene expression changes quantitatively, the extracted total RNA was first reverse transcribed to cDNA using the Protoscript II enzyme (New England Biolabs, USA) according to the manufacturer's directions:

Component	Volume	Final concentration
Total RNA *(*100-1000 ng)	X µl	
oligo dT primer (50 µM)	1 µl	2.5 µM
dNTPs *(*10 mM)	1 µl	0.5 mM
RNase free H_2O	Add up to 12 µl	
Incubation at 65°C for 5 min. Removal from the thermocycler and addition of the following material on ice:		
5x Protoscript II reaction buffer	4 µl	1x
DTT (0.1 M)	2 µl	10 mM
Murine RNase inhibitor (40 U/µl)	1 µl	2 U/µl
Protoscript II reverse transcriptase (200 U/µl)	1 µl	10 U/µl
Incubation at 42°C for 1 hour, followed by inactivation of the enzyme at 80°C for 5 min.		

The yielded cDNA was centrifuged briefly, diluted to the concentration of 10 ng/µl and then either used for subsequent qPCR or was stored at -20°C for long-term storage. To determine the expression of the housekeeping as well as the specific genes, the PCR reaction was prepared accordingly:

Component	Volume	Final concentration
Diluted cDNA (10 ng/µl)	2 µl	
SYBR-Green mix 2x	6.25 µl	1x
Forward primer (20 µM)	0.25 µl	0.4 µM
Reverse primer (20 µM)	0.25 µl	0.4 µM
Nuclease-free water	3.75 µl	

After preparation of the reaction, the plate was covered with an optical adhesive seal, centrifuged briefly and placed in a StepOne real-time PCR machine using the cycling program stated below. Optionally, a melt curve analysis was performed, especially for each new pair of primers in order to evaluate the specificity of the primers. Ideally, only one peak was observed by running the melt curve analysis.

	Temp.	Time
Initial denaturation at 95°C for 10 min, followed by 40 cycles:		
Denaturation	95°C	10 s
hybridization	60°C	30 s
Elongation	65°C	1.5 min
Melt curve analysis (optional)		
	95°C	15 s
	60°C	1 min
	90°C	15 s

For determining gene expression changes, the Ct values were exported after the qPCR run and the relative expression changes were calculated using $2^{-(\Delta\Delta Ct)}$ method, where ΔCt was calculated as the difference between the Cts of each gene before and after treatment, and the ΔΔCt was obtained as the difference between the ΔCts of the target gene versus the control (housekeeping) gene.

3.4.4 Reverse transcription and qPCR of miRNAs

MiRNAs were reverse-transcribed using the miRCURY LNA Universal RT microRNA PCR protocol (Exiqon, Denmark). The RNA samples were adjusted to 5 ng/ µl using nuclease free water and the reaction was prepared as followed:

Component	Volume
RNA (5 ng/µl)	2 µl
nuclease free H_2O	5 µl
5x reaction buffer	2 µl
enzyme mix	1 µl

The reaction was mixed by pipetting and were then incubated at 42°C for 60 min, and the enzyme was then heat-inactivated at 95°C for 5 min. The samples were then maintained at 4°C. For qPCR, depending on the abundance of the intended miRNA, the samples were diluted in nuclease-free water (typically at 1:60) ratio and PCR reaction was prepared as following:

Component	Volume
Diluted sample	4 µl
SYBR-Green mix	5 µl
Specific Primer mix (U6 as housekeeping or miR-365)	1µl

The reaction was then mixed, centrifuged briefly and placed in a StepOne real-time PCR machine and the below mentioned program was performed. The resulting Ct values were then exported and miRNA expression changes were calculated using the $2^{-(\Delta\Delta Ct)}$ method.

	Temp.	Time
Initial denaturation at 95°C for 10 min, followed by 40 cycles:		
Denaturation	95°C	15 s
Extension	60°C	1 min

3.4.5 Small RNA-sequencing

After extraction of total RNA from healthy hiPSC-CMs, the integrity and concentration of RNA were determined by running the samples on a Bioanalyzer RNA pico chip according to the manufacturer's recommendations. Only samples with RIN greater than 8.5 were used for small RNA library preparation. For library construction, 700 ng RNA was processed according to NEBNext small RNA library prep kit instructions. Briefly, 3' and 5' sequencing adaptors were added to both ends of transcribed RNA molecules, the barcoded RNA was reverse-transcribed to produce the 1st cDNA strand and the fragments were amplified by PCR. This was followed by an AMPure XP bead-based size selection step to capture only smaller species of RNA including miRNAs. Libraries were then validated by running on a Bioanalyzer DNA kit, where the presence of a peak around 143 bp indicated a successful library preparation. The libraries were then sequenced on a HiSeq4000 (in this study a paired-end 100 bp sequencing was performed).

3.4.6 Next generation RNA-sequencing

For bulk RNA-seq, the integrity and quantity of total RNA isolated from untreated and miR-365-manipulated hiPSC-CMs were measured using Agilent 4200 TapeStation, RNA kit. Libraries were prepared from approximately 1 µg of RNA using the TruSeq Stranded mRNA kit (Illumina) according to the provided instructions. Briefly, the samples were first purified by magnetic beads to remove any unwanted salts or impurities. Then the total RNA was fragmented and 1st and 2nd strand of cDNA was synthesized. At each step, the resulted products were purified from the residual buffers and enzyme by bead-based purification. Then the unique sequencing adapters were added to both ends of each cDNA fragment and the libraries were amplified by PCR. The quality and quantity of libraries were determined using the TapeStation DNA kit. Fragments with a size range between 200-500 bp were observed with a peak at 260. The area under the curve yielded the concentration and molarity of each library and the libraries were pooled accordingly and were sequenced on a HiSeq4000, generating 150 bp paired-end reads.

3.4.7 Single cell RNA-sequencing

After transfection of the control hiPSC-CMs with mimic- and antimiR-365 for 48 h, the cells were proceeded for single cell capture, barcoding and library preparation using Chromium

Chromium single cell 3' (v2, 10x Genomics). To do so, first the cells were digested as described in section 3.1.1.5 with 2 extra washing steps with PBS to ensure removal of cell debris and residual medium. The viability of the cells was determined using a Countess automated cell counter and only samples with 90% viability and higher were considered for single cell RNA-seq. The digested hiPSC-CMs were kept at room temperature until 16,000 cells were combined with the reverse-transcription mixture (cells-RT mix). The Chromium single cell A chip was then filled with barcoded gel-beads, the cells-RT mixture and partitioning oil according to the manufacturer's instruction. After running the Chromium Controller, the resulting gel emulsions (GEMs, containing a single cell and a gel bead encapsulated in an oil droplet) were collected in PCR tubes and were incubated at 53°C to carry out the reverse-transcription. The library preparation continued by a cleanup step to remove the oil and residual enzyme and buffers and cDNA amplification. Then the quantity of the resulted cDNA was measured using the TapeStation high sensitivity DNA kit (D5000) in order to estimate the necessary PCR cycles to amplify the library in the subsequent steps. The cDNA was then fragmented, the sequencing adaptors and the sample indices were added, and the library was amplified. The quality and quantity of the resulting single cell libraries were determined using the TapeStation high sensitivity DNA (D1000) and the samples were sequenced on an Illumina HiSeq 4000 to obtain approximately 100,000 reads per cell.

3.5 Bioinformatics and statistical analysis

3.5.1 Analysis of small RNA-seq data

After sequencing FASTQ files were generated and the downstream analysis was performed using an in-house Galaxy server. Forward reads were trimmed of adapters (Trim Galore! version 0.4.2) using the option for auto-detection of Illumina adaptors. The quality of the FASTQ files was determined before and after trimming using the FastQC tool (version 0.69). The reads were mapped against miRBase21 mature and hairpin sequences and then quantified using the MiRDeep2 tool (version 2.0.0).

3.5.2 Analysis of Transcriptomics data

The generated FASTQ files were imported into the Galaxy server for analysis. The quality of the forward and reverse reads was determined (FastQC, version 0.69). Due to the low adapter score, no trimming was necessary. Reads were aligned against a built-in human genome (GRCh38 with GENCODE version 28 annotation) using RNA STAR (version 2.6.0) with default parameters. StringTie (version 1.3.6) was then used for transcript assembly (based on GENCODE version 28) and quantification, yielding transcript per million (TPM) and gene counts that can be used as an input for differential gene expression analysis tool. DESeq2

(version 2.11.40.2) was used to identify differentially expressed genes (DEGs) upon manipulation of miR-365. Genes with an expression change of greater than 30% (up- or downregulated, absolute log2 fold change of 0.4) and false discovery rate (FDR) of less than 0.05 between different treatments were considered as DEGs.

3.5.3 Analysis of single cell RNA-seq data

After sequencing, the raw base call files were converted to FASTQ files using CellRanger mkfastq (v2.1.0, 10x Genomics), resulting in 3 FASTQ files containing the mRNA reads, unique cell barcode reads and index reads. Using the CellRanger count module, the reads were mapped against the human genome annotation (GRCh38, GENCODE annotation v28), counted and attributed to each single cell based on the detected barcodes. The gene expression matrices of cells that passed the quality-control steps of CellRanger were then used for subsequent analysis in R package Seurat (v3.2) [246]. To ensure retaining of only high-quality cells, cells with less than 300 detected genes (possibly empty droplets containing ambient RNA) or more than 6500 detected genes (indicating droplets with more than one encapsulated cell) were omitted. As a further quality control step, cells with greater than 20% of mitochondrial reads were omitted from the downstream analysis, since high mitochondrial gene detection can be indicative of cell damage. Afterward, SCTransform [252] function was used for normalization and scaling of raw counts and regressing out the unwanted sources of variation (such as mitochondrial gene content and cell cycle stage). SCTransform also yielded the highly variable features that were used for linear dimensional reduction using principal component analysis (PCA). The components that contributed significantly to the dimensionality of the data were used for unsupervised graph-based clustering (resolution 0.1) and Uniform Manifold Approximation and Projection (UMAP) embedding and visualization. Adaptively-thresholded Low-Rank Approximation (ALRA) algorithm was then used to impute the dropout gene expression values. The significant marker genes of each cluster were identified using the Seurat FindAllMarkers function and employed to assign cell types to each cluster. Differentially expressed genes (with > 50% expression change, P-value < 0.05) between mimic- and antimiR-365 cells were detected with FindMarkers function of Seurat package based on implemented Wilcoxon Rank Sum test. Various plotting functions from the R package ggplot2 were used for generating heatmaps, UMAPs, feature and violin plots.

3.5.4 Gene ontology enrichment analyses

For gene-disease enrichment analysis, the predicted targets of miR-365 were exported from online miRNA-target prediction tool TargetScanv7.2 and disease enrichment was carried out using the online tool EnrichR[253] and the integrated Online Mendelian Inheritance in Man (OMIM) data collection. For bulk RNA-seq experiment, to determine the biological processes

associated with the DEGs upon miR-365 manipulation, ClueGO application (v2.5.6) [241] was used which was run within Cytoscape (v3.8.0)[242] network analysis tool. For this analysis, only terms with P-value < 0.05 and GO tree levels 3 to 8 were considered and plotted. Subsequently, gene set enrichment analysis (GSEA) was performed using the GSEA software (v4.0.3, Broad Institute)[254] on normalized reads ranked based on log2 fold changes (log2 FC) in mimic-365 compared to mimic-ctrl treated cells. The relevant gene sets were extracted from the available collections in the Molecular Signatures Database (MSigDB).

3.5.5 Statistics

All statistical tests were performed using GraphPad Prism (version 6 or 8). All quantitative data shown on bar graphs are presented as mean ± standard error of the mean (SEM). Optical recording results are reported as dot plots representing individual values and the median. To compare the two groups, first, the distribution of the data and the difference between variances were tested using the Kolmogorov-Smirnov test and *F* test, respectively. Depending on the distribution of data, unpaired two-tailed t-test or Mann-Whitney test were used to determine the statistical significance for data with or without normal distribution, respectively. To evaluate the differences before and after manipulation of miR-365 in myocardial slices two-tailed paired t-test was used to. Significance is depicted as * P < 0.05, ** P < 0.01, *** P < 0.001, **** P < 0.0001.

4 Results

4.1 MiR-365 as the primary miRNA controlling repolarization in human myocytes

4.1.1 Transcriptome and miRNome analysis in human cardiac myocytes revealed key action potential regulating miRNAs

To identify miRNAs contributing to the regulation of human cardiac AP, a quantitative analysis of the miRNA targetomes in human cardiac myocytes was performed. Cardiac myocytes derived from human induced pluripotent cells (hiPSC-CMs) served as an accessible model for human cardiac myocytes. hiPSCs from a healthy individual without any history of cardiovascular disease[240] were differentiated to beating hiPSC-CMs using a well-established cardiac differentiation protocol[255] with minor modifications (**Figure 4.1 A**).

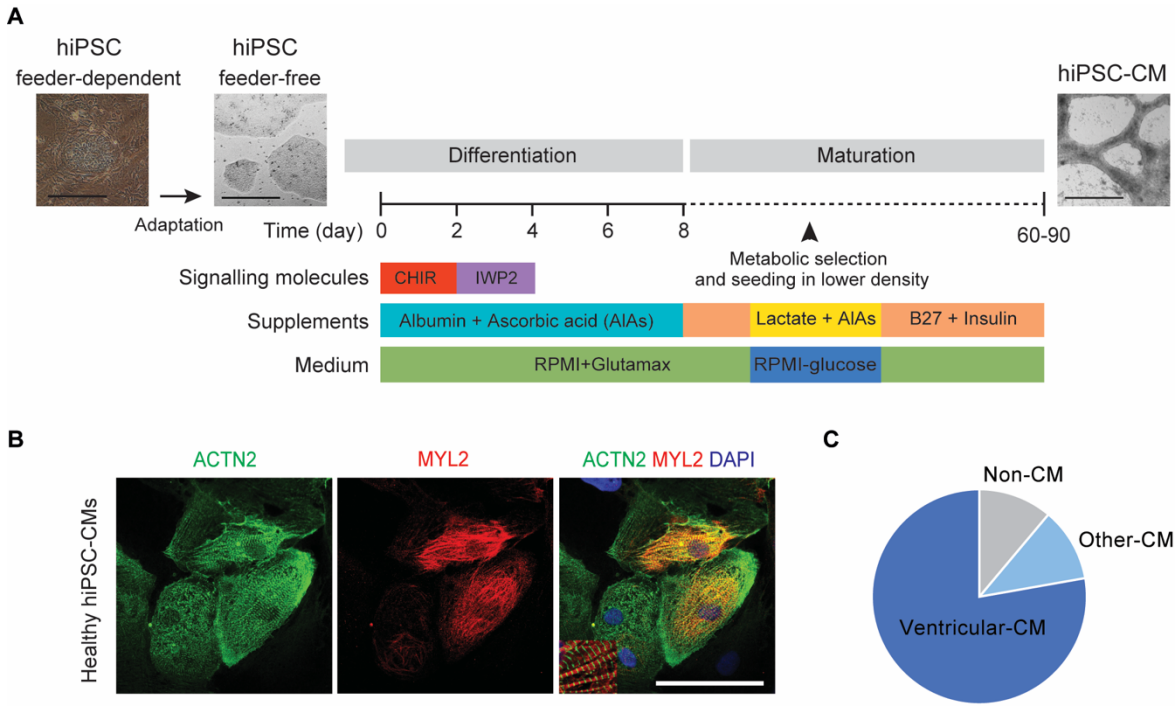

Figure 4.1. Directed cardiac myocyte differentiation from human iPSCs. (A) Protocol for adaptation of human iPS cells (left, hiPSC) from feeder-dependent culture to feeder-free setup, and cardiac differentiation based on manipulating Wnt-signaling, yielding hiPSC-derived cardiac myocytes (right, hiPSC-CMs, scale bars represent 500 µm). **(B)** Representative images showing immunofluorescent staining for actinin (alpha-actinin, ACTN2) and myosin (ventricular myosin light chain, MYL2) filaments in healthy hiPSC-CMs cultured for 60-90 days (scale bar depicts 25 µm). **(C)** The proportion of cardiac myocyte subtypes at Day 60 of differentiation. The ACTN2^{+} cells were defined as cardiac myocytes. Ventricular-like CMs expressed the ventricular marker MYL2 in addition to alpha-actinin (Data from 3 independent differentiations). This figure has been partially used in our publication[256].

Briefly, the hiPSCs were first adapted to a feeder-free culture system, were replated, and differentiation was initiated when the cells reached 80-90% of confluency. Activation and inhibition of Wnt-signaling were achieved using small molecules CHIR99021 and IWP2, respectively, inducing hiPSCs to differentiate toward cardiac progenitors. Prolonged culture (60 to 90 days) and a metabolic selection resulted in the relative maturation of hiPSC-CMs. Immunofluorescent staining in these cells against ACTN2 (sarcomeric Actinin Alpha 2), a general cardiac myocyte marker, and a ventricular specific marker, MYL2, revealed that this differentiation protocol resulted in a heterogeneous population (**Figure 4.1 B**), consisting of a majority of ventricular-like myocytes ($ACTN2^{+}MYL2^{+}$, 80%), a smaller population of non-ventricular myocytes ($ACTN2^{+}MYL2^{-}$, 11%) and another fraction lacking both markers ($ACTN2^{-}MYL2^{-}$, **Figure 4.1 C**).

To define the human cardiac myocyte-specific "channelome" and "miRNome", these hiPSC-CMs were then subjected to deep RNA sequencing and small RNA sequencing analysis (**Figure 4.2 A**). To this end, high-quality RNA (as measured by RNA Integrity number > 8, **Figure 4.2 B**) was extracted from healthy hiPSC-CMs, and total mRNA libraries (poly-adenylated, **Figure 4.2 C**) and small RNA libraries (**Figure 4.2 D**) were prepared, validated, and deep RNA-sequencing was performed. After subsequent analysis, these myocyte-specific data were supplemented with transcriptome and small RNA profiling data sets of human non-failing left ventricular myocardium (Yang et al., 2014, GEO accession: GSE46224).

The UniProt Knowledge-based database[258] was then used to extract a list of 27 proteins that are confidently annotated as ion channels involved in cardiac repolarization. Out of these 27 ion channels, the corresponding genes of 23 were expressed in cardiac myocytes based on the expression profiles of the human myocardium and hiPSC-CMs, comprising the human cardiac myocyte-specific "channelome" (**Figure 4.3**). To determine the "miRNome", the top 100 highly expressed miRNAs in human myocardium and hiPSC-CMs were considered in the downstream analysis, as the expression level of a miRNA in cells closely determines its functional relevance[85]. Next, TargetScan v7.2[113] was used for miRNA-target mining and identification of miRNAs with binding sites in the 3' UTR of cardiac myocyte-specific ion channel mRNAs. This analysis yielded 273 individual miRNAs with 1 to 8 conserved and canonical 7-mer or 8-mer binding sites in 3' UTR of the ion channel genes, with 46 seed families meeting the expression threshold (**Figure 4.3**). Amongst these top 46 cardiac ion channel-targeting miRNAs, miR-365 with eight binding sites exhibited the largest number of binding sites in the 3' UTR of the cardiac ion channel mRNAs, followed by miR-125 (with 7 binding sites) and miR-26 (with 6 binding sites). Interestingly, all the predicted direct targets of miR-365, namely *KCNQ1*, *KCNH2*, *KCNJ2*, *CACNA1C*, *KCNC3*, *KCNA1,* and *KCNJ3* (**Figure 4.4 A**), are contributing to the repolarization phases of cardiac AP (AP phases 1, 2, and 3) and

some are known to be the major ion channels forming repolarizing currents (e.g., KCNQ1 forming I_{Ks}, KCNH2 forming I_{Kr}, or KCNJ2 contributing to I_{K1}).

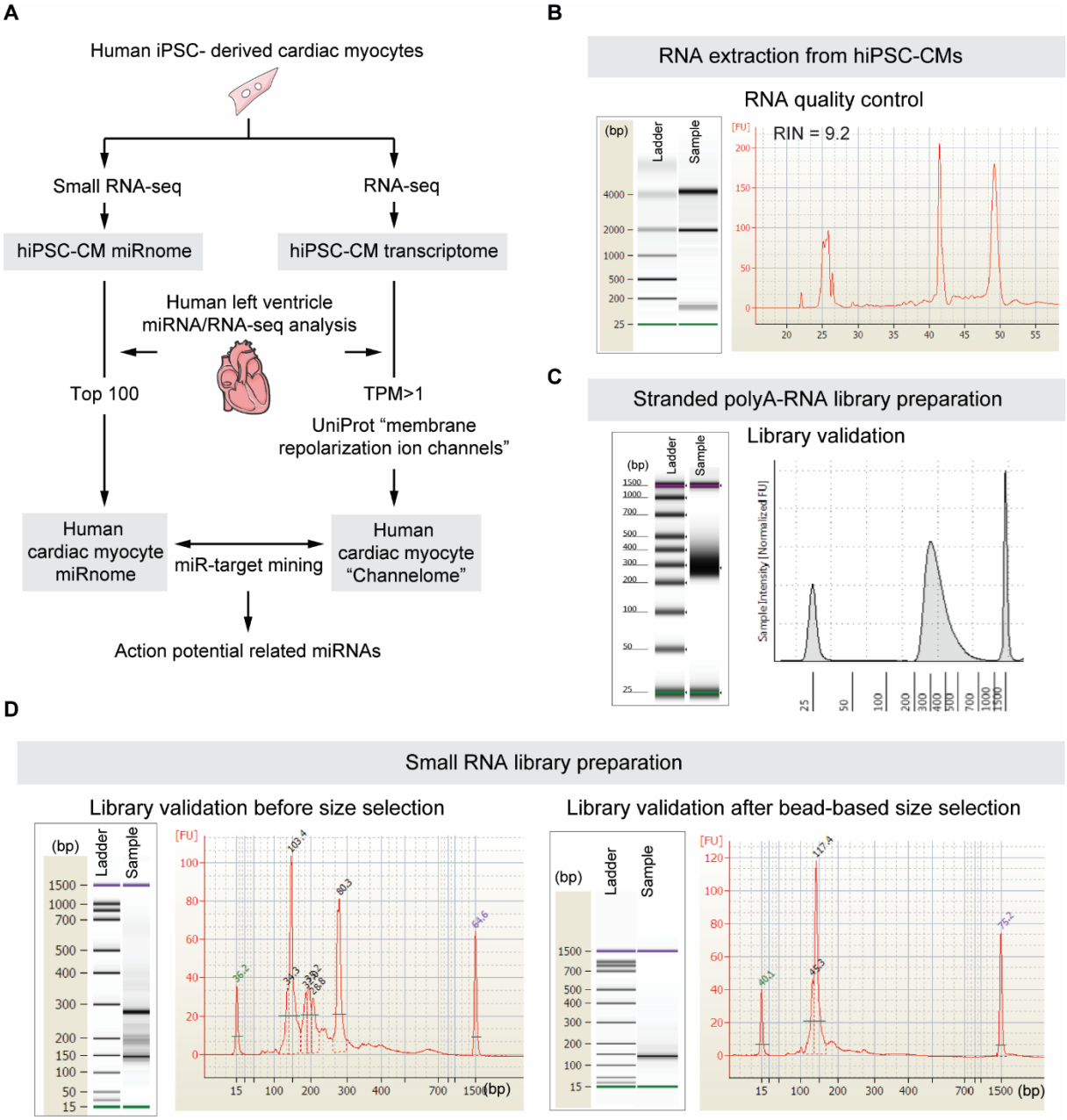

Figure 4.2. Quality control steps in preparation of small and poly-adenylated RNA sequencing libraries from healthy hiPSC-CMs. (A) Scheme representing the miRNA-targetome screening approach to identify miRNAs involved in cardiac repolarization. This panel has also been used in our publication[256]. **(B)** Representative gel image (left) and electropherogram (right) of total RNA sample extracted from a healthy hiPSC-CM sample (> 60 days in culture) after running Bioanalyzer RNA Pico. Samples with RNA integrity number (RIN) > 8 were selected for either small RNA or polyA-RNA library preparation. **(C)** Validation of a representative polyA-RNA library prepared from hiPSC-CMs, using TapeStation D1000. The resulting cDNA library contained 170-700 bp fragments (peak at 260 bp). **(D)** Representative images of cDNA library quality control during small RNA library preparation, using Bioanalyzer DNA1000. Libraries were first validated (left) for the presence of the miRNA band (143-146 bp). Subsequently, the smaller fragments were enriched using beads and the second validation (right) was performed post-purification.

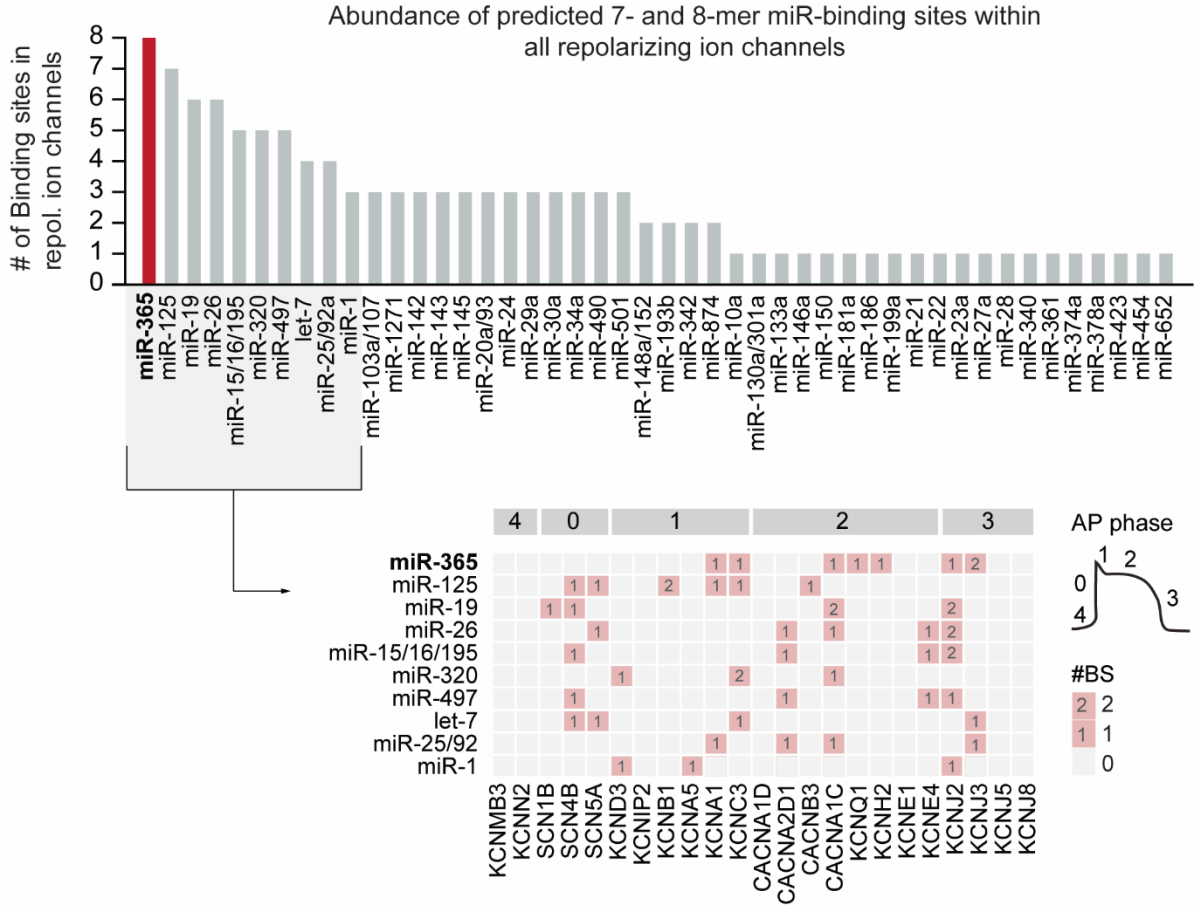

Figure 4.3. Screening of miRNA-targetomes to identify relevant miRNAs in the regulation of cardiac repolarization. The total number of predicted binding sites within 3' UTRs of mRNAs encoding for repolarizing ion channels among all miRNAs expressed in human myocardium. MiRNAs are ranked according to the respective number of binding sites (upper panel). The ion channel targets of the top 10 candidate miRNAs are depicted in detail (lower panel) and are assigned to the different phases of a typical ventricular AP. This figure has also been used in our publication[256].

This analysis indicated miR-365 as a potential candidate for regulation of cardiac repolarization through binding to the 3' UTR of the essential ion channel mRNAs and, therefore, repression of these genes. It is known that the repertoire of ion channels contributing to AP formation is highly specific in different species specificity. To determine if the expression of miR-365 also follows a species-specific pattern, the relative expression of miR-365 was assessed in various cardiac cells and models (**Figure 4.4 B**). The results revealed that the expression of miR-365 is about 5-fold higher in human cardiac myocytes (as measured in hiPSC-CMs and human left ventricular myocardium) compared to the myocardium of rodent models. MiR-365 expression was similar and somewhat higher in porcine models relative to humans.

Small RNA-sequencing in healthy hiPSC-CMs indicated moderate to high expression of miR-365 in these cells (415 read counts) with 3p arm as the dominant (mature) strand with higher reads and 5p as the transient (star) strand with only a few detected reads (**Figure 4.4 C**).

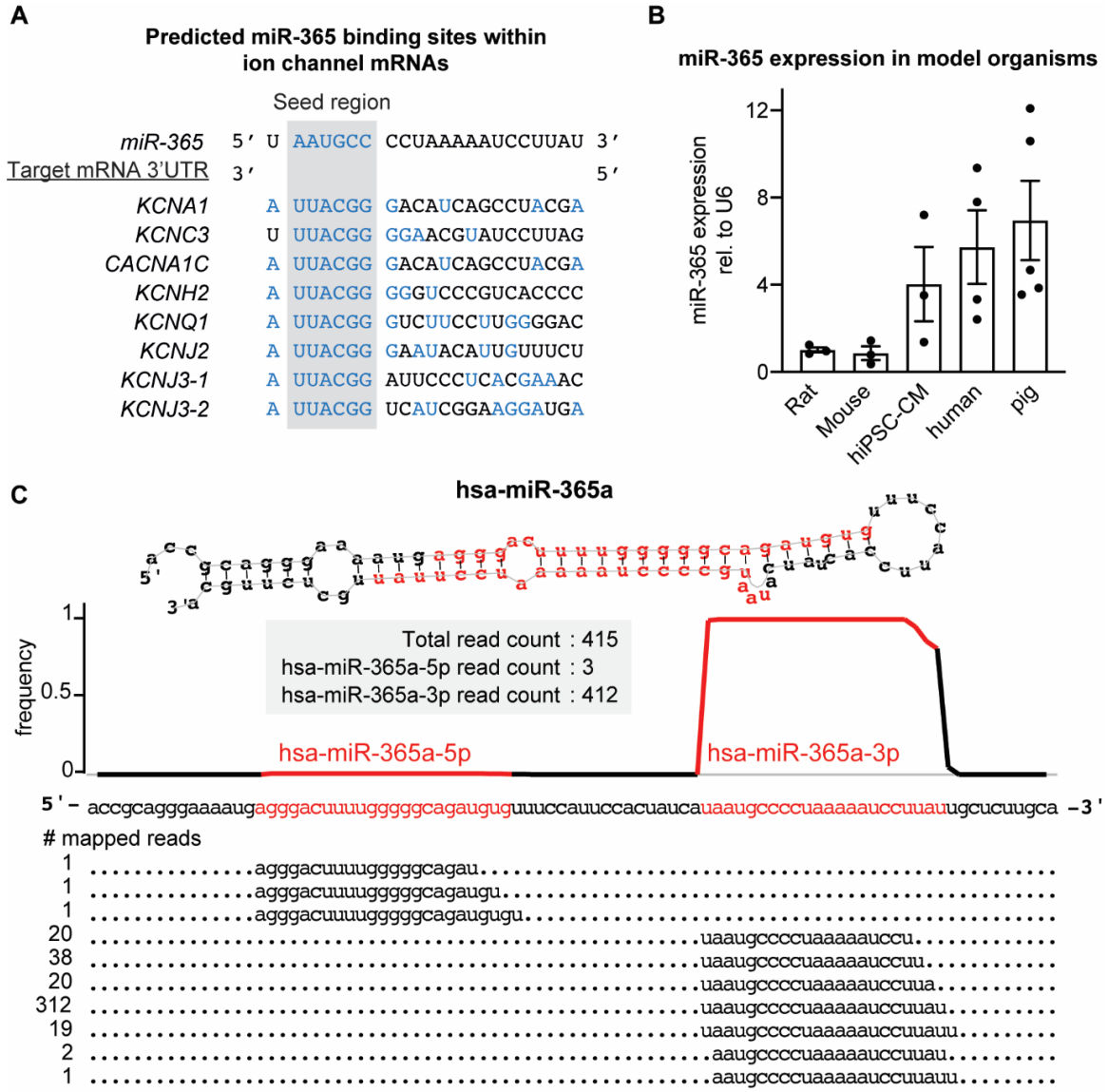

Figure 4.4. Characterization of miR-365 targeting and expression in model organisms. (A) The sequence of mature miR-365 (identical between hsa-miR-365a and hsa-miR-365b) and the corresponding 3' untranslated regions (3' UTR) of predicted target mRNAs. The seed region (nucleotides 2-7 of the mature miRNA from the 5' end) and the corresponding binding sites are highlighted in gray and the Watson-Crick base pairing between miRNA and 3' UTRs are depicted in blue. **(B)** Relative expression of miR-365 in various model organisms, namely neonatal rat cardiac myocytes, mouse left ventricular myocardium, human iPSC-derived cardiac myocytes, human left ventricular myocardium and porcine left ventricular myocardium, assessed by qPCR (n= 3-5 independent samples). Data are reported as means ± SEM. **(C)** Proposed stem-loop structure and read signature of hsa-miR-365a precursor based on miRDeep2 analysis on small RNA-sequencing data of hiPSC-CMs. The overall frequency of the small RNA-sequencing reads and the total number of mapped reads to each part of the miRNA sequence (3p arm or mature strand and 5p arm or star strand) are depicted in the lower panels. This figure has also been used in our publication[256].

4.1.2 The predicted targetome of miR-365 links this miRNA to arrhythmia

To assess the potential relevance of miR-365 in human disease, gene enrichment analysis was performed on predicted targets of this miRNA. Based on TargetScan (v7.2), 377 transcripts are predicted to contain conserved 7- or 8-mer binding sites for miR-365 (herein

conserved targets), while 2918 transcripts in total contain 7- or 8-mer binding sites calculated based on probability of targeting and irrespective of evolutionary conservation. Enrichment analysis on either of these lists primarily associated miR-365 to long QT syndrome (LQTS) among all genetic diseases in humans (listed in OMIM database), suggesting a potential role of miR-365 in controlling arrhythmogenesis (**Figure 4.5 A and B**).

The outcome of the gene list enrichment analysis on the predicted targets of miR-365 is detailed in **Table 4.1**, where the miR-365 target genes contributing to each disease are listed. For instance, among 12 genes that are known to be associated with LQTS, 8 genes are predicted to be targets of miR-365, meaning that miR-365 targets comprise 67% of all the genes that are known to cause LQTS.

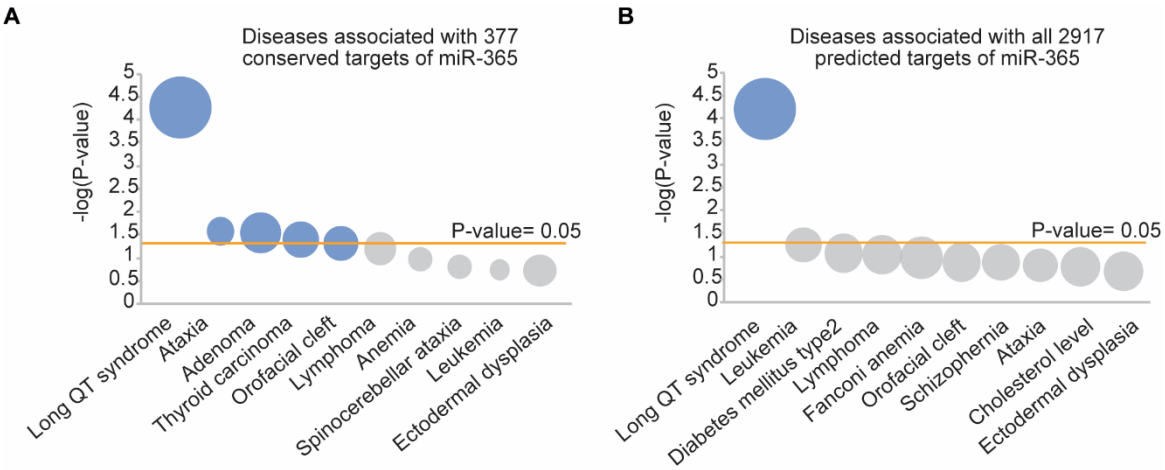

Figure 4.5. The predicted targetome of miR-365 links this miRNA to cardiac arrhythmia. Bubble plots depicting the outcome of gene list enrichment analysis to evaluate the association between either the conserved targets **(A)** or all the predicted targets **(B)** of miR-365 and all hereditary human diseases (listed in OMIM database). Bubble size corresponds to the number of genes associated with a disease term and the p-value on the y-axis (calculated using the Fisher exact test) depicts the significance of the phenotypes. P-value < 0.05 was considered as significant. A modified version of panel B has been used in our publication[256].

Disease	Disease contributing target genes	Disease contributing target genes		P-value
		proportion	number	
associated with 377 conserved targets of miR-365				
Long QT syndrome	***KCNH2, KCNQ1, CACNA1C, KCNJ2***	**33%**	**4/12**	**5.46E-05**
Ataxia	*ABCB7, ATXN7, KCNC3, KCNA1*	7%	4/60	0.03
Adenoma	*PLAG1, HMGA2*	14%	2/14	0.03
Thyroid carcinoma	*PTEN, TRIM24*	12%	2/17	0.04
Orofacial cleft	*UBB, SATB2*	11%	2/19	0.05
Lymphoma	*BCL2, MALT1*	9%	2/22	0.06
Anemia	*DHFR, FANCD2, ABCB7*	5%	3/61	0.11
Spinocerebellar ataxia	*ATXN7, KCNC3*	5%	2/37	0.15
Leukemia	*CBFB, BCL2, WHSC1L1*	4%	3/78	0.18
Ectodermal dysplasia	*IKBKG*	9%	1/11	0.19
associated with all 2917 predicted targets of miR-365				
Long QT syndrome	***KCNH2, KCNE1, KCNQ1, CACNA1C, SCN5A, ALG10, SCN4B, KCNJ2***	**67%**	**8/12**	**5.8E-05**
Leukemia	*PDGFRB, CHIC2, ARHGEF12, CBFB, ACSL6, PTPN11, DEK, ARHGAP26, LPP, TCL1B, KIT, BCL2, ABL2, BAX, TCF3, JAK2, WHSC1L1*	22%	17/78	0.05
Diabetes mellitus, type 2	*SLC30A8, KCNJ11, IRS1, HNF4A, AKT2, ENPP1, IRS2, SLC2A4*	25%	8/32	0.08
Lymphoma	*TCL1B, CASP10, IL21R, BCL2, PAX5, MALT1*	27%	6/22	0.09
Fanconi anemia	*BRIP1, FANCM, FANCD2, FANCE*	31%	4/13	0.11
Orofacial cleft	*UBB, SATB2, MTHFR, MTR, TP63*	26%	5/19	0.13
Schizophrenia	*APOL4, DAO, CHRNA7, AKT1, MTHFR, NRG1, DISC1*	23%	7/30	0.14
Ataxia	*SETX, TBP, FGF14, ABCB7, ATXN7, KCNC3, KCNA1, ITPR1, SLC1A3, APTX, POLG, TTBK2*	20%	12/60	0.16
Cholesterol level	*CETP, PCSK9, HMGCR, PLTP*	27%	4/15	0.16
Ectodermal dysplasia	*EDAR, IKBKG, TP63*	27%	3/11	0.21

Table 4.1 Disease association analysis of the predicted targets of miR-365.

4.2 MiR-365 determines the action potential duration in cardiac myocytes by repressing repolarizing ion channels

4.2.1 MiR-365 prolongs action potential duration in cardiac myocytes

To assess the impact of miR-365 on cardiac AP, first the robust manipulation of this miRNA in cardiac myocytes was established. To this end, an adeno-associated virus (AAV)-based miRNA overexpressing vector (AAV6-miR-365) was cloned, and neonatal rat cardiac myocytes (NRCMs, **Figure 4.6 A**) and hiPSC-CMs (**Figure 4.6 B**) were infected with increasing concentrations of this AAV (Multiplicity of infections e^3 to $5e^5$ viral genomes/cell). The cellular levels of miR-365 were subsequently evaluated at different time points post-infection. In both cell types, MOI of e5 vg/cell 5 days after infection resulted in an optimal elevation of miR-365

levels (a 12- and 22-fold increase in NRCMs and hiPSC-CMs, respectively, compared to cells treated with AAV6-ctrl) as determined by qRT-PCR.

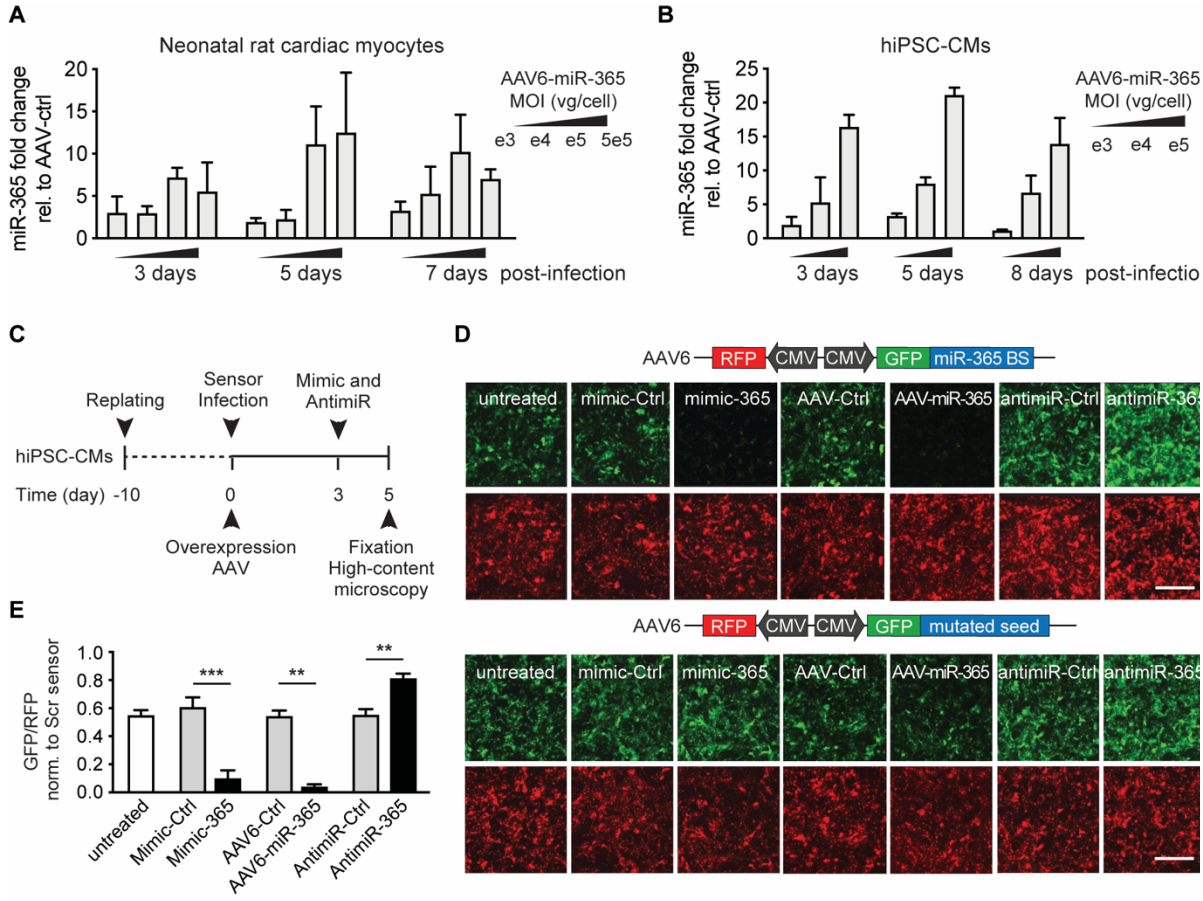

Figure 4.6. Validation of *in vitro* manipulation of miR-365 in cardiac myocytes. (A) Relative expression of miR-365 in neonatal rat cardiac myocytes after infection with AAV6-miR-365. The cells were infected with different amounts of AAV6-miR-365 -ctrl (MOI e3, e4, e5, and 5e5 viral genomes per cell) and incubated for different time intervals (3, 5, or 7 days) before RNA extraction and qPCR. The level of miR-365 is determined relative to U6. Data are represented as fold change compared to AAV6-ctrl at each condition and are acquired from 2 independent experiments. **(B)** MiR-365 expression fold change hiPSC-CMs infected with AAV6-miR-365 compared to AAV6-ctrl. AAV6-miR-365 or -ctrl were added in different MOIs (e3, e4, e5 vg/cell), and after incubation for 3, 5, or 7 days, RNA extraction and qPCR were performed. The expression of miR-365 is determined relative to U6, and data are acquired from 2 independent experiments. **(C)** Experimental scheme for assessing the efficiency of various miR-365 manipulation strategies in hiPSC-CMs using a dual-fluorescent reporter assay. **(D)** Dual fluorescent sensor for miR-365 activity in living hiPSC-CMs. Representative images of hiPSC-CMs after infection with AAV6 expressing miR-365 activity sensor (or a control sensor with a mutated binding site) and subsequent manipulation of miR-365. Manipulation was performed using overexpressing AAV infection or transfection with mimic or antimiR oligonucleotides. High content microscopy was used to determine the activity of miR-365 (scale bar= 100 µm). **(E)** Quantification of data from (D). Data are from 3-4 independent experiments performed in duplicates. Unpaired t-test was used to determine the statistical significance (* $P < 0.05$, ** $P < 0.01$). All quantitative data are reported as means ± SEM. This figure has been partially used in our publication[256].

Higher concentrations of viruses resulted in more inter-sample variability, which can indicate levels of cytotoxicity. Additionally, adverse effects on cell morphology were observed upon prolonged cultivation of NRCMs with viruses. Thus, the experiments were continued with MOI of e^5 vg/cell and incubation for 5 days. Alternatively, cells were transfected with synthetic

mimics and locked nucleic acid inhibitor oligonucleotides (LNA-antimiRs) for 48 hours. Since qPCR is not a reliable method to determine the miRNA levels after treatment with oligonucleotides [259], a miRNA activity sensor was employed for this purpose (**Figure 4.6 C**). These constructs express RFP and GFP under the control of identical but independent promoters, with RFP serving as an internal control, while GFP is followed by three complementary binding sites for miR-365 or a scrambled sequence as a control for binding specificity. Thus, the expression of GFP is quantitatively repressed by the intracellular activity of the miRNA. An AAV serotype 6 vector (AAV6) was used to express this construct robustly in hiPSC-CMs (**Figure 4.6 D**) and the GFP/RFP ratio was assessed by high content microscopy after treating the cells with 25-50 nM of synthetic mimic- or antimiR-365. Mimic-365 transfection resulted in about 70% of GFP repression, while antimiR-365-treated cells exhibited about 30% of GFP de-repression. Dual fluorescent reporter assay in cells treated with AAV6-miR-365 substantiated the qPCR results, showing 85% of GFP repression (**Figure 4.6 E**). This regulation through the miR-365 binding site was specific and was not observed using a sensor with a scrambled binding site.

To determine the impact of miR-365 on AP duration (APD), optical AP recordings were performed in cardiac myocytes. To do this, a genetically encoded fluorescence resonance energy transfer (FRET)-based voltage sensor was used. The sensor, which consists of a voltage-sensitive domain (VSFP) followed by a pair of fluorescent proteins Clover-GFP and mRuby2-RFP (CR) [218,260], was cloned into an AAV6 backbone. In a polarized membrane, conformational change in VSFP results in the energy transfer between the FRET pairs (**Figure 4.7 A and B**). This can be observed upon the ratiometric recording of the two emission wavelengths upon excitation at 488 nm, as a decrease in 565 nm and an increase in 615 nm fluorescent intensities. Since the membrane is depolarized throughout phases 0 to 3 of the AP (equivalent to repolarization time), the width of AP traces resulting from these measurements represents APD of ventricular CMs with a high signal-to-noise ratio (**Figure 4.7 C**).

To achieve highly specific AP recordings from ventricular myocytes, the MYL2 promoter was used upstream of the sensor. Using this construct, the changes in APD were measured in NRCMs treated with AAV6-miR-365 or AAV6-Ctrl (**Figure 4.7 D**). APD at 90% of repolarization (APD90) was significantly prolonged from a mean of 496 ms in the AAV6-Ctrl group up to 702 ms in AAV6-miR-365 treated cells (41% increase). A comparable increase was observed in APD50 (299 ms to 391 ms upon AAV6-miR-365 infection).

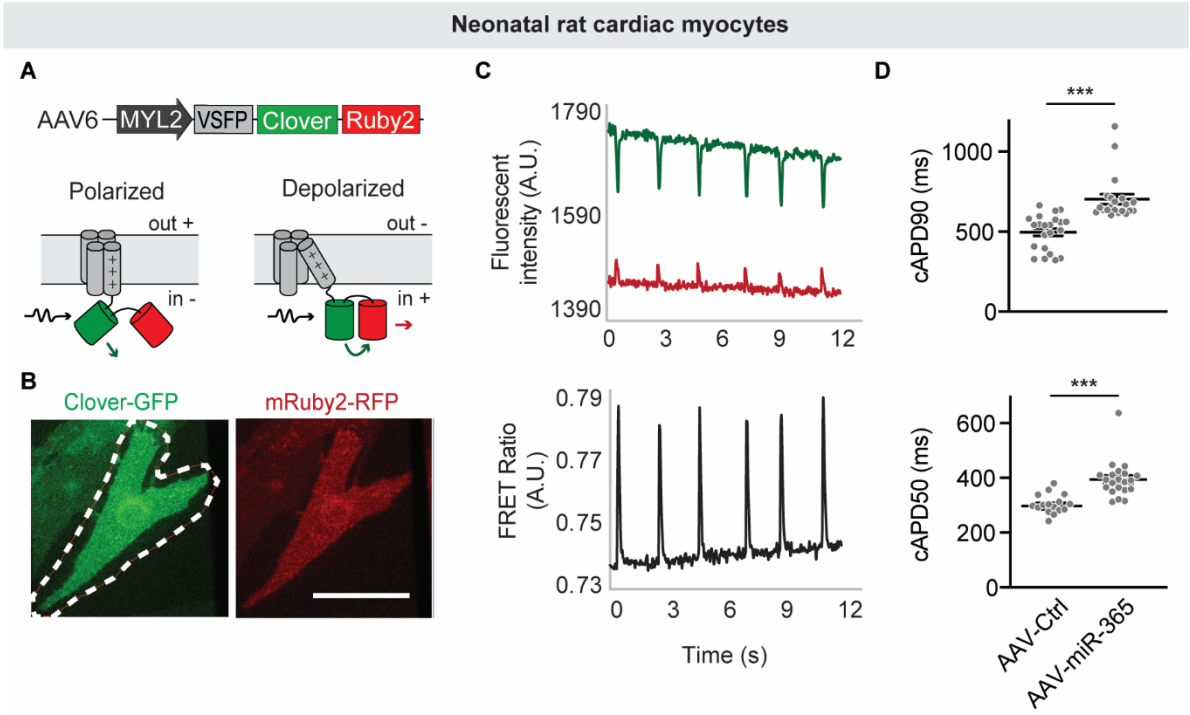

Figure 4.7. Optical action potential measurements in neonatal rat myocytes upon overexpression of miR-365. (A) Schematic representation of AAV6 vector carrying the voltage sensor VSFP-CR under control of MYL2 ventricular myocyte specific promoter. The sensor consists of a voltage-sensitive domain (VSFP) conjugated to a FRET pair, namely Clover-GFP and mRuby2-RFP (CR). The lower panel depicts the conformational change upon membrane depolarization. This panel has also been used in our publication[256]. **(B)** Representative image of NRCMs infected with AAV6-MYL2-VSFP-CR after 5 days in the red and green channel of a FRET-microscope. The region of interest (ROI) is depicted as a white dotted line around a single cell (scale-bar 25 µm). **(C)** Representative plot of GFP and RFP intensities during FRET recording (upper panel). The ratio of RFP/GFP represents the energy transfer during the repolarization phase of the AP. **(D)** Quantitative analysis of the ratiometric determination of AP duration. Data are acquired from 16-22 cells per condition from 3 independent experiments. Data were recorded in MetaFluor software and analyzed in a custom-written Python program yielding corrected AP duration at 90% or 50% of repolarization (cAPD90 and cAPD50). Bazett's formula was used for correcting the variation caused by beating frequency. A two-tailed Mann-Whitney test was performed to determine the statistical significance of the mimic-365 effect on APD (*** P-value < 0.001).

Although a significant effect of miR-365 on APD was observed in these experiments, the cells were exposed to double the amount of AAVs (for expressing VSFP-CR and miR-365), and this resulted in an adverse effect in the quality of the cells, presented as 40-46% prolongation of APD even in AAV6-ctrl treated cells compared to untreated ones (data are not shown). Thus, in measurements performed in hiPSC-CMs, synthetic mimics were used instead of overexpressing AAVs to avoid any possible cytotoxicity (**Figure 4.8 A**). In hiPSC-CMs, sufficient expression of VSFP-CR was achieved in ventricular cells 8-15 days post-infection (**Figure 4.8 B**). Voltage sensing and signal-to-noise ratio were robust and comparable to NRCMs (**Figure 4.8 C and D**) and augmentation of miR-365 in hiPSC-CMs similarly prolonged the APD in these cells, as shown by 28% prolongation of corrected APD90 (cAPD90) from 295 ms in the control group compared to 377 ms in mimic-365 treated ventricular-like myocytes (**Figure 4.8 E and F**).

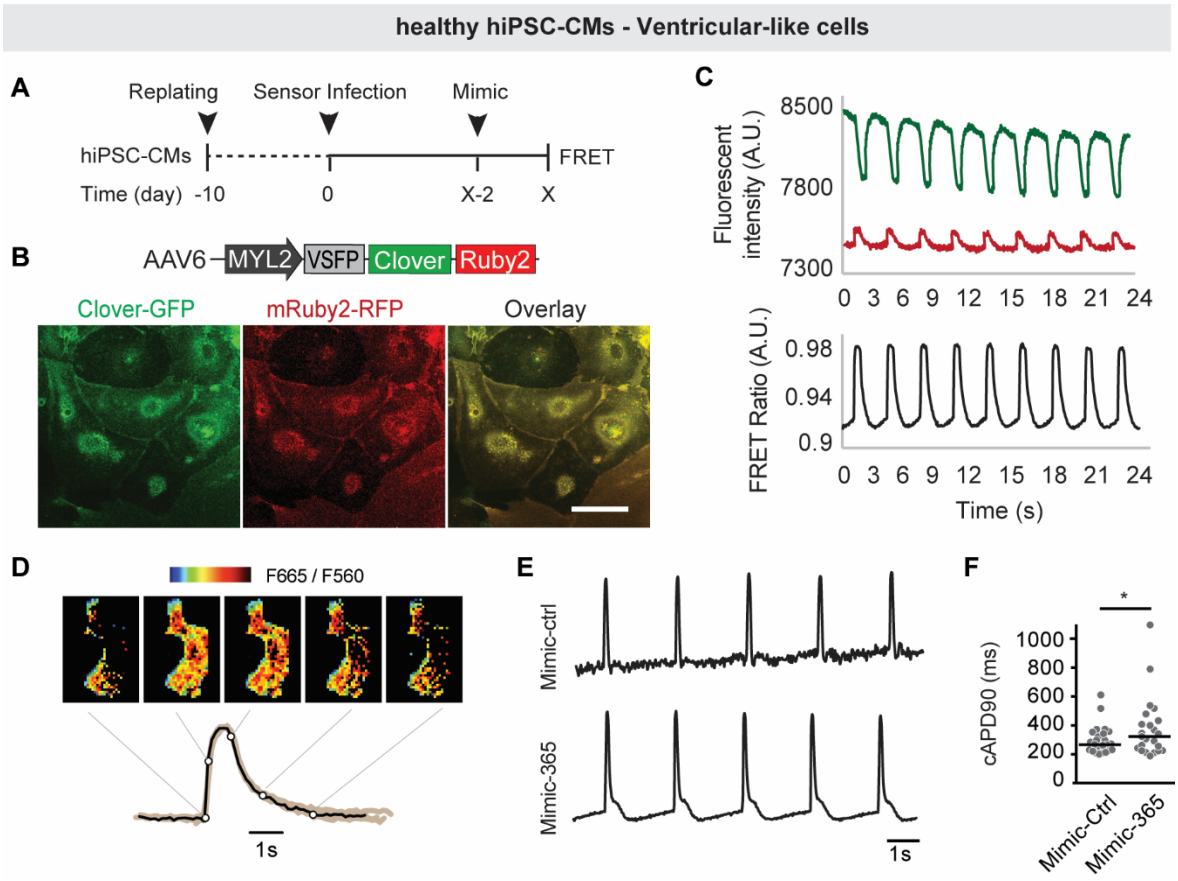

Figure 4.8. FRET-based action potential recording in miR-365 treated human ventricular-like myocytes. (A) Experimental scheme for FRET-based AP recording in hiPSC-CMs. After robust expression of GFP and RFP upon infection of cells with AAV6 carrying the voltage sensor, the cells were transfected with mimic-365 or mimic-ctrl. 48 hours after transfection, the optical recording of the spontaneous AP was performed at 35 °C. **(B)** Representative confocal image of hiPSC-CMs infected with AAV6-MYL2-VSFP-CR (scale-bar 25 µm). **(C)** Representative RFP and GFP (upper panel) and AP traces (F665/F560 ratio, lower panel) from healthy hiPSC-CMs. **(D)** Real-time voltage-dependent change in energy transfer and therefore in FRET ratio during a ventricular AP depicted as an average trace of 15 APs recorded from a representative cell transduced with AAV6-MYL2-VSFP-CR. Energy transfer between the two fluorophores is depicted as the ratio of Ruby2-RFP to Clover-GFP emissions (F665/F560) in specific time-points of the AP (white circles). This panel has also been used in our publication[256]. **(E)** Comparative AP traces of hiPSC-CMs treated with mimic-365 or -ctrl. **(F)** Quantitative analysis of transmembrane potentials. Data are acquired from 23-26 cells per condition from 3 independent experiments and are depicted as Bazett's corrected AP duration at 90% of repolarization (cAPD90). A one-tailed unpaired t-test was performed on log-transformed values to determine the statistical significance of the mimic-365 effect on APD (median 295 ms in the control group compared to 377 ms in the mimic-365 group, * P-value < 0.05).

These measurements were complemented with optical recordings using the voltage-sensitive dye, di-8-ANEPPS, as a well-established methodology that minimizes any additional intervention to the cells rather than miRNA manipulation, as the cells are loaded with the dye shortly before measurements (**Figure 4.9 A and B**). ANEPPS-based measurements also enable high signal-to-noise ratio determination of APD (**Figure 4.9 C**); however, ventricular-myocytes cannot be distinguished from the other cardiac cells, and the recorded AP would be a mixture of ventricular and non-ventricular APs. Nevertheless, using this methodology, the observed prolonging effect of miR-365 on cardiac myocytes APD was substantiated, with a

35% significant prolongation upon miR-365 elevation (**Figure 4.9 D and E**, median APD increased from 379 ms in the control group up to 509 ms in the mimic-365 group).

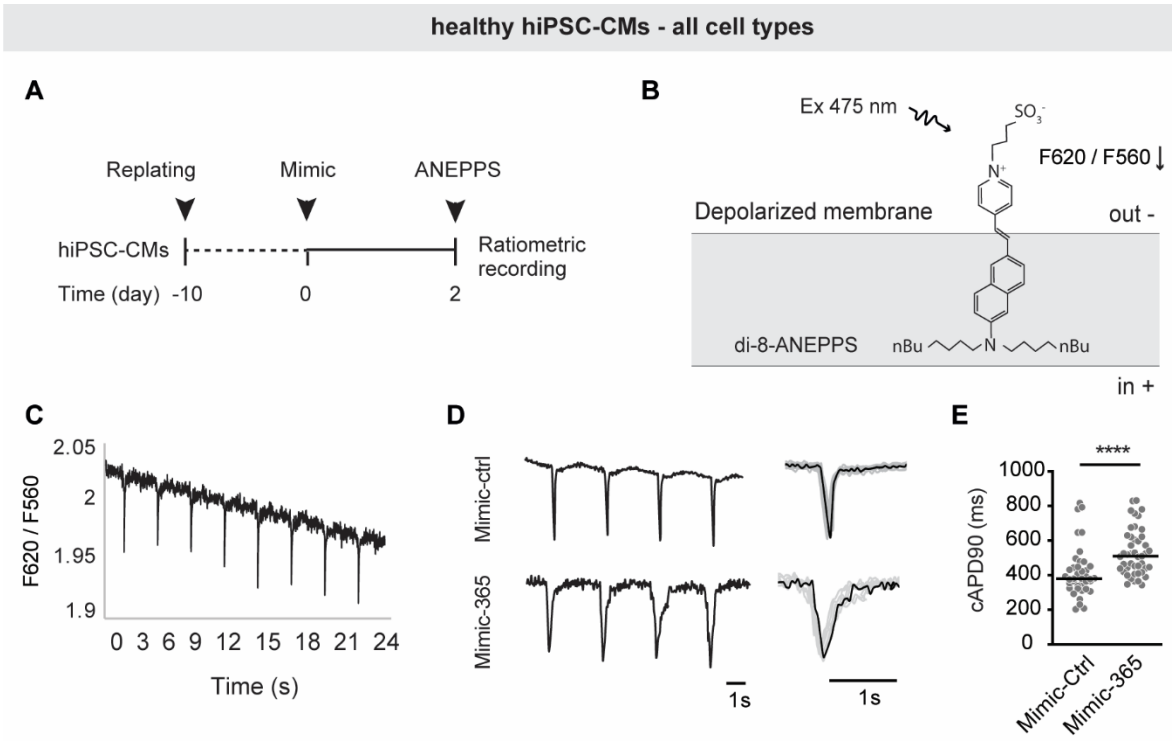

Figure 4.9. Optical action potential recording in hiPSC-CMs reveals a prolonging effect of miR-365 on action potential duration. (A) Experimental scheme depicting optical recording of the AP in hiPSC-CMs using a voltage-sensitive dye (di-8-ANEPPS). **(B)** Scheme showing localization of the voltage-sensitive dye di-8-ANEPPS in the cell membrane and its fluorescence response to electric potential changes during the cardiac AP. **(C)** Decrease in F620/F560 upon membrane depolarization during optical measurement of AP in hiPSC-CMs. The ratio represents the spontaneous AP of the cells in real-time. **(D)** Representative AP traces from healthy hiPSC-CMs transfected with mimic-365 or control mimic and loaded with di-8-ANEPPS 48 hours after transfection (left). Averaged trace of multiple APs recorded from a representative cell in each condition (right). **(E)** Quantitative analysis of transmembrane potentials (median 379 ms in the mimic-Ctrl group compared to 509 ms in the mimic-365 group). Data are acquired from 39-45 cells per condition from 5 independent experiments. All measurements were performed at 35 °C. Data are represented as Bazett's formula corrected APD at 90% of repolarization (cAPD90). The Man-Whitney test was performed to determine the statistical significance of the mimic-365 effect on APD (**** P-value < 0.0001). This figure has been partially used in our publication[256].

Taken together, data obtained from rat and human cardiac myocytes demonstrate the functional role of miR-365 in the prolongation of APD.

4.2.2 MiR-365 regulates action potential duration through shaping a distinct transcriptome signature

To delineate the mechanism through which miR-365 exerts its prolonging effect on cardiac AP, the targetome of this miRNA was next characterized. qRT-PCR for predicted ion channel targets of miR-365 upon transfection of NRCMs with mimic-365 showed significant repression of targets mRNA levels (**Figure 4.10 A**).

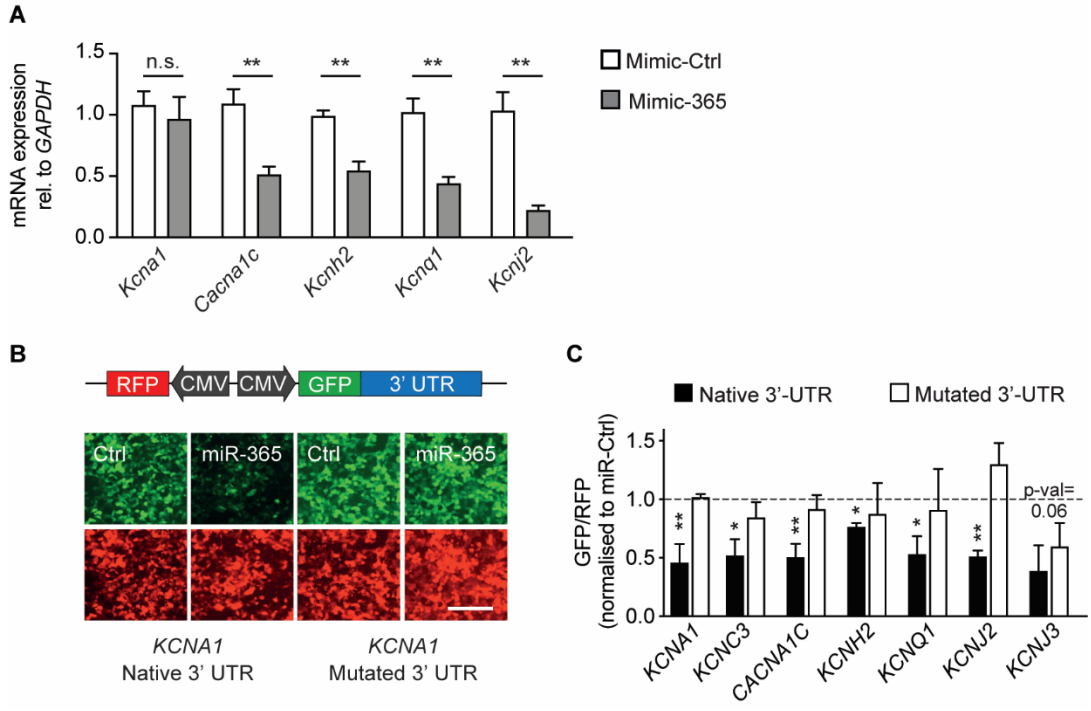

Figure 4.10. MiR-365 regulates the key repolarizing ion channels in ventricular myocytes. **(A)** Quantitative real-time PCR to assess repression of a panel of predicted targets upon elevation of miR-365. The experiment was performed in neonatal rat cardiac myocytes transfected with mimic-365 or mimic-ctrl (n= 2-4 independent experiments). Unpaired t-test was used to determine the P-value (** P-value < 0.01, n.s., non-significant). **(B)** Dual fluorescent reporter assay to test for direct interaction between miR-365 and its predicted ion channel targets in HEK293 cells. The reporter constructs carried 3' UTR sequences of target genes with native or mutated binding sites for miR-365. Representative images of cells transfected with a reporter for binding to the KCNA1-3' UTR and its respective mutated binding site (scale bars= 10 µm). **(C)** Quantitative analysis of the reporter assay. Data is from 3-6 independent experiments, each performed in triplicate. Two-tailed unpaired t-test or Mann-Whitney test were used to determine the P-values (* P < 0.05, ** P < 0.01). All quantitative data are reported as means ± SEM. This figure has also been used in our publication[256].

To validate the direct interaction between miR-365 and the 3' UTR of the predicted ion channel targets, double-fluorescent (df-) reporter assays were carried out in HEK293 cells. These were similar df-reporter constructs (mentioned in section 4.2.1), in which the GFP mRNA sequence was followed by the native 3' UTR of the target gene or a seed mutated 3' UTR as control (instead of repetitive miR-365 binding sites, **Figure 4.10 B**). Fluorescent intensities were then assessed at the single-cell level, and a decrease in the GFP/RFP ratio indicated miRNA binding and repression of the specific target 3' UTR. Using a synthetic miR-365 mimic or a control mimic, miR-365 was found to interact with and therefore significantly repress the predicted conserved ion channel 3' UTR. The GFP/RFP ratio was unchanged in the cells treated with mutated constructs, showing the specificity of miRNA-binding site interaction (**Figure 4.10 C**).

To evaluate the global effect of miR-365 on the transcriptome of human cardiac myocytes, deep RNA sequencing of healthy hiPSC-CMs was then performed upon manipulation of miR-365 levels using mimics or antimiRs (**Figure 4.11 A**).

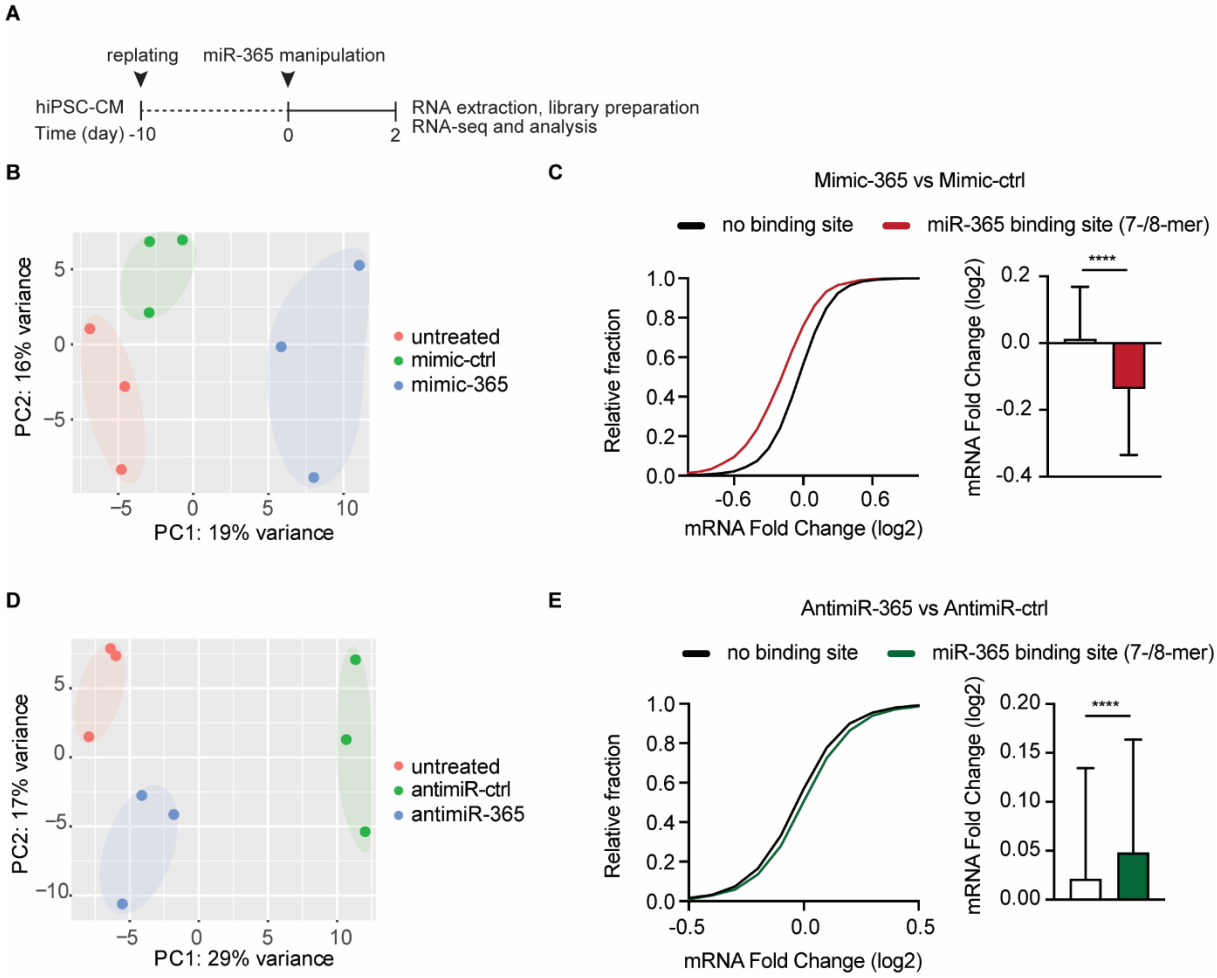

Figure 4.11. The effects of miR-365 manipulation on the transcriptome of hiPSC-CMs. (A) Experimental scheme for RNA-seq experiment in healthy hiPSC-CMs. The cells were replated, equilibrated for more than 10 days, and transfected with mimic-365 or -Ctrl and antimir-365 or -Ctrl. RNA was extracted after 48 hours, and libraries were prepared, sequenced, and analyzed. **(B)** Principal component analysis (PCA) of untreated, mimic-ctrl- and mimic-365- treated hiPSC-CMs. Each dot represents a sample (n=3 per condition). **(C)** Cumulative distribution plots of differential expression for all genes versus broadly conserved miR-365 targets containing 8-mer, 7-mer-m8, or 7-mer-A1 binding sites as predicted by TargetScan Human version 7.2. Kolmogorov-Smirnov test was used to determine the significance (****P-value < 0.0001). Quantitative data are reported as median with interquartile range. **(D)** Principal component analysis of untreated, antimiR-ctrl- and antimiR-365- treated hiPSC-CMs. **(E)** Cumulative distribution plots of expression changes for all genes versus broadly conserved miR-365 targets carrying 8-mer, 7-mer-m8, or 7-mer-A1 binding sites (predicted by TargetScan Human version 7.2). Data are shown as median mRNA fold change with interquartile range, and the Kolmogorov-Smirnov test was used to determine the significance (**** P-value < 0.0001). This figure has also been used in our publication[256].

Each treatment exerted a distinct effect on the transcriptome of hiPSC-CMs, and the replicates clustered closer to each other than samples with other treatments as calculated by principal component analysis (PCA, **Figure 4.11 B and D**). To assess whether these transcriptome changes are indeed related to the modulation of miR-365 activity, the mRNA fold changes were determined for all miR-365 targets (mRNAs predicted to contain 7- or 8-mer binding sites for miR-365) and was compared to those of all other non-target genes. Cumulative distribution of mRNA fold changes upon transfection of mimic-365 demonstrated significant and strong

repression of mRNAs carrying miR-365 binding sites (predicted targets) compared to mRNAs without miR-365 binding sites (non-targets, **Figure 4.11 C**). A significant de-repression was observed upon antimiR-365 transfection compared to the antimiR-ctrl treated group (**Figure 4.11 D**).

Out of more than 16000 expressed transcripts in hiPSC-CMs (transcripts per million reads, TPM > 1), 645 genes were significantly downregulated in cells treated with mimic-365 compared to mimic-ctrl. Out of these, 253 genes were reciprocally elevated in antimir-365 treated hiPSC-CMs (**Figure 4.12 A**). These reciprocally regulated genes were used for a gene ontology (GO) enrichment analysis using ClueGO[241,242], to determine the biological processes that were primarily affected by miR-365 deregulation. Among all biological processes known in humans, processes contributing to the repolarization phase of cardiac AP were enriched (**Figure 4.12 B**). Specifically, K^+ ion transport machinery and its regulatory elements are shown to be highly downregulated by miR-365. The gene set enrichment analysis (GSEA) was then utilized to assess whether the expression pattern of each gene set is sufficient to explain the observed differences caused by mimic-365 manipulation. GSEA showed a significantly negative normalized enrichment score (NES, false discovery rate FDR < 0.05) not only for "voltage-gated potassium channel activity" (**Figure 4.12 C**) but also "regulation of cardiac muscle cell AP" (**Figure 4.12 D**), suggesting a synergistic effect of miR-365 on AP duration which extends beyond targeting of repolarizing ion channels, to affecting regulators of AP formation and repolarization.

These experiments were performed on the bulk population of hiPSC-CMs; however, the available cardiac differentiation protocols yield a heterogenous population of myocytes. To delineate the impact of miR-365 manipulation in different populations of hiPSC-CMs, these cells were subjected to single-cell RNA-sequencing (scRNA-seq) upon transfection with mimic- or antimiR-365 (**Figure 4.13 A**).

scRNA-seq of both mimic- and antimiR-365-treated samples resulted in comparable quality of data, as indicated by various metrics such as the number of detected genes and mitochondrial gene expression (**Figure 4.13 B, C and Table 4.2**). Thus, after the quality control steps, the two datasets were combined into one Uniform Manifold Approximation and Projection (UMAP) embedding and dimensionality reduction step was applied on the data. In this step, only the highly variable genes belonging to the top 15 principal components were used (**Figure 4.13 D**), since these components are sufficient to significantly explain the differences between the cell type clusters. Subsequently, unsupervised clustering was performed on these 6000 cells, revealing various hiPSC-CM subpopulations, irrespective of miR-365 manipulation (**Figure 4.13 E and G**).

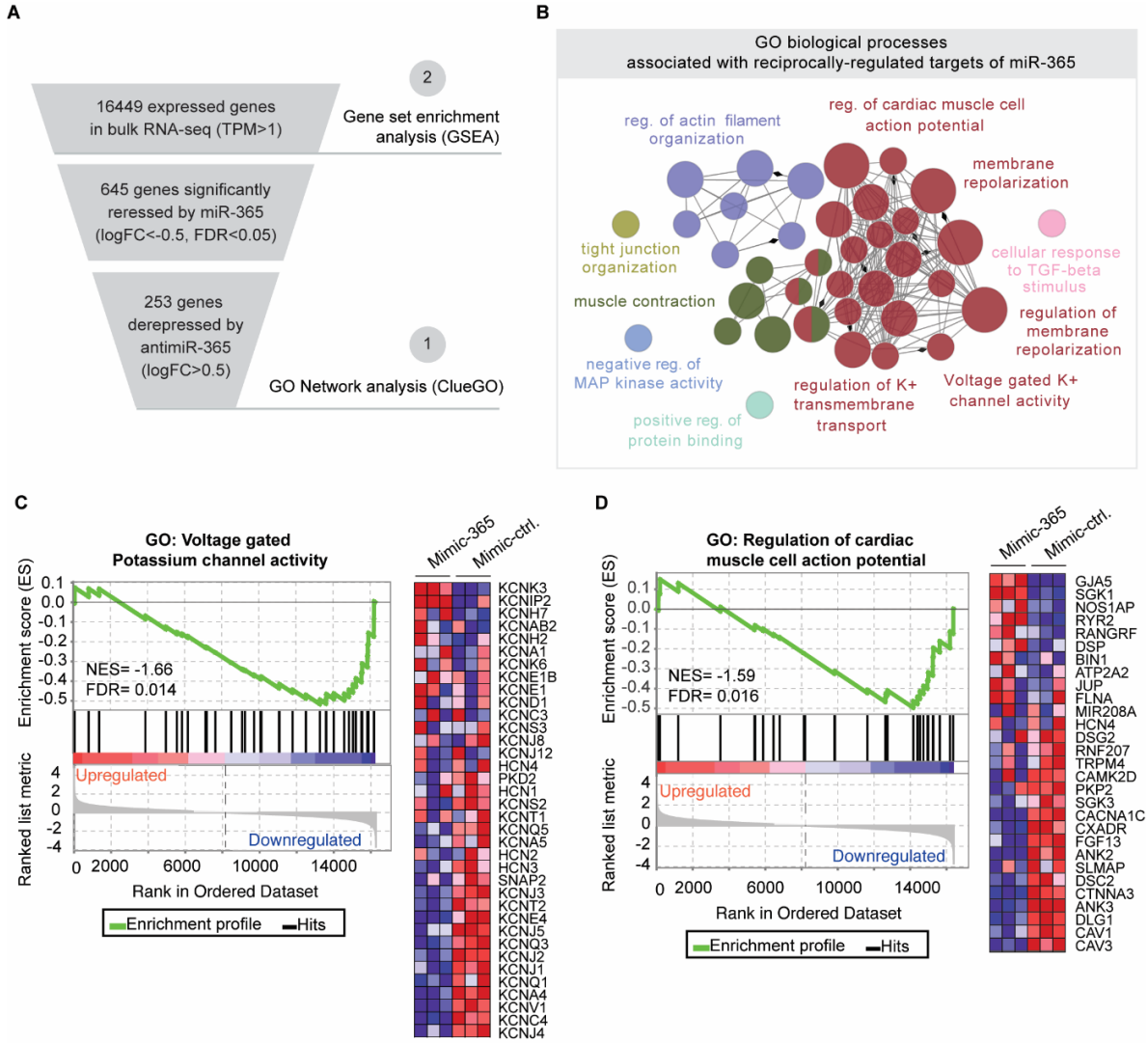

Figure 4.12. miR-365 represses repolarization and action potential regulators in human cardiac myocytes. (A) Scheme representing the steps to filter the genes expressed above the noise level and to shortlist the differentially expressed genes for downstream analysis. **(B)** The gene ontology network of biological processes that are significantly associated with miR-365 target genes. Each network node (circle) represents a specific biological process or pathway, and network edges (lines) show the relationship between different terms. The size of the circles represents the term enrichment significance (P-value <0.05). Functionally similar terms or pathways are depicted with the same color. **(C, D)** Gene set enrichment analysis (GSEA) on the GO terms voltage-gated potassium channel activity (C) and regulation of cardiac muscle cell AP (D). The whole transcriptome of hiPSC-CMs was ranked based on gene expression fold-changes between mimic-365 and mimic-Ctrl and normalized enrichment scores (NES) were calculated to determine whether each term is negatively or positively enriched upon miR-365 elevation. A false discovery rate (FDR) <0.05 is considered as significant enrichment. Genes contributing to each GO term are shown in the heatmaps (blue-red depicts low-high expression). This figure has also been used in our publication[256].

Since current hiPSC-CM differentiation protocols (such as the one used here) typically yield a population that represents properties of fetal myocytes, the available transcriptomic profiling maps of embryonic cardiogenesis[261,262] were used to characterize the subpopulations observed in the scRNA-seq dataset. All the cells expressed the general cardiac markers such as various types of Troponin and Myosin genes at different levels. The majority of cells showed high levels of *MYL2* as well as expression of ventricular myocyte-specific genes such as *HEY2*

and *CACNAC1C*. At the lower resolution (0.1), these cells comprised about 90% of the whole population and were classified as ventricular-like cardiac myocytes. About 8% of the population represented an exclusive expression of *GJA1, GJA5, NR2F2, BMP4, SYTL2,* and *SLN* and were categorized as atrial-like hiPSC-CMs. Another population of myocytes (about 2%) expressed a number of markers genes found in Outflow-tract (OFT)-like myocytes (*BMP2, TBX3, LTBP2, PRSS23, TIMP2, GLI3, PCSK6, ID2*, *ADM,* and *ITM2A*) (**Figure 4.13 F**). To have a better insight into the composition of myocytes, the resolution of unsupervised clustering was increased to 0.3 (maximum resolution resulting in distinct populations) and the expression of cell type-specific markers at this resolution was determined (**Figure 4.13 G, H**). Interestingly, while atrial- and OFT-like cardiac myocyte populations remained unchanged, further clustering was observed within the ventricular-like hiPSC-CMs. Cluster 0 represented a higher expression of mitochondrial genes compared to the other ventricular populations, which indicates a higher metabolism in these cells. Clusters 1 and 3 expressed hallmarks of cardiac hypertrophy (e.g., *NPPA* and *NPPB* in cluster 1 and components of the Wnt/β-catenin signaling pathway such as *CTNNB1*) at relatively higher levels. Cluster 2 expressed *TNNI3* higher than the other cells. This particular isoform of Troponin is more abundant in adult cardiac myocytes [263], indicating that cluster 2 is comprised of more mature hiPSC-CMs. Whereas cluster 5 expressed *CCR7*, *CACNA1D*, and *ACTA1*, markers of multipotent cardiac progenitors and intermediate cardiac myocytes, indicating that these cells are at more primitive stages of maturation. In order to focus on ventricular-specific effects of miR-365 manipulation, we continued with the simplified clustering, where all the ventricular-like cells are grouped in one cluster irrespective of their physiological state (**Figure 4.13 E**).

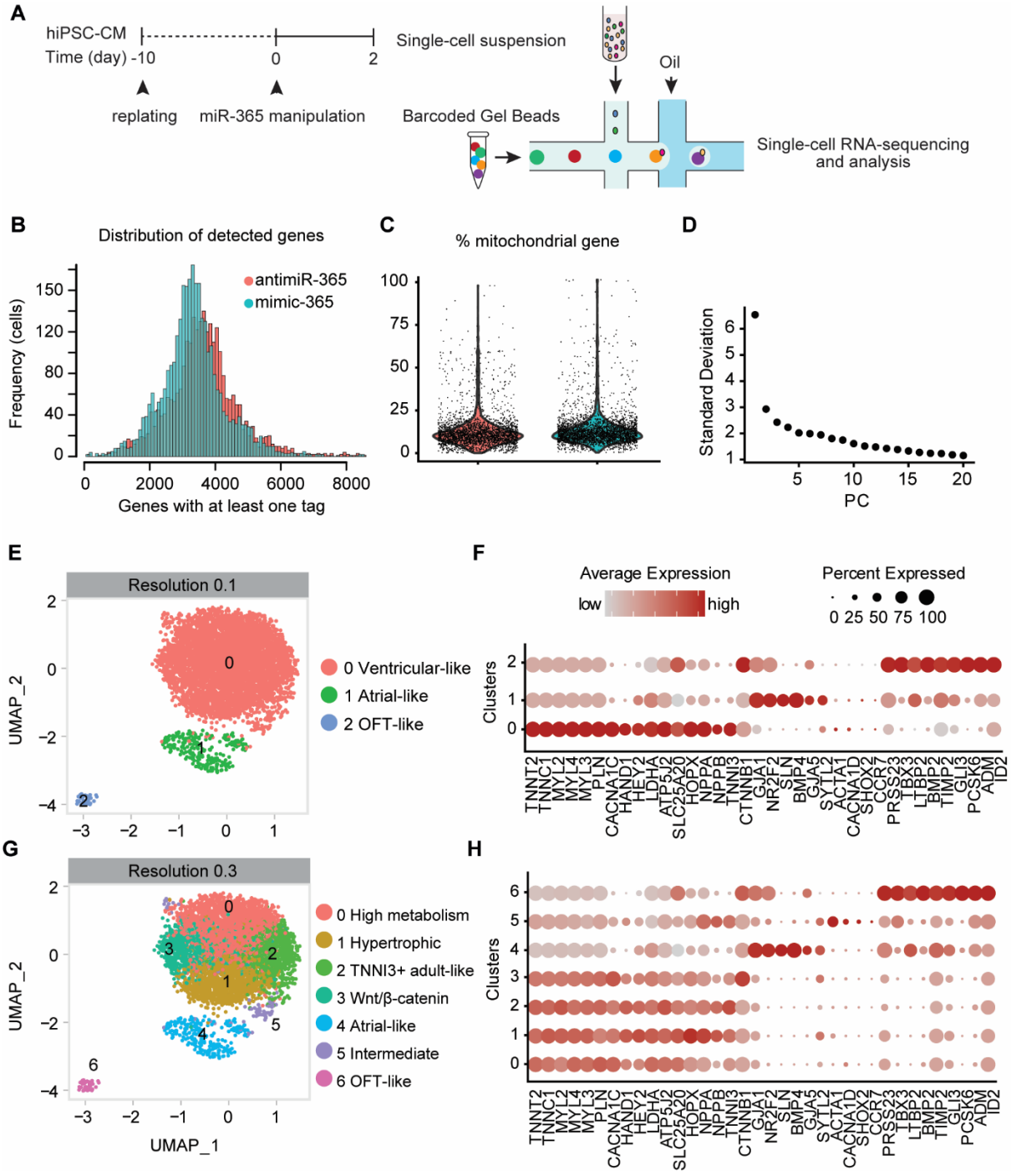

Figure 4.13. Single cell RNA sequencing of healthy hiPSC-CMs after miR-365 manipulation.

(A) Scheme depicting the experimental setup for single-cell RNA-sequencing of hiPSC-CMs after 48 hours of transfection with mimic- or antimir-365. **(B)** Histograms showing the frequency of detected genes per cell in each sample. Peaks (median detected genes) are observed at 3600 and 3400 for antimir and mimic samples, respectively. **(C)** Violin plots depicting the percentage of mitochondrial genes among all detected genes in each sample. **(D)** An elbow plot representing the ranking of principal components based on the percentage of variance explained by each one. Components 1 to 15 were used in the subsequent dimensional reduction step. **(E)** UMAP clustering of 6000 transcriptomes at resolution 0.1 revealed three main populations of cells. **(F)** Dot plot showing the average expression of marker genes defining different subpopulations of hiPSC-CMs. The size of dots indicates the proportion of cells in each cluster that express each marker gene. **(G)** UMAP clustering at a higher resolution (0.3) yields 7 subpopulations of cardiac myocytes, namely ventricular-like hiPSC-CMs at different stages of maturation (clusters 0-3 and 5). **(H)** Dot plot showing the average expression of marker genes in each subpopulation of hiPSC-CMs. This figure has been partially used in our publication[256].

	Mimic-365 treated hiPSC-CMs	AntimiR-365 treated hiPSC-CMs
Cells and detected genes		
Estimated Number of Cells	3,255	2,724
Fraction Reads in Cells	87.20%	85.50%
Mean Reads per Cell	114,416	133,849
Median Genes per Cell	3,437	3,610
Total Genes Detected	25,774	25,932
Median UMI Counts per Cell	15,527	16,853
Number of Reads	372,425,335	364,606,792
Valid Barcodes	97.70%	97.80%
Sequencing Saturation	68.40%	70.60%
Mapping		
Reads Mapped to Genome	87.70%	86.30%
Reads Mapped Confidently to Genome	83.50%	82.60%
Reads Mapped Confidently to Intergenic Regions	3.40%	3.00%
Reads Mapped Confidently to Intronic Regions	18.30%	18.00%
Reads Mapped Confidently to Exonic Regions	61.80%	61.50%
Reads Mapped Confidently to Transcriptome	57.20%	57.30%
Reads Mapped Antisense to Gene	0.90%	0.90%

Table 4.2. Single cell RNA-sequencing data quality metrics for hiPSC-CMs treated with antimiR- or mimic-365. This table has also been used in our publication[256].

ScRNA-seq datasets typically suffer from dropout events, which is defined as inefficient mRNA capture during library preparation and, therefore, artificial low or zero expression values for the gene[264]. This phenomenon especially affects genes with low to moderate expression levels, such as ion channel genes in our hiPSC-CMs datasets. To circumvent this problem, an imputation algorithm, namely Adaptively-thresholded Low-Rank Approximation (ALRA), was applied. This algorithm estimates the true expression of genes based on their overall expression pattern in different cell types (clusters). This approach drastically improved the homogeneity of gene expression as depicted for representative genes at moderate (e.g., *KCNH2, CACNA1C*) to low (e.g., *GJA5, KCNA1*) expression range compared to normalized values without imputation (**Figure 4.14**). Thus, the imputed values were adapted for downstream differential gene expression analysis between mimic- and antimiR-365 treated groups (**Figure 4.15 A and B**). The changes in the expression of ion channel targets of miR-365 in ventricular hiPSC-CMs were in line with the targetome identified in previous experiments. These findings further validated that the major repolarizing ion channels, specifically *KCNQ1*, *KCNC3*, *KCNJ3*, and *KCNJ2* are targeted by miR-365, and therefore, the elevation of this miRNA prolongs APD through repression of these ion channels.

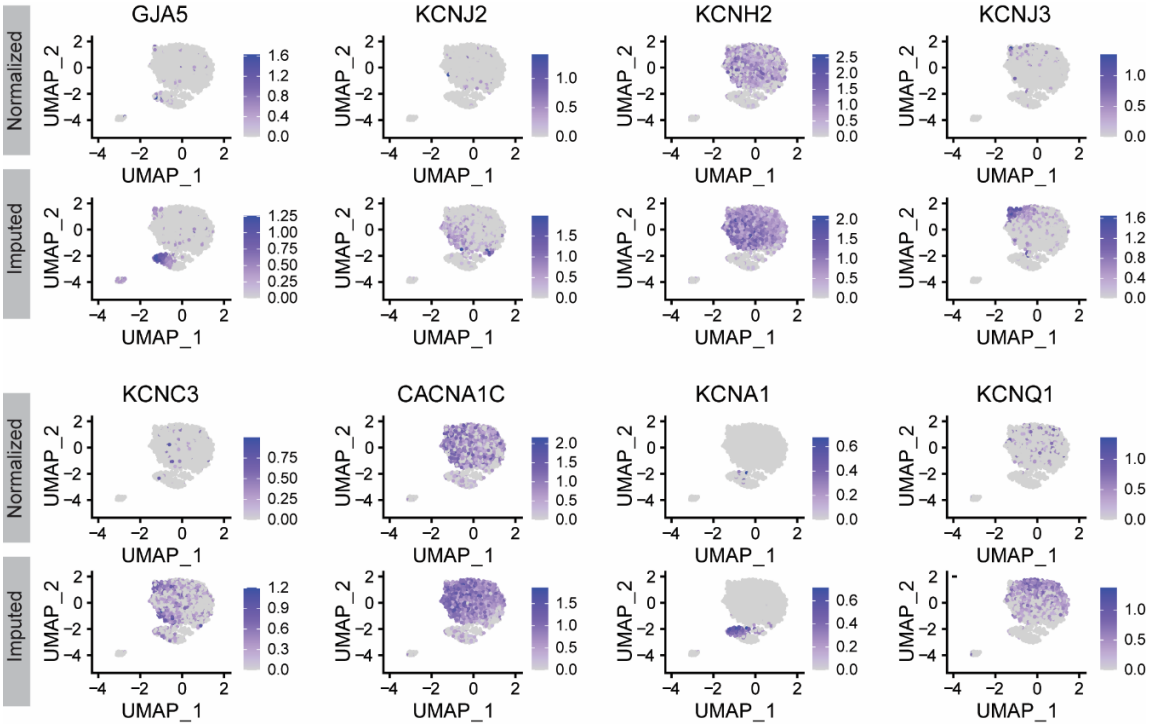

Figure 4.14. Imputation of single-cell RNA-sequencing data resolves the dropout and recovers true expression levels. Feature plots comparing gene expression patterns before and after imputation algorithm. A panel of genes at moderate (e.g., *KCNH2, CACNA1C*) to low (e.g., *GJA5, KCNA1*) expression range were chosen, and feature plots were generated based on original average expression and imputed expression values.

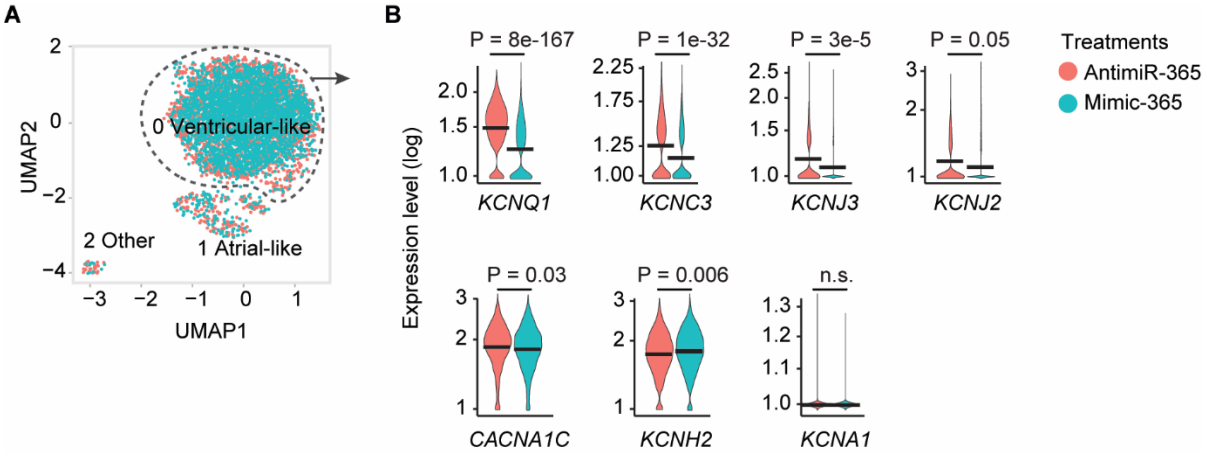

Figure 4.15. Differential expression of miR-365 predicted target ion channel genes within various cardiac myocyte populations. (A) UMAP embedding and clustering of hiPSC-CM treated with mimic- or antimiR-365 to assess for potential changes in cell populations. **(B)** Violin plots depicting the regulation of miR-365 predicted targets upon miR-365 manipulation at single-cell level in the ventricular populations of hiPSC-CM. Simplified clustering at resolution 0.1 was used to assess the cell-type specific effects of miR-365 manipulation.

4.3 MiR-365 as a means to normalize aberrant action potential duration in hiPSC-CM models of QT syndromes

Based on the above findings, the hypothesize was tested that miR-365 could be used as a means to therapeutically correct pathologically altered APD, such as in human QT syndromes. To evaluate this, patient-specific hiPSC-CMs derived from long QT syndrome type 1 (LQT1) and short QT syndrome type 1 (SQT1) patients were employed. The APD recorded from these patient-derived cardiac myocytes closely recapitulates the altered QT interval measured by electrocardiography in the donor patients [221,265]. Therefore, these cells provide a suitable model to test the effect of miR-365 manipulation on APD.

4.3.1 Elevation of miR-365 prolongs action potential duration in Short QT syndrome type 1

To obtain cardiac myocytes from SQT1 hiPSCs with comparable quality as the healthy cells, the cardiac differentiation protocol depicted in **Figure 4.1 A**, was optimized to include a shorter incubation time with the Wnt-activator CHIR at a higher concentration (6 µM, at days 0 to 1) following by a delayed inhibition of this signaling pathway (at day 3 instead of day 2). This protocol resulted in a majority of ventricular-like cardiac myocytes as identified by immunofluorescent staining for cardiac markers (**Figure 4.16 A**).

Optical recordings using either the voltage-sensitive dye di-8-ANEPPS (**Figure 4.16 B**) in bulk cardiac myocytes or using AAV6-MYL2-VSFP-CR (**Figure 4.16 E**) for exclusive recording from ventricular-like cells initially confirmed pathological shortening of APD in SQT1 cells compared to control myocytes (median cAPD90 in untreated SQT1 hiPSC-CMs were 263 ms and 191 ms in bulk population and ventricular cells, respectively, compared to 491 ms and 311 ms in healthy hiPSC-CMs). Based on previous experiments in healthy hiPSC-CMs and NRCMs, where higher levels of miR-365 repressed and therefore prolonged cardiac repolarization, SQT1 hiPSC-CMs were treated with mimic-365. This treatment prolonged the pathologically shortened APD by about 46% to 431 ms upon APD recording using di-8-ANEPPS (**Figure 4.16 C and D**). FRET-based ventricular-specific measurements, likewise demonstrated normalization of shortened APD upon overexpression of miR-365, resulting in about 50% increase in APD (**Figure 4.16 F and G**).

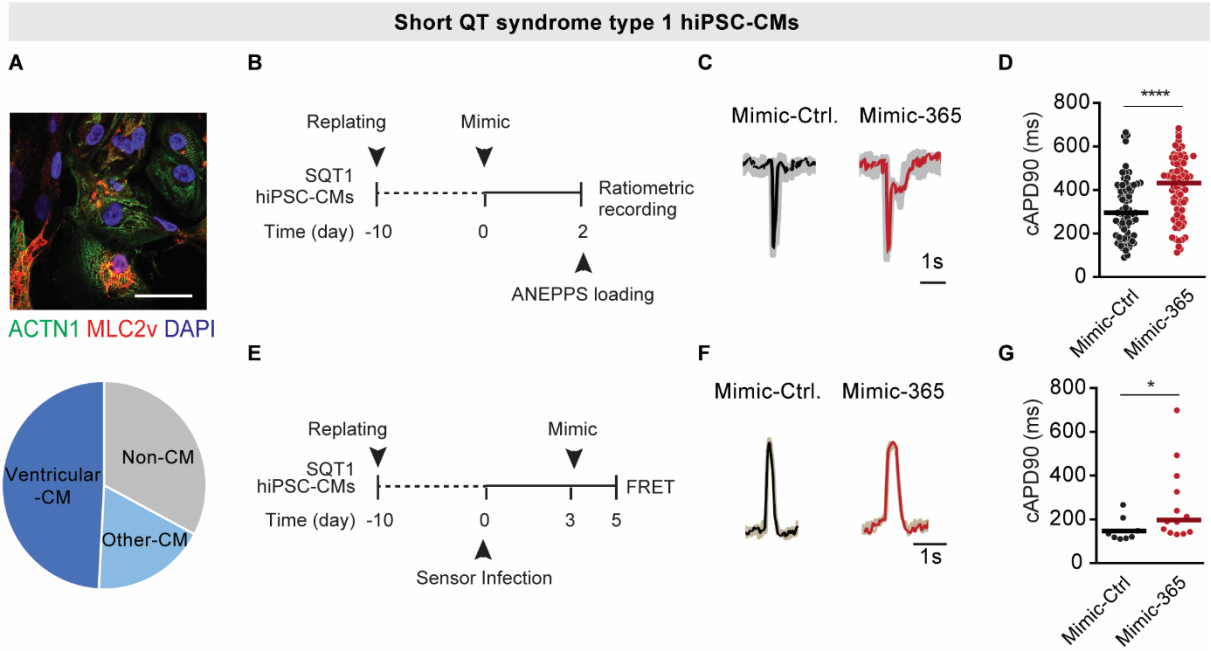

Figure 4.16. Elevation of miR-365 to prolong AP duration in Short QT syndrome type 1 (SQT1) hiPSC-CMs. (A) Representative image of SQT1 hiPSC-CMs (> 60 days) stained for cell type markers ACTN2 and MYL2 (upper panel). The pie chart (lower panel) shows the proportion of myocytes (blue) and non-myocyte (grey) populations. Ventricular-like (dark blue) myocytes are positive for ACTN2 and MYL2, ACTN2-positive cells negative for MYL2 are classified as other myocytes (light blue) (Data from 2 independent differentiation, scale bar = 20µm). **(B)** Experimental scheme for optical AP recording in SQT1 hiPSC-CMs after transfection with mimic-365 or -ctrl. **(C)** F665/F560 traces from representative SQT1 hiPSC-CMs treated with mimic-ctrl (black) and mimic-365 (red). Shown are the averages from 10-15 recorded APs per cell. **(D)** Quantification of optical AP recordings in all cardiac myocytes using di-8-ANEPPS. Note that APD is pathologically shortened in control-treated SQT1 hiPSC-CMs (median 290 ms compared to 431 ms in the mimic-365 group, from 72-74 cells per condition from 3 independent experiments). The two-tailed unpaired t-test was used to assess whether the change was significant (**** P-value < 0.0001). **(E)** Experimental scheme representing FRET-based AP recording in SQT1 hiPSC-CMs. **(F)** Averaged AP traces (10-15 single APs) recorded from representative SQT1 hiPSC-CMs treated with mimic-ctrl (black) and mimic-365 (red). **(G)** Quantification of optical AP recordings selectively in ventricular-like myocytes using MYL2-VSFP-CR (median 127 ms in the control group compared to 190 ms in mimic-365 treated cells). Data were acquired from 8-13 cells per condition from 2 independent experiments. (* P-value < 0.05 calculated by Mann-Whitney test). This figure has been partially used in our publication[256].

4.3.2 Inhibition of miR-365 normalizes prolonged action potential in Long QT syndrome type 1

In LQT1 hiPSC, directed cardiac differentiation was carried out using an identical protocol as the healthy cells in order to obtain beating hiPSC-CMs expressing cardiac markers (**Figure 4.17 A**). These cells were subjected to APD recordings using di-8-ANEPPS and AAV6-MYL2-VSFP-CR (**Figure 4.17 B and E**, respectively). Based on the hypothesis that the intracellular level of miR-365 and its ion channel targets would determine the target repression and APD, LQT1 hiPSC-CMs were transfected with a synthetic, locked nucleic acid inhibitor oligonucleotide (LNA-antimiR-365) or a scrambled oligonucleotide as a negative control (antimiR-Ctrl). Interestingly, optical APD measurements using di-8-ANEPPS showed a 60%

reduction of cAPD90 upon antimiR-365 transfection (**Figure 4.17 C and D**). FRET-based recordings exclusively in the ventricular population likewise demonstrated a 60% shortening and thus normalization of the abnormally prolonged APD (median 673 ms) to comparably normal levels (median 419 ms, **Figure 4.17 F and G**).

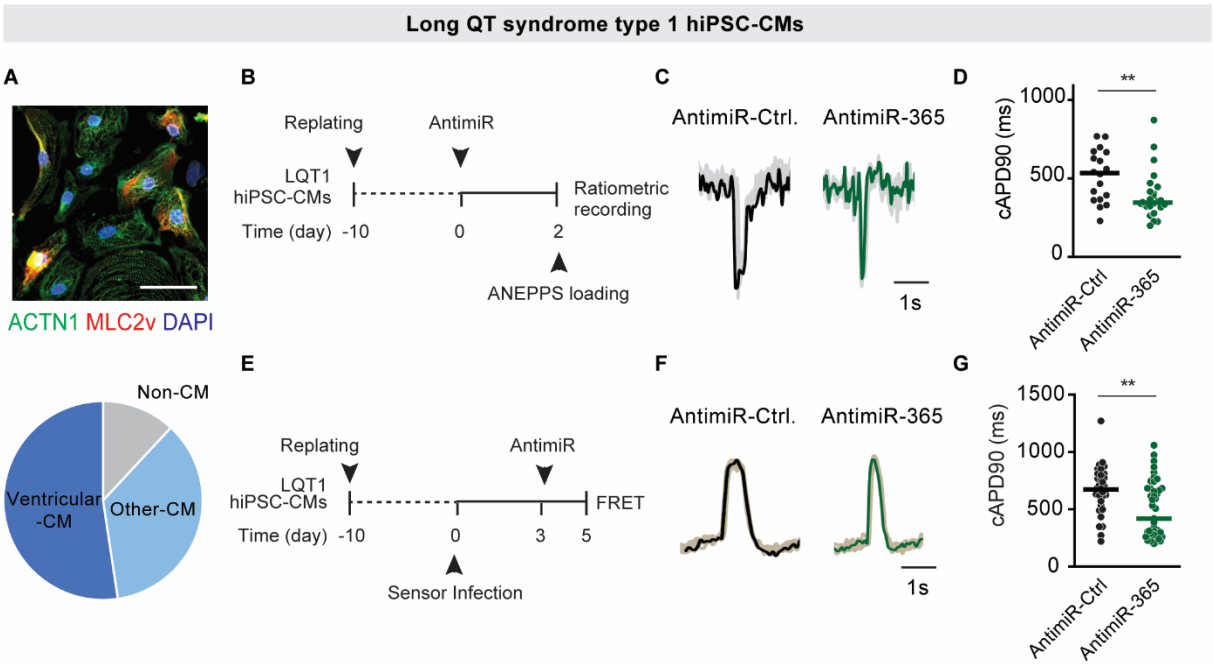

Figure 4.17. Inhibition of miR-365 for shortening AP duration in hiPSC-CMs from patients with Long QT syndrome type 1 (LQT1). (A) Staining of LQT1 hiPSC-CMs for cardiac markers ACTN2 and MYL2 (upper panel). The pie chart (lower panel) shows the proportion of myocytes populations (Data is acquired from 3 independent differentiations). **(B)** Experimental scheme for ANEPPS-based AP recording in LQT1 hiPSC-CMs after transfection with antimiR-365 or -Ctrl. **(C)** F665/F560 traces, averaged from 5-10 recorded APs in one exemplary LQT1 hiPSC-CM, treated with either antimiR-ctrl (black) or antimiR-365 (green). **(D)** Quantification of optical AP recordings in the bulk population of cardiac myocytes. APD is pathologically prolonged in control-treated SQT1 hiPSC-CMs (median 534 ms compared to 346 ms in antimiR-365 treated cells, from 18-26 cells per condition from 3 independent experiments). A Mann-Whitney test was used to assess whether the change is significant (** P-value < 0.01). **(E)** Experimental scheme of FRET-based AP recording in LQT1 hiPSC-CMs after miR-365 inhibition. **(F)** Averaged AP traces (10-15 single APs) recorded from representative LQT1 hiPSC-CMs treated with antimiR-ctrl (black) and antimiR-365 (green). **(G)** Quantification of optical AP recordings selectively in ventricular-like LQT1 hiPSC-CMs using MYL2-VSFP-CR (median 673 ms in the antimiR-ctrl group compared to 418 ms in antimiR-365 treated cells). Data were acquired from 34-43 cells per condition from 4 independent experiments. (** P-value < 0.01 calculated by Mann-Whitney test). This figure has been partially used in our publication[256].

Taken together, these results obtained in myocytes derived from patients suffering from QT abnormalities (SQT1 and LQT1) demonstrate that manipulation of miR-365 activity through synthetic oligonucleotides is feasible in these cells and overexpression of this miRNA can effectively prolong pathologically shortened APD in such as in SQT1, while inhibition of miR-365 can normalize prolonged APD observed in conditions similar to LQT1.

4.4 Characterization of miR-365-based action potential regulation in human myocardial slices

Next, the experiments were extended to intact human myocardium to evaluate whether the regulatory role of miR-365 demonstrated in human cardiac myocytes can be translated to a complex multicellular system such as human myocardial slices. To this end, human left ventricular myocardial tissue was obtained from recipients of heart transplantation surgeries, and thin (300 µm) slices were prepared from this tissue using a vibratome (**Figure 4.18 A**).

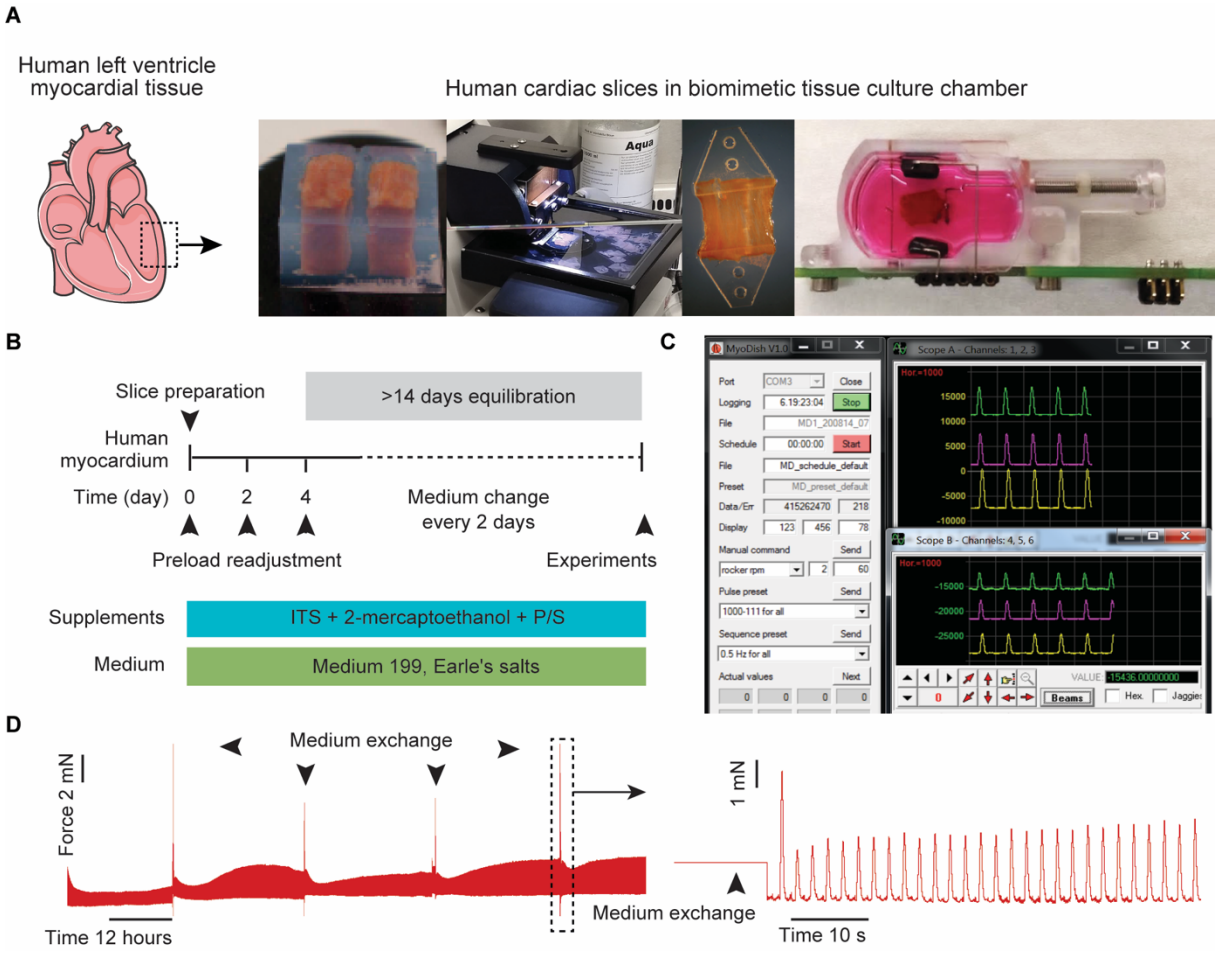

Figure 4.18. Human myocardial slices as an *ex vivo* model to study the role of miR-365 in AP regulation. (**A**) The human ventricular myocardium was embedded in agarose gel and 300 µm slices were prepared using a vibratome. After identifying the orientation of myocytes, the slices were glued to plastic triangles and mounted in biomimetic tissue culture chambers. The slices were cultured under 1 mN preload and 0.5 Hz electrical pacing for at least 2 weeks before starting the functional experiments to reach an equilibrium. The contraction force was measured constantly. **(B)** Scheme showing the steps in preparation and cultivation of human myocardial slices. **(C)** Screenshot of the data acquisition software (Myodish v1.0) representing the controller options (right) and exemplary contraction force traces from 6 different slices (right). **(D)** Contraction force measurement from a representative slice over a 10-day time span of continuous cultivation (left) and at a higher resolution immediately after the medium exchange (right). This figure has been partially used in our publication[256].

The slices were glued to plastic triangles, mounted onto biomimetic tissue culture chambers and cultivated under constant electrical stimulation (0.5 Hz) and physiological preload (1 mN), providing mechanical stimulation. This condition recapitulates the physiological state of the heart and enables long-term survival and contraction of myocardial slices for up to a few months[230]. Slices were cultured for at least two weeks in order for the system to equilibrate to culture conditions and the contraction force was monitored until it reached a strong and stable pattern at the steady-state (**Figure 4.18 B-D**). To establish means to manipulate miRNA levels in cardiac slices, transduction of AAVs or transfection of synthetic miR-365 mimics or antimiRs were tested (**Figure 4.19 A**). To assess the feasibility of transfection, a fluorescently labeled oligonucleotide (FAM-mimic-Ctrl) was used. Confocal imaging after transfection, showed an uptake of the oligonucleotides in a large fraction of cells (**Figure 4.19 B**).

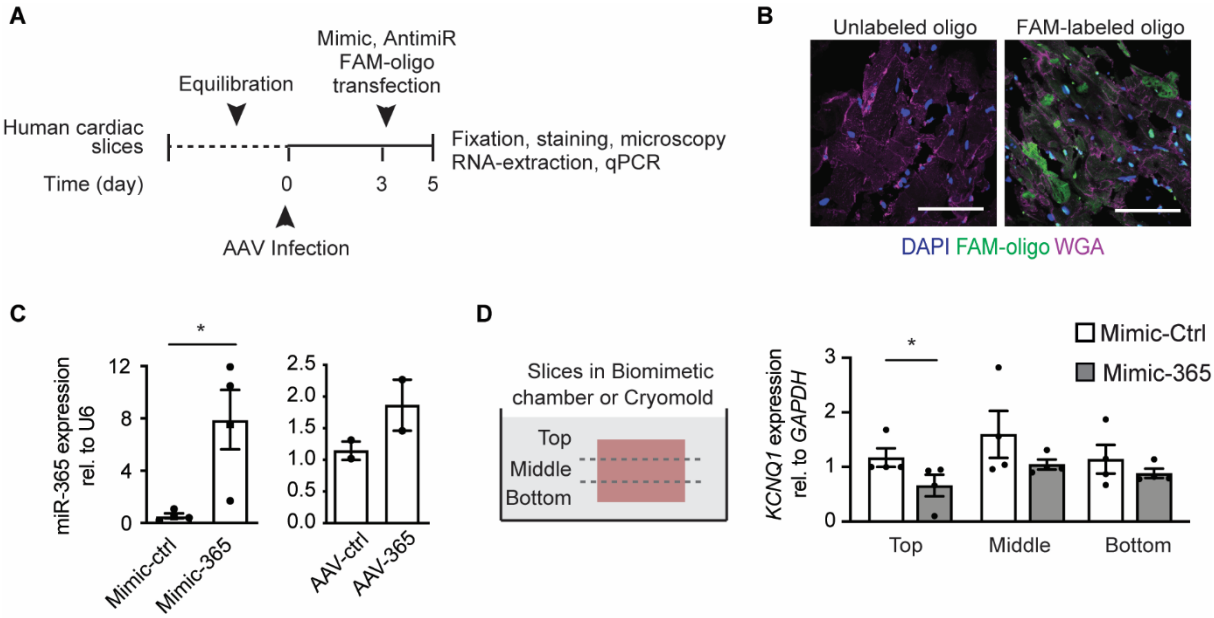

Figure 4.19. MiR-365 manipulation in human myocardial slices. (**A**) Scheme showing various strategies for miR-365 manipulation in human cardiac slices. **(B)** Confocal microscopy of 5 µm sections prepared from myocardial slices transfected with Fluorescein amidite (FAM)-labeled oligonucleotides (green) compared to an untreated slice. Wheat germ agglutinin staining (magenta) defines the area of the cells and DAPI (blue) marks the nuclei (Scale bar represents 75 µm). **(C)** MiR-365 levels in treated slices as determined by qRT-PCR. Slices were transfected with mimic-365 or -ctrl for 48 hours or with AAV6-miR-365 or -ctrl for 5 days (* P-value < 0.05 based on unpaired t-test on 4 independent myocardial slices treated with mimics). **(D)** Scheme representing the localization of human myocardial slices inside the biomimetic culture dish or embedded in a cryomold before making sections for qPCR (left) and qPCR results for *KCNQ1*, a validated target of miR-365, in different layers of a slice. Data is acquired from 4 independent myocardial samples. An unpaired t-test was used to determine the significance of the effect (* P-value < 0.05). All quantitative data are reported as means ± SEM. This figure has been partially used in our publication[256].

Additionally, qPCR experiments revealed that miR-365 levels were 10-fold increased in the slices transfected with mimic-365 compared to mimic-ctrl, further confirming robust penetration of the synthetic mimic into the slices. However, AAV-based overexpression did not prove as

efficient (**Figure 4.19 C**). This was in line with microscopy results on slices infected with AAV6-GFP, where the GFP intensity was unchanged between untreated and infected slices (data not shown). Therefore, for functional characterizations, the transfection of slices with synthetic oligonucleotides was continued. Furthermore, the expression of *KCNQ1* mRNA, a validated target of miR-365, was quantified. *KCNQ1* showed the greatest extent of regulation in the previous experiments on hiPSC-CMs and NRCMs. To assess whether the oligonucleotides reached throughout the entire thickness of slices or the penetration was limited to the superficial part, from each slice, three longitudinal layers were prepared using a microtome. About 40% significant repression of *KCNQ1* was observed in the top layer, while in the middle and bottom of sections, the repression occurred to a lesser extent upon miR-365 transfection (**Figure 4.19 D**).

As a measure of myocardial repolarization, the refractory period (RP) was used. RP is defined as the interval when the tissue has not entirely repolarized following a preceding excitation-contraction and is thus unresponsive to a new depolarizing stimulus. As the RP spans through the complete repolarization of the membrane, it therefore directly correlates with the APD of comprising cardiac myocytes. Upon transfection of human myocardial slices with mimics or antimiRs, the RP was assessed using a programmed electrical stimulation. The protocol involved constant measurement of contraction force upon paired electrical triggers that were set at decreasing intervals (from 1000 to 250 ms). The longest inter-stimulus interval that failed to induce two distinct contractions was considered as the RP of each slice (**Figure 4.20 A, B**). RP recordings were performed pre- and 48 hours post-transfection and revealed 30 ± 5 ms prolongation of RP duration upon transfection of mimic-365 (**Figure 4.20 C, E**) and 50 ± 12 ms shortening of RP after antimiR-365 treatment (**Figure 4.20 D, F**). Transfection of antimiR-Ctrl or mimic-Ctrl did not alter the RP (**Figure 4.20 E, F**).

Taken together, these results demonstrated the feasibility of the administration of synthetic miR-365 mimics and antimiRs for the modulation of APD in intact human myocardial slices.

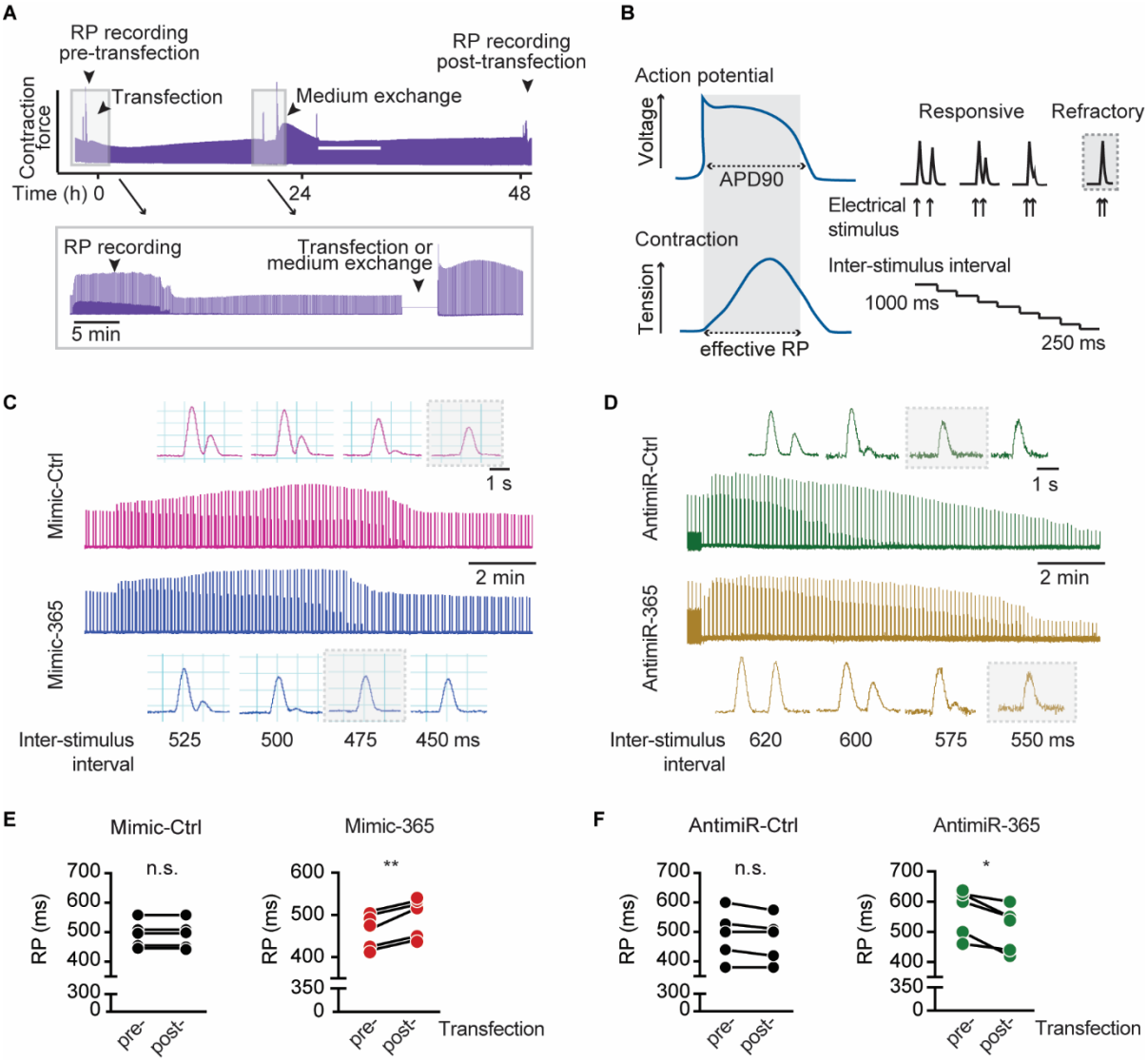

Figure 4.20. Augmentation of miR-365 levels prolongs APD in intact human myocardium. **(A)** Schemes showing the experiment timeline for cultivation and transfection of human myocardial slices with mimic and antimiRs. **(B)** The electrical stimulation program for determining the refractory period in slices. The automated protocol contains two subsequent triggers with defined intervals enabling the determination of the cardiac refractory period (RP), which serves as a measure of AP duration. **(C)** Representative traces depict a detailed representation of an individual round of RP measurements in slices treated with mimic-control (pink) or mimic-365 (blue) 48 hours after transfection. **(D)** Representative high-resolution contraction force traces were acquired from slices transfected with antimiR-ctrl (green) or antimiR-365 (brown) 48 hours after transfection. **(E, F)** Quantitative analysis of RP recordings upon miR-365 elevation (E) or inhibition (F). Cardiac tissue was acquired from 5 independent patients. Statistical significance is determined using a two-tailed paired t-test. Absolute RPs are reported before and after transfection. This figure has also been used in our publication[256].

5 Discussion and outlook

5.1 MiRNA-based regulation of cardiac action potential

An orchestrated expression and function of multiple ion channels enables the formation of a normal cardiac AP. Abnormalities of AP, particularly in ventricles, lay the ground for severe arrhythmia and SCD. Harnessing the regulatory role of non-coding RNAs such as miRNAs on the ion channel mRNAs provides an opportunity for developing novel therapeutics.

Here, to identify the miRNAs that potentially regulate the human cardiac AP, a quantitative analysis based on the predicted miRNA-targetomes was performed. Deep sequencing of total RNA and small RNAs of hiPSC-CMs and human left ventricular myocardium yielded the human ventricular myocyte-specific “channelome” and “miRNome”. The “channelome” was defined as all of the ion channel genes contributing to AP formation and were highly expressed in both hiPSC-CMs and the myocardium. The “miRNome” included all of the miRNAs that were abundantly expressed in both specimens since a moderate to high endogenous expression level is crucial for the functionality of miRNAs[85,266]. Sequencing hiPSC-CMs provided the myocyte-specific transcriptome and miRNome, and since the majority of hiPSC-CMs exhibit a ventricular-like phenotype and gene expression profile (as demonstrated in **Figure 4.1** and **Figure 4.13**), the resulted expression profiles were biased toward ventricular myocyte-specific profiles. However, the main limitation of hiPSC-CMs is their immaturity, and therefore, the data acquired from these cells were supplemented with available data on the human left ventricular myocardium to have the gene and miRNA expression profiles of the adult myocytes. It became more evident that the myocardium contains various cell types besides the myocytes and even in more abundant numbers, especially following the recent single cell RNA-seq studies[267,268]. Thus, the data obtained from the total myocardium is an estimation of the bulk expression throughout all the different cell types, though still biased toward the cardiac myocytes, as the cellular deconvolution algorithms have revealed that myocytes hold a great share of the transcriptome content[269]. Therefore, the human iPSC-CMs and left ventricular myocardium profiles are complementary and by combining them, tissue and cell type specificity, as well as the maturity of the myocytes were taken into account. Recently, another study simultaneously determined the miRNA and mRNA expression profiles of human left ventricular myocardium[270]. These profiles were comparable to the currently used myocardium datasets and yielded similar results, with miR-365 as the primary miRNA with the most predicted binding sites within the 3’ UTR of the ion channel mRNAs (data now shown).

Interestingly, next to miR-365, this analysis predicted other miRNAs in lower ranks that have been shown to be involved in regulating AP or arrhythmogenesis. For instance, miR-1 has been reported to exacerbate arrhythmogenicity, where *KCNJ2* was one of the targets involved

alongside Ca^{2+} handling components and gap juctions[271]. Recently, miR-19 has also been shown to regulate the ventricular AP in zebrafish through targeting multiple ion channels[156], an observation that has yet to be investigated in higher organisms such as humans. Another example is miR-26, a miRNA that has been implicated as a biomarker in AF and exerts a pro-fibrillatory effect by targeting I_{K1} (*KCNJ2* mRNA) in atrial myocytes[272].

For a miRNA to be regarded as a suitable candidate for antiarrhythmic intervention, a moderate expression is favorable. It has been reported that very lowly expressed miRNAs confer only a minimal targeting effect[119]. Whereas modulating miRNAs with very high expression, such as cardiac miRNAs miR-1 and miR-133, has proved to be challenging due to two main reasons: first, the current modulation approaches, such as antimiR, administrated within their safety margin, would not result in full inhibition of highly expressed miRNAs. Second, even when a robust inhibition is achieved, several of the essential biological processes will be obstructed, resulting in unspecific and possibly detrimental effects on the functionality of myocytes, as demonstrated by the high lethality rate in fully knockout animals due to severe cardiac defects[273].

MiR-365 is moderately expressed in cardiac muscle and is among the top 100 highly expressed miRNAs in hiPSC-CMs and left ventricular myocardium (**Figure 4.4**). In human cardiac tissue, among other miRNAs, the incorporation of miR-365 in AGO2 has been identified by immunoprecipitation, evidence suggesting that this miRNA has an active role in post-transcriptional repression of mRNA targets in cardiac tissue[274]. The *in silico* prediction[113] estimated about 377 transcripts containing conserved binding sites for miR-365 and many of the essential ion channels (e.g., *KCNQ1*, *KCNH2*, *KCNJ2*, *CACNA1C*, *KCNC3*, *KCNA1*) are among these predicted targets. Strikingly, these 377 predicted targets are significantly associated with LQTS, a class of ventricular arrhythmias, among all the hereditary diseases described in humans (**Figure 4.5** and **Table 4.1**). This is due to the fact that the predicted targets of miR-365 comprise one-third of the genes that are known to contribute to LQTS.

Recent studies revealed that the total number of predicted targets also affects the activity of miRNAs. Therefore, miRNAs with a very large predicted targetome exhibit decreased regulatory effects[85,275]. Interestingly, the predicted targetome for miR-365 is comprised of 377 targets, which is enriched with ion channels and is substantially smaller than that of miR-125 and miR-19, the miRNAs following miR-365 in the list of AP-related miRNAs (**Figure 4.3**, with 931 and 1339 predicted targets, respectively), or that of cardiac miRNAs such as miR-1 and miR-133 (predicted to target 896 and 630 transcripts, respectively). While these associations do not infer causality, they provided further evidence to investigate the impact of miR-365 on ventricular AP and QT abnormalities.

5.2 MiR-365 modulates AP in human cardiac myocytes

Following the quantitative analysis of miRNA-targets, miR-365 was selected as a putative regulator of the cardiac AP. Since the majority of the predicted ion channel targets of miR-365 were among repolarizing K^+ channels, it was hypothesized that the elevation of this miRNA causes repression of these ion channel genes and prolongs the AP duration due to the decreased repolarization capacity. To evaluate this, miR-365 was overexpressed in primary rat cardiac myocytes and hiPSC-CMs derived from a healthy subject, and the functional impacts were assessed by optical AP recordings in these cardiac myocytes. Since these cells are terminally differentiated cells, traditional manipulation methods are often inefficient or toxic[276], and therefore, for the elevation of miR-365 levels in these cells, two different transduction- and transfection-based approaches were tested. Transduction of the cardiac myocytes with an AAV-based overexpression vector or transfection of these cells with synthetic miR-365 mimic proved to be comparably efficient as determined by qRT-PCR or a double-fluorescent miRNA-activity sensor. The effective multiplicity of infection (MOI) and the optimal time-point of experiments after the transduction were also determined by qRT-PCR (**Figure 4.6**). Although AAV-based transduction and transfection of miR-365 mimics resulted in a similar elevation of this miRNA in hiPSC-CMs, synthetic oligonucleotides were used as the preferred method for manipulation of miRNA subsequently. This is due to the fact that transfection of oligonucleotides results in a similar alteration of miRNA levels in a shorter time (48 hours instead of 5-7 days) and is more cost-effective. Additionally, synthetic oligonucleotides enable both elevation and inhibition of miRNAs, using miRNA mimics or antimiRs, respectively. From a translational perspective, recent advances in non-viral-based delivery of nucleic acids such as modified mRNA, siRNAs, and miRNAs to cardiac muscle made this approach a promising candidate for pharmacological intervention [277].

For measuring relative changes in the membrane potential and determining AP duration, a genetically encoded voltage sensor known as VSFP-CR was used. This FRET-based sensor was originally developed for sub-millisecond AP measurements in neurons[251] and was recently modified to be used as a subtype-specific AP sensor in cardiac myocytes[218]. The voltage-sensing domain of this genetically engineered voltage indicator is originated from the α-subunit of a voltage-gated K^+ channel in rats and is fused to a pair of bright and photostable fluorescent proteins that act as a FRET pair. Therefore, the voltage changes were reflected as alterations in FRET efficacy between the two fluorescent proteins. This sensor has been expressed under the control of a ventricular-specific promoter, MYL2, and has been robustly delivered to cardiac myocytes using an AAV serotype 6 (AAV6) vector. Of note, AAV6-MYL2-VSFP-CR exhibited a robust and homogenous expression in primary cardiac myocytes prepared from neonatal rat

ventricular tissue within 3-5 days, whereas in hiPSC-CMs, due to the heterogeneity of cell populations, robust expression of the sensor happened at later time-points (after 10-15 days).

The genetically encoded voltage sensor enables a ventricular-specific AP recording; however, the long-term and active viral expression of the transgene in addition to transfection or transduction of miR-365 might cause adverse or confounding effects on the electrical properties of the hiPSC-CMs. Contrarily, the voltage-sensitive dyes, such as di-8-ANEPPS, are applied shortly before the recording, and therefore eliminate any interference with miR-365 effects on hiPSC-CMs. Additionally, these dyes are also more time- and cost-effective. Therefore, these two approaches are complementary and were used in parallel in this study. Although these approaches are fast and reliable compared to conventional techniques such as patch clamp, and even enable cell type-specific recordings of APD when GEVIs are used, the outcome is the relative changes and not the absolute voltage across the membrane. Also, measuring individual currents is not possible. Nevertheless, optical-based AP recordings are the method of choice, especially when measuring integrated responses resulting from affecting multiple cardiac currents. Such regulation is expected for miR-365, considering its broad ion channel targetome, and as has been reported, measuring these complex effects using patch clamp systems might be challenging[278].

Optical AP recording in these settings revealed that elevation of miR-365 significantly prolongs the AP duration in rat and human cardiac myocytes. Although the data shows a similar effect of miR-365 in rat cardiac myocytes, further characterizations were conducted entirely in human cells and disease models for the following reasons: first and foremost, the expression of miR-365 has been demonstrated to be about 4-fold higher in human compared to mouse and rat cardiac myocytes (as determined by qRT-PCR in **Figure 4.4**). This is also in good agreement with previous studies that profiled human and mouse myocardium[257,270,274]. Although miR-365 is evolutionarily conserved, this lack of expression questions the relevance of this miRNA in murine cells, tissue, or disease models. Second, arrhythmia studies in murine models meet considerable obstacles due to the differences in AP properties. Murine models display an almost 10-fold higher heart rate compared to humans, which results in much shorter APD and likewise limits the application of murine models in studies focusing on APD. Furthermore, murine cardiac myocytes exhibit profoundly distinct ion channel repertoires compared to humans. A significant example is the lack of I_{Kr} and I_{Ks} currents in murine myocardium, which not only results in substantially different APs but, of note, *KCNH2* and *KCNQ1*, the genes encoding for the alpha subunits of these absent ion channels, are targets of miR-365.

The hiPSC-CMs, on the other hand, not only display the typical features of human cardiac myocytes but also recapitulate the electrophysiological phenotype of the donor[279]. Therefore, in addition to the healthy hiPSC-CMs, two models of well-defined genetic forms of QT

alteration, namely LQTS and SQTS were exploited. For modeling LQTS, hiPSCs that have been previously derived from an LQT1 patient were used. This male patient carried an autosomal dominant missense mutation in the *KCNQ1* gene, a substitution of G to A, resulting in the formation of glutamine instead of arginine (R190Q). This alteration resulted in comparable prolongation of the QT interval in the patient and the APD in the generated cardiac myocytes. Further characterization of the resulted myocytes revealed that this mutation caused a 70 to 80% reduction in I_{Ks} current due to the suppressed trafficking of the channel to the cell membrane and altered gating properties of the channel[221]. To determine the role of miR-365 in this model, a monolayer-based cardiac differentiation protocol was performed, resulting in a robust generation of beating hiPSC-CMs from this LQT1 hiPSC line. Specific inhibition of miR-365 in LQT1 hiPSC-CMs was achieved by transfection of these cells with a synthetic LNA-antimiR-365, resulting in a significant normalization of pathologically prolonged APD.

As a model of SQTS, a recently developed hiPSC model of SQT1 was investigated[225]. SQT1 hiPSCs were derived from a male patient carrying a C to G mutation resulting in the substitution of asparagine to a lysine (N588K) in the *KCNH2* gene. This mutation is known to impair the inactivation of KCNH2 channels and therefore enhance the steady-state I_{Kr} current. In cardiac myocytes derived from this patient, an increased *KCNH2* expression at mRNA and protein levels was also observed[225]. To study the role of miR-365, these SQT1 hiPSCs were differentiated to cardiac myocytes using a modified version of the protocol, which was used for the control and LQT1 cell lines, including a stronger activation of the WNT-signaling pathway. In the resulted hiPSC-CMs, miR-365 levels were elevated using mimic-365, following the observation in the healthy hiPSC-CMs, where overexpression of miR-365 resulted in prolongation of APD. Interestingly, *KCNH2* is also a validated target of miR-365 as shown here and in another study in neurons[280], and since SQT1 is accompanied by the increased levels of KCNH2 mRNA, miR-365-based repression of this gene was expected to be beneficial in restoring the shortened QT. Indeed, the administration of mimic-365 prolonged the APD in SQT1 hiPSC-CMs to relatively normal durations.

All three hiPSC lines were generated by reprogramming dermal fibroblasts with OCT3/4, SOX2, KLF4, and c-MYC transcription factors. For overexpressing these factors in the control[240] and the SQT1[225] cells, Sendai viruses were used, whereas, for LQT1 cells, retroviral vectors were used instead[221]. These different genetic modifications during reprogramming, as well as possible alterations during cultivation of hiPSCs, and differentiation-dependent heterogeneity of the resulted cardiac myocytes prevent the direct comparison between the healthy, SQT1 and LQT1 cell lines. Nevertheless, the SQT1 and LQT1 hiPSC-CMs showed relatively shorter and longer APDs at the basal level, respectively, and the effects of miR-365 on each cell line have been very well controlled by using corresponding control oligonucleotides (antimir-Ctrl and mimic-Ctrl).

While these proof-of-concept experiments revealed the modulatory role of miR-365 on APD abnormalities in patient-specific hiPSC-CM models, naturally, the known limitations of hiPSC-CMs apply. For instance, further analysis on hiPSC-CMs derived from additional patients with LQT1 and SQT1 will be needed to determine the broader potential of miR-365 in the restoration of APD. These analyses can also be expanded on hiPSC-CMs derived from a larger number of patients with other types of LQTS and SQTS. Also, employing isogenic control hiPSC-CMs, genetically matched control cells in which the underlying mutation is corrected by genetic means, have been reported to be advantageous for distinguishing between pathologically relevant effects and other background or unspecific variations[224].

In addition, a certain degree of immaturity in modeling adult human cardiac myocytes, differences in morphological structure and ion channel expression patterns might impact the functional properties and the extent of arrhythmogenic response in these cells[279,281]. However, due to the importance of these cells in various fields of research, namely arrhythmia studies, improving the maturation of hiPSC-CMs is still a work in progress. Recent studies reported on improved physiological functions of hiPSC-derived cardiac myocytes upon mechanical and electrical stimulation and metabolic induction of maturation[282,283].

Similarly, the two-dimensional (2D) cultivation system of hiPSC-CMs in the absence of other relevant cell types might not reflect the conditions that can be found in the adult heart[206,282]. To circumvent these issues, models such as the engineered heart tissue (EHT)[281], three-dimensional (3D) structures comprised of hiPSC-CMs on a matrix, engineered heart myocardium (EHM) models, comprised of hiPSC-derived cardiac myocytes and fibroblasts, and heart-on-a-chip models including hiPSC-derived cardiac myocytes, vascular endothelial, and smooth muscle cells[284] have been developed. More advanced morphological, molecular, and functional maturation of the hiPSC-CMs in these models allow for organotypic responses to physiological and pathological stimuli and provide more reliable platforms for arrhythmia studies.

5.3 MiR-365 regulates AP through shaping a distinct transcriptome signature

The initial *in silico* analysis identified a remarkable enrichment of canonical binding sites for miR-365 in several ion channels, including *KCNQ1*, *KCNH2*, *KCNJ2*, *CACNA1C*, *KCNC3*, *KCNA1*, and *KCNJ3*. These are the genes encoding for the α-subunit of the most important ion channels that determine the repolarization phase of the human ventricular AP. The possibility of direct interactions between miR-365 and the 3’ UTR of all of these ion channels has been evaluated by performing double fluorescent (df-) reporter assays. These reporter constructs, are variations of classically used luciferase-based reporters, that carry two

fluorescent proteins (here, eGFP and tdTomato) instead of bioluminescent proteins (such as Firefly or Renilla luciferases), however, they follow the same principle: the two reporter proteins are expressed under the control of independent promoters, and one serves as a control while the other is fused to the 3' UTR of the predicted target gene and therefore, its expression is impacted post-transcriptionally by the intended miRNA[285]. To control for unspecific effects, a reporter construct containing the same 3' UTR with a mutated binding site is included in these experiments. The df-reporters enable high-sensitivity detection of miRNA-target interactions at the single cell level and with lower variability compared to the bulk bioluminescence readings. By co-transfection of each of these df-reporter constructs and miR-365 mimic into HEK293 cells, the interaction between this miRNA and its binding sites within the 3' UTR of *KCNQ1*, *KCNH2*, *KCNJ2*, *CACNA1C*, *KCNC3*, *KCNA1*, and *KCNJ3* genes was validated. This was observed as a reduction of the GFP signal, whereas the RFP signal remained stable. Of note, the *KCNH2* reporter showed lower repression compared to the other targets (approximately 20% repression upon mimic-365 transfection compared to the control) and in the case of *KCNJ3*, the seed-mutated df-reporter also showed certain levels of repression, possibly due to the fact that *KCNJ3* carries two binding sites for miR-365 that are located in about 400 nucleotides proximity and cause a more complex interaction of the RISC with the 3' UTR.

Although df-reporter assays provide valuable insight on the possibility of miRNA-target interactions, these experiments have been performed in HEK293 cells that possess a very distinct miRNA and gene expression profile, which is entirely different from the one of cardiac myocytes. Therefore, possible competitions between the endogenous miRNAs to bind to the same target or between the targets to bind to a certain miRNA are neglected. As a consequence, df-reporter assays deliver evidence for interactions between miRNA and mRNAs and not necessarily the functional alteration of target levels.

Thus, to gain a deeper understanding of the mechanism of action of miR-365 in the context of cardiac myocytes, extensive transcriptome analyses have been performed on healthy hiPSC-CMs treated with miR-365 mimics and antimiRs. Single cell RNA-sequencing (scRNA-seq), a recently emerged technique, enabled characterization of gene expression profiles at a high resolution in individual cells, and therefore identification of cell-type specific gene expression changes and responses upon treating the cells with miR-365. One of the main limitations of droplet-based scRNA-seq methods in the cardiovascular field is the restriction of input cell size. This means that larger cells such as adult cardiac myocytes (with a diameter of approximately 100 µm) cannot be processed using these setups due to the limited diameter (<30 µm) of the microfluidic tubes used for single cell droplet preparation[286]. An advantage of hiPSC-CMs is their small diameters (approximately 15-20 µm) that allow for droplet-based scRNA-seq. This experiment revealed that the heterogeneous population of cardiac myocytes derived from healthy hiPSCs consists of mostly ventricular-like cells, while smaller fractions of

other cardiac myocytes have also been present. These cells expressed genes characteristics for atrial-like and outflow tract-like cardiac myocytes. Interestingly, the cell compositions detected by scRNA-seq resembled the proportion of cells identified by immunostaining of healthy hiPSC-CMs. After the identification of cell populations, the expression of repolarization-associated ion channels targets of miR-365 was determined in each subpopulation. Among these genes, *KCNQ1*, *KCNJ2*, *KCNJ3*, *CACNA1C* and, *KCNH2* were specifically expressed in the ventricular-like population, while *KCNA1* expression appeared to be higher in atrial-like cells, and *KCNC3* showed a similar expression in ventricular- and atrial-like populations (data not shown). Among the predicted and validated targets of miR-365 only *KCNQ1*, *KCNJ2*, *KCNJ3* and *KCNC3* were repressed in mimic-365-treated cells. Interestingly, the *CACNA1C* gene, which is responsible for the depolarizing current, $I_{Ca,L}$, and acts toward prolongation of APD was unaffected, leaving miR-365 to repress the repolarizing K^+ channels in human ventricular myocytes and explaining the prolonging effect of this miRNA on AP.

Another limitation of scRNA-seq is its low capture efficiency and high dropout rate due to the low amount of starting material (RNA content of only one cell). These result in a fewer number of detected genes and higher noise in scRNA-seq experiments, especially compromising the detection of lowly expressed genes[287]. Since the ion channel targets of miR-365 (and in general ion channels) belong to the class of lowly to moderately expressed genes, the scRNA-seq experiment was complemented with bulk RNA-seq of healthy hiPSC-CMs.

Deep RNA-seq analysis corroborated the key cardiac repolarizing channels as direct targets of miR-365 and revealed alterations of additional AP-regulating genes by this miRNA. For instance, mRNAs coding for pore-forming or accessory domains of other repolarizing ion channels (*e.g.*, *KCNE4*, *KCNC4*, *KCNJ12*) were similarly repressed. In addition, the elevation of miR-365 caused downregulation of important regulatory factors such as potassium channel-regulating kinases (*SGK3* and *SGK1*), caveolins (*CAV1* and *CAV3*), and ankyrins (*ANK3* and *ANK2*) are shown to affect other ion currents by modulating ion channel protein assembly, trafficking and activation[25,288]. Noteworthy, *CAV1*, *CAV3* and *ANK2* are also associated with various types of LQTS[59,289]. *ANK3*, *SGK1* and *SGK3* each contain one conserved binding site for miR-365 and are perhaps direct targets of miR-365. The validity of these targeting events must be assessed using df-reporter assays. However, the repression of other genes possibly happens through indirect regulatory pathways, with upstream regulatory elements that are potentially direct targets of miR-365, a hypothesis that remains to be tested.

Among the initially predicted targets of miR-365, an interesting observation has been made in the case of *KCNH2*. This important gene that is responsible for the I_{Kr} current was validated to interact with miR-365 using df-reporter assays in HEK293 cells, and its expression was downregulated upon miR-365 elevation in primary rat cardiac myocytes at mRNA level.

However, following transcriptome analyses at bulk and single cell level in human cardiac myocytes, *KCNH2* showed a subtle upregulation upon elevation of miR-365 rather than repression. This is probably due to the compensatory effect of the cardiac "repolarization reserve", meaning that significant repression of I_{Ks} (*KCNQ1*) and I_{K1} (*KCNJ2*) is possibly compensated by elevation of *KCNH2*. In ventricular myocytes, this phenomenon happens to maintain a stable repolarizing current and thereby an unchanged APD[19]. However, since functional data in these cells showed a prolongation of APD upon miR-365 elevation, this compensation must have been partial in hiPSC-CMs, not overcoming the effect of miR-365 on decreasing the repolarizing currents. In fact, the repolarization reserve is one of the hurdles in the application of specific repolarizing K^+ channel blockers (Class III antiarrhythmic drugs) as a therapeutic approach since blocking one current would not be sufficient to exert any effect on APD[290]. The simultaneous targeting of these three dominating repolarizing channels by miR-365, while maintaining the miRNA-inherent high degree of target specificity makes this miRNA an effective modulator of APD.

While miR-365 has not been previously linked to regulation of cardiac ion channels or arrhythmia, targeting of *Kcnh2* by miR-365 has been reported in the central nervous system, where this interaction affected the excitability of neurons[280]. The observation that miR-365 represses *KCNH2* in neurons as well as in rat primary myocytes, and not in healthy hiPSC-CMs is further proof of context-specific effects of miRNAs. Therefore, as a perspective, performing transcriptome analysis in LQT1 and SQT1 hiPSC-CMs upon treatments with antimiR- and mimic-365 might possibly reveal a cell type-specific target repression pattern by miR-365 in these arrhythmia models. This approach would take parameters such as the endogenous concentration of the ion channels and miR-365 into account. This is especially important since the mutated ion channels in human QT syndromes are often among the targets of miR-365, and transcriptome analyses in these cells provide information on the differential effects of miR-365 on the native and mutated isoforms of the ion channels.

In summary, it has been demonstrated that miR-365 modulates a complex set of direct and indirect target genes that together shape the repolarization phase of the AP in human cardiac myocytes. Such synergistic regulation of the AP may also provide for new therapeutic opportunities by overcoming the compensatory mechanisms of cardiac myocytes.

5.4 The translational perspective of miR-365-based AP regulation

Although the regulatory role of miR-365 on the cardiac AP was successfully demonstrated in hiPSC-CMs, a direct and reliable translation of these results to human myocardium is challenging. This is due to the existing limitations of these models such as relative immaturity

of the resulted myocytes, differentiation-dependent and cell line-dependent variabilities, as well as the absence of cell-cell and cell-ECM interactions that natively occur in the myocardium. These shortcomings are not limited to hiPSC-CMs but apply to other existing human-based models in cardiovascular research. For instance, the isolated adult cardiac myocytes undergo enzymatic dissociation protocols that remove the ECM and native cellular interactions and often result in remodeling of the morphology and function of myocytes within a few hours. Even the tissue-engineering-based models that are developed more recently, such as engineered heart tissue or heart-on-a-chip, are still in their infancy and do not fully incorporate the complex cell composition of the native myocardial tissue.

Human myocardial tissue slices provide a clinically relevant model that represents the complexity and function of the adult human heart. Methods for preparation and cultivation of human myocardial slices saw considerable advances recently that now the multicellularity and the noncellular architecture of the native myocardium are almost fully preserved. Biomimetic cultivation criteria permit maintenance of multiple cardiac tissue slices in parallel, with constant mechanical and electrical stimulation and over prolonged periods of time for up to a few months. These models are probably the closest model to intact human myocardium, exhibiting its developmental maturity and the conservation of the native structure, which substantially circumvent the limitations of other models such as hiPSC-CMs. Using this platform and performing refractory period measurements upon treatment with miR-365 mimics or antimiRs, the modulatory effect of miR-365 on AP duration was substantiated also in adult human myocardial tissue.

In more recent studies, the slices have been used for drug screening and modeling of diseases such as heart failure[233] and muscular dystrophy[291] and optical-based recordings of Ca^{2+} transients and APD have been performed in human cardiac slices[291–293]. For gene delivery, the feasibility of transduction of slices with adenovirus particles carrying GFP has been reported before[292,294]. However, there were no quantitative analysis showing the efficacy of this approach. In fact, robust manipulation, and subsequent functional characterization of a candidate in human myocardial slices have not been reported previously, and the current study is one of the first attempts for such an approach. Here, transfection of synthetic mimics and antimiRs resulted in significant alteration of endogenous miRNA, as demonstrated by distribution of fluorescently labeled mimic molecules within the tissue and by quantification of miRNA and target levels using qRT-PCR. These experiments revealed a significant elevation of miR-365 upon transfection of myocardial slices with mimic-365 and consequently, repression of *KCNQ1*, a validated target of miR-365 was observed in different layers of the tissue. This suggests the applicability of transfection of modified RNAs (modRNAs) as a possibility for overexpression of coding genes in human myocardial slices. With further

optimizations, the efficiency of delivery can be improved, particularly into the inner layers of the tissue.

Application of human myocardial slices in translational research is still in progress, and studies to better understand the exact composition of surviving cells after slice preparation and the effects of the long-term culture on each cell type are necessary. The lack of systemic neurohormonal regulations is also a remaining limitation of myocardial slices to fully recapitulate the intact human myocardium.

As a translational perspective, the effect of miR-365 in controlling AP can also be characterized in preclinical animal models. As discussed in section 5.2, significant differences in the basal expression of miR-365, the ion channel repertoire and electrophysiological properties restrict the applicability of murine models, however, rabbit and porcine models are two noteworthy examples of small and large animal models. Unlike murine myocardium, rabbits exhibit a robust expression of I_{Kr} and I_{Ks} currents (encoded by *KCNH2* and *KCNQ1*) resulting in a longer APD comparable to humans. In recent years, several transgenic rabbit models for various types of QT syndromes, namely LQT1, LQT2, LQT5 and SQT1 have been generated by cardiac-specific overexpression of mutated isoforms of human *KCNQ1*, *KCNH2* and *KCNE1*, and the native human *KCNH2* gene, respectively. These animal models represent different extents of repolarization impairment[208,295], and can be employed to evaluate the *in vivo* effects of miR-365 manipulation. However, the endogenous expression of miR-365 is not known in rabbit myocardium. Pig models also share key similarities with humans, such as the anatomical properties, heart rate and electrophysiological properties. Interestingly, miR-365 showed a robust expression in the porcine myocardium. In addition, systemic injection of antimiRs and AAV-based overexpression strategies, as well as precise electrocardiography techniques are well established in these large animal models[95,296], making them a suitable model to study the *in vivo* relevance of miR-365 on cardiac rhythm control.

The application of miR-365 as an AP regulator is not necessarily restricted to congenital channelopathies and can be extended to arrhythmias that occur as a result of structural remodeling in the myocardium or drug-induced arrhythmias. Interestingly, the very first report on a possible relevance of miR-365 in the cardiovascular system was a study of our group, where miR-365 was identified as pro-hypertrophic miRNA in a phenotypic screen for cardiac hypertrophy in rodents cardiac myocytes[191]. Another study further extended this finding in a TAC model of pressure overload in mice[192]. Although the involvement of miR-365 in hypertrophy in an *in vivo* setting was shown in this study, the changes in the electrical properties of these mice were not determined. Nevertheless, prolongation of the QT interval has been associated with TAC models[199], and the effects of miR-365 on hypertrophy-induced arrhythmias should be further investigated. QT prolongations also occur as an undesirable

side effect of a large number of drugs. Drug-induced QT prolongations can trigger life-threatening episodes of arrhythmia in healthy individuals with normal cardiac repolarization otherwise, therefore is a hurdle in drug development[67]. These arrhythmias typically happen due to the blockage of KCNH2 channels that is a validated target of miR-365, but irrespective of this, the overall impact of miR-365 manipulation on AP regulatory networks might rescue these types of APD prolongation.

Pharmacologically, miR-365 might circumvent some of the shortcomings of the Class III antiarrhythmic drugs. These drugs are comprised of K^+ channel blockers with different degrees of specificity that can be used in modulating diseases such as SQTS. However, an increased risk of proarrhythmic events is the main hurdle for their application. Targeting repolarizing K^+ channels through manipulation of miR-365 effectively alters the APD by overcoming the repolarization reserve. Unlike the unspecific K^+ channel blockers, which often increase the risk of arrhythmogenesis, the effect of miR-365 is accompanied by the inherent safety of miRNAs as miRNA-based regulation quickly reaches saturation and typically does not exceed a limit of 50% of target gene regulation, even at very high miRNA concentrations[266]. A further limitation of conventional K^+ channel blockers is that this class of antiarrhythmic drugs typically increase the risk of reactivation of Ca^{2+} channels and therefore the occurrence of EADs as a consequence of the prolonged repolarization phase[19,297]. A possible advantage of miR-365 in this regard is that simultaneously to the main repolarization reserve K^+ ion channels, this miRNA also targets the voltage-gated Ca^{2+} channel mRNA (*CACNA1C*) to a lesser extent, omitting the risk of proarrhythmic events effect of miR-365.

In humans, the highest expression of miR-365 has been observed in cardiac and skeletal muscle and adipose tissue[298], yet an involvement of miR-365 has also been reported in various cancers, immune cells and nervous system[299,300]. Therefore, the off-targets and probable side effects of miR-365 must be evaluated cautiously.

In summary, in this first study on the role of miR-365 in cardiac rhythm control, the utility of this miRNA in modulating APD has been demonstrated in an exemplary way in cardiac myocytes generated from a healthy individual and from patients suffering from congenital channelopathies, namely SQT1 and LQT1. Similar regulation of AP by miR-365 was observed in human myocardial tissue slices. These data suggest that by targeting and repressing several repolarizing ion channels and additional AP regulators, miR-365 prolongs the APD. Taken together, the presented data indicate a crucial role for miR-365 in the control of the human cardiac AP and suggest further studies to determine its therapeutic potential (**Figure 5.1**).

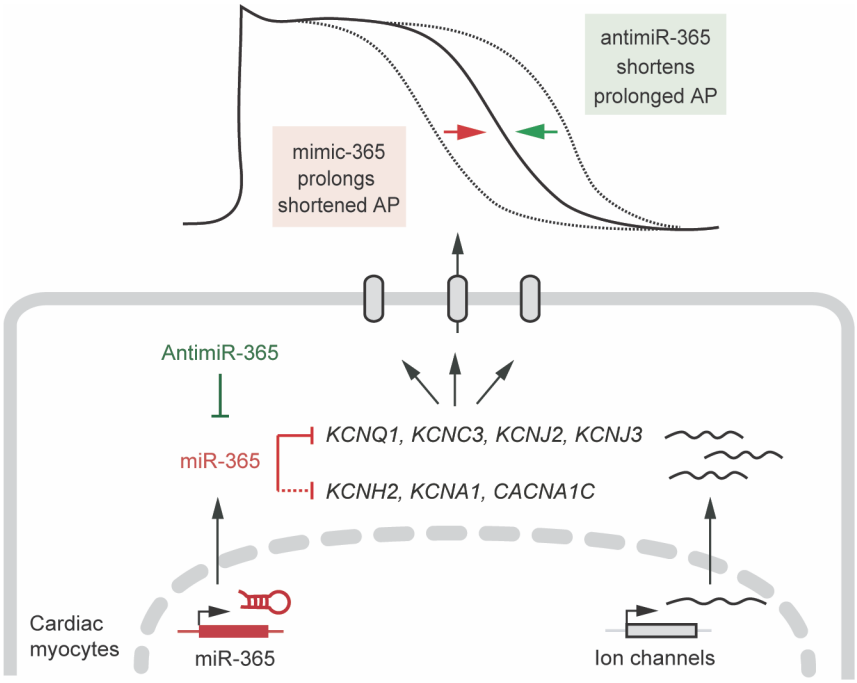

Figure 5.1. Proposed mechanism for the regulatory role of miR-365 on the cardiac action potential. In cardiac myocytes, miR-365 represses multiple repolarizing ion channels such as KCNQ1, KCNJ2, KCNJ3 and KCNC3 upon direct interaction with their 3' UTR and thereby, results in prolongation of AP duration. The therapeutic modulation of miR-365 using specific mimics and antimiRs is sufficient to restore pathologically altered APD to normal levels. Such alterations are observed in various QT syndromes such as LQTS and SQTS.

5.5 Non-coding RNAs as novel antiarrhythmic targets

Current pharmacological treatments for ventricular arrhythmias, although partially effective, met considerable challenges such as unresponsiveness of the individuals, or unspecific effects on the other components of cardiac rhythm formation[48]. Thus, more invasive options such as the implantation of cardioverter-defibrillators or left ventricular sympathetic denervation must be pursued[48,301], which are associated with relevant long-term complications[80]. Thus, new therapeutic avenues for various forms of cardiac arrhythmia are in demand.

Regarding the inherited channelopathies, with the recent progress of gene editing techniques, gene therapy approaches aiming for somatic correction of arrhythmogenic mutations in the myocardium of affected individuals would be curative. However, currently, these interventions are in their infancy and need to be further optimized to be effective and sufficiently specific for the human cardiac muscle[302]. Furthermore, these approaches would mainly target the inherited channelopathies and not the acquired types of arrhythmias.

Non-coding RNA-based techniques on the other hand, provide an attractive opportunity by regulation of various components of AP formation, such as the pore-forming or accessory units of the ion channels and established AP regulatory genes. This is due to the remarkable ability

of some miRNAs to target several distinct, but functionally connected targets, resulting in an effective regulation of whole signaling pathways or complex cellular processes[96].

Additionally, recent advances in manipulating individual miRNA molecules in parallel to the development of AAV-based and non-viral approaches (e.g., lipofection or nucleofection) for delivery of nucleic acids to cardiac muscle make these molecules promising candidates for pharmacological intervention against various cardiovascular diseases including cardiac arrhythmias[277,303].

Although promising, several limitations of miRNA-based therapeutics have been reported. For example, miRNAs that belong to a seed family share their targetome, and therefore an effective manipulation of all the family members is needed to achieve a regulation at the target level. As it is becoming more evident that the functionality of miRNAs depends on the tissue and even the cell-type context, efforts for developing organ- and cell-type-specific delivery tools are necessary. Another example is the sex-dependent functionality that is reported for some miRNAs, a phenomenon that is emerging in many aspects of cardiovascular diseases and needs to be addressed in preclinical studies, before aiming for therapeutic interventions[139,303].

Notwithstanding all these limitations, harnessing the regulatory role of miRNAs may provide powerful means for pharmacological intervention of AP abnormalities in various types of congenital or acquired arrhythmias and could circumvent principal problems of drug development towards key cardiac ion channels.

Non-coding RNA-based regulation of cardiac AP is not restricted to miRNAs and can be expanded to other classes of non-coding RNAs, such as long non-coding RNAs (lncRNAs). lncRNAs are a class of non-coding RNA molecules that are longer than 200 nucleotides and exert their regulatory effects by many different modes, such as affecting chromatin modifications and accessibility, transcriptional activation or inhibition, or modulating translation or splicing at post-transcriptional level[304]. Recent studies revealed the involvement of a few lncRNAs in various aspects of arrhythmogenicity. For instance, lncRNAs KCNA2AS and KCNQ1OT1 are neighboring transcripts to *KCNA2* and *KCNQ1* genes in the opposite strand and inhibit the expression of these two ion channel genes in an antisense manner. KCNA2AS was upregulated in heart failure[305], while KCNQ1OT1 was first described in atrial fibrillation[306] and has been associated with LQTS later[307]. Another example is lncRNA MIAT in the context of atrial fibrillation. This lncRNA has a partial sequence complementarity to *KCNJ2*, although it is not located in the neighboring region of this gene. MIAT reduces the expression of *KCNJ2* through antisense binding and thereby, decreases I_{K1} current. This group of regulatory molecules provides further opportunities for understanding arrhythmogenicity mechanisms and for the development of RNA-based antiarrhythmic interventions[304].

6 Summary

The cardiac action potential (AP) is generated by an orchestrated function of a panel of ion channels. Abnormalities in the expression and function of these ion channels, as observed in long or short QT syndromes, are associated with an increased risk of life-threatening arrhythmias and sudden cardiac death. This study aimed to identify microRNAs (miRNAs) that post-transcriptionally regulate cardiac ion channels and to assess whether manipulation of such miRNAs would allow for modulation of the irregularities of action potential duration (APD). Among miRNAs that are highly expressed in the human cardiac myocytes, miR-365 was identified to target the largest number of repolarizing ion channels. Carrying out double-fluorescent reporter assays, a direct interaction between miR-365 and its corresponding binding sites within *KCNQ1*, *KCNH2*, *KCNJ2*, *CACNA1C*, *KCNC3*, *KCNA1*, and *KCNJ3* mRNAs was confirmed. Interestingly, an independent gene enrichment analysis on all predicted targets of miR-365 primarily associated this miRNA with long QT syndrome among all hereditary diseases in humans.

To resolve the regulatory function of miR-365, optical AP recordings were performed in patient-specific induced pluripotent stem cell-derived cardiac myocytes (hiPSC-CMs) as a human disease model. In hiPSC-CMs derived from a long QT syndrome type 1 patient, the pathologically prolonged APD was restored to normal levels upon inhibition of miR-365 using specific antimiRs, whereas the elevation of miR-365 in short QT type 1 hiPSC-CMs resulted in prolongation of APD and, therefore, normalization of abnormally shortened APD.

Mechanistically, transcriptome analyses in hiPSC-CMs at bulk and single-cell level confirmed direct targeting of the essential cardiac repolarizing channels by miR-365. These analyses revealed that this miRNA exerts its regulatory role by significantly repressing the potassium ion transport machinery and the repolarization phase of the cardiac AP.

Finally, human myocardial tissue slices were employed to determine the relevance of miR-365 in a model that incorporates the complexity of the adult human heart. Slices were prepared from left ventricular myocardium and cultivated under electromechanical stimulation to preserve their structure and function for up to 4 months. Repeated recordings of the refractory period (RP) upon manipulation of miR-365 revealed that elevation of miR-365 significantly prolonged the RP, whereas treatment with antimiR-365 resulted in a shortened RP compared to respective controls.

Taken together, our results delineate miR-365 to regulate cardiac APD through post-transcriptional repression of key determinants of cardiac repolarization. Therefore, manipulation of miR-365 may be employed to modulate APD abnormalities in various human arrhythmias.

7 References

1. Bagnall, R. D. *et al.* A Prospective study of sudden cardiac death among children and young adults. *N. Engl. J. Med.* **374**, 2441–2452 (2016).
2. Skinner, J. R., Winbo, A., Abrams, D., Vohra, J. & Wilde, A. A. Channelopathies that lead to sudden cardiac death: clinical and genetic aspects. *Hear. Lung Circ.* **28**, 22–30 (2019).
3. Wong, C. X. *et al.* Epidemiology of sudden cardiac death: global and regional perspectives. *Hear. Lung Circ.* **28**, 6–14 (2019).
4. Sumner, G. L., Kuriachan, V. P. & Mitchell, L. B. Sudden cardiac death. in *Encyclopedia of cardiovascular research and medicine* 511–520 (Elsevier, 2018).
5. World Health Organization. Global Health Estimates 2019: Global Health Estimates: Life expectancy and leading causes of death and disability. Retrieved from https://www.who.int/data/gho/data/themes/mortality-and-global-health-estimates (2020).
6. Schmitt, N., Grunnet, M. & Olesen, S. P. Cardiac potassium channel subtypes: New roles in repolarization and arrhythmia. *Physiol. Rev.* **94**, 609–653 (2014).
7. Zipes, D. P., Jalife, J. & Stevenson, W. G. *Cardiac electrophysiology: From Cell to Bedside*. (Elsevier, 2017).
8. Issa, Z., Miller, J. M. & Zipes, D. P. *Clinical arrhythmology and electrophysiology: A companion to Braunwald's heart disease*. (Elsevier, 2018).
9. Tosaki, A. ArrhythmoGenoPharmacoTherapy. *Front. Pharmacol.* **11**, 1–19 (2020).
10. Liang, X., Evans, S. M. & Sun, Y. Development of the cardiac pacemaker. *Cell. Mol. Life Sci.* **74**, 1247–1259 (2017).
11. Weisbrod, D., Khun, S. H., Bueno, H., Peretz, A. & Attali, B. Mechanisms underlying the cardiac pacemaker: The role of SK4 calcium-activated potassium channels. *Acta Pharmacol. Sin.* **37**, 82–97 (2016).
12. George, S. A. *et al.* At the atrioventricular crossroads: Dual pathway electrophysiology in the atrioventricular node and its underlying heterogeneities. *Arrhythmia Electrophysiol. Rev.* **6**, 179–185 (2017).
13. Saremi, F. *et al.* Fibrous skeleton of the heart: Anatomic overview and evaluation of pathologic conditions with CT and MR imaging. *Radiographics* **37**, 1330–1351 (2017).
14. Park, D. S. & Fishman, G. I. The cardiac conduction system. *Circulation* **123**, 904–915 (2011).
15. Nerbonne, J. M. & Kass, R. S. Molecular physiology of cardiac repolarization. *Physiol. Rev.* **85**, 1205–53 (2005).
16. Bartos, D. C., Grandi, E. & Ripplinger, C. M. Ion Channels in the Heart. *Compr. Physiol.* **5**, 1423–64 (2015).
17. Bers, D. M. Cardiac excitation–contraction coupling. *Nature* **415**, 198–205 (2002).
18. Chiamvimonvat, N. *et al.* Potassium currents in the heart: functional roles in repolarization, arrhythmia and therapeutics. *J. Physiol.* **595**, 2229–2252 (2017).
19. Schmitt, N., Grunnet, M. & Olesen, S.-P. Cardiac Potassium Channel Subtypes: New Roles in Repolarization and Arrhythmia. *Physiol. Rev.* **94**, 609–653 (2014).
20. Priest, B. T. & McDermott, J. S. Cardiac ion channels. *Channels* **9**, 352–359 (2015).
21. Liu, J., Laksman, Z. & Backx, P. H. The electrophysiological development of cardiomyocytes. *Adv. Drug Deliv. Rev.* **96**, 253–273 (2016).

22. Comollo, T. W., Zhang, C., Zou, X. & Kass, R. S. Physiology and molecular biology of ion channels underlying ventricular repolarization of the mammalian heart. In: El-Sherif N. (eds) *Cardiac Repolarization* (2020).

23. Garg, P. *et al.* Human induced pluripotent stem cell-derived cardiomyocytes as models for cardiac channelopathies: A primer for non-electrophysiologists. *Circ. Res.* **123**, 224–243 (2018).

24. Betzenhauser, M. J., Pitt, G. S. & Antzelevitch, C. Calcium channel mutations in cardiac arrhythmia syndromes. *Curr. Mol. Pharmacol.* **8**, 133–42 (2015).

25. Amin, A. S., Pinto, Y. M. & Wilde, A. A. M. Long QT syndrome: Beyond the causal mutation. *J. Physiol.* **591**, 4125–4139 (2013).

26. Abriel, H., Rougier, J. S. & Jalife, J. Ion channel macromolecular complexes in cardiomyocytes: Roles in sudden cardiac death. *Circ. Res.* **116**, 1971–1988 (2015).

27. Kearney, J. Voltage-gated ion channel accessory subunits: Sodium, potassium, or both? *Epilepsy Curr.* **13**, 30–31 (2013).

28. Remme, C. A. & Wilde, A. A. Targeting sodium channels in cardiac arrhythmia. *Curr. Opin. Pharmacol.* **15**, 53–60 (2014).

29. Bosch, R. F. *et al.* β3-Adrenergic regulation of an ion channel in the heart - Inhibition of the slow delayed rectifier potassium current IKs in guinea pig ventricular myocytes. *Cardiovasc. Res.* **56**, 393–403 (2002).

30. Roden, D. M. & Kupershmidt, S. From genes to channels: Normal mechanisms. *Cardiovasc. Res.* **42**, 318–326 (1999).

31. Rosati, B. & McKinnon, D. Regulation of ion channel expression. *Circ. Res.* **94**, 874–883 (2004).

32. Tomson, T. T. & Arora, R. Modulation of cardiac potassium current by neural tone and ischemia. *Card. Electrophysiol. Clin.* **8**, 349–360 (2016).

33. Roden, D. M. Taking the 'Idio' out of 'Idiosyncratic': Predicting Torsades de Pointes. *Pacing Clin. Electrophysiol.* **21**, 1029–1034 (1998).

34. Nguyen, T. P., Singh, N., Xie, Y., Qu, Z. & Weiss, J. N. Repolarization reserve evolves dynamically during the cardiac action potential: effects of transient outward currents on early afterdepolarizations. *Circ. Arrhythmia Electrophysiol.* **8**, 694–702 (2015).

35. Grant, a. O. Cardiac ion channels. *Circ. Arrhythmia Electrophysiol.* **2**, 185–194 (2009).

36. Rai, V. & Agrawal, D. K. Role of risk stratification and genetics in sudden cardiac death. *Can. J. Physiol. Pharmacol.* **95**, 225–238 (2016).

37. Chugh, S. S. Sudden cardiac death in 2017: Spotlight on prediction and prevention. *Int. J. Cardiol.* **237**, 2–5 (2017).

38. Bezzina, C. R., Lahrouchi, N. & Priori, S. G. Genetics of sudden cardiac death. *Circ. Res.* **116**, 1919–1936 (2015).

39. Deo, R. & Albert, C. M. Epidemiology and genetics of sudden cardiac death. *Circulation* **125**, 620–637 (2012).

40. Lerma, C., Gorelick, A., Ghanem, R. N., Glass, L. & Huikuri, H. V. Patterns of ectopy leading to increased risk of fatal or near-fatal cardiac arrhythmia in patients with depressed left ventricular function after an acute myocardial infarction. *Europace* **15**, 1304–1312 (2013).

41. Deyell, M. W., Krahn, A. D. & Goldberger, J. J. Sudden cardiac death risk stratification. *Circ. Res.* **116**, 1907–1918 (2015).

42. Waldmann, V. *et al.* Association between atrial fibrillation and sudden cardiac death:

pathophysiological and epidemiological insights. *Circ. Res.* 301–309 (2020) doi:10.1161/CIRCRESAHA.120.316756.

43. Farwell, D. & Gollob, M. H. Electrical heart disease: Genetic and molecular basis of cardiac arrhythmias in normal structural hearts. *Can. J. Cardiol.* **23**, 16A-22A (2007).

44. Curcio, A., Santarpia, G. & Indolfi, C. The Brugada syndrome — From gene to therapy —. *Circ. J.* **81**, 290–297 (2017).

45. Antzelevitch, C. & Patocskai, B. Brugada Syndrome: Clinical, genetic, molecular, cellular, and ionic aspects. *Curr. Probl. Cardiol.* **41**, 7–57 (2016).

46. Györke, S. Molecular basis of catecholaminergic polymorphic ventricular tachycardia. *Hear. Rhythm* **6**, 123–129 (2009).

47. Imberti, J. F., Underwood, K., Mazzanti, A. & Priori, S. G. Clinical challenges in catecholaminergic polymorphic ventricular tachycardia. *Hear. Lung Circ.* **25**, 777–783 (2016).

48. Priori, S. G. *et al.* 2015 ESC Guidelines for the management of patients with ventricular arrhythmias and the prevention of sudden cardiac death: The Task Force for the Management of Patients with Ventricular Arrhythmias and the Prevention of Sudden Cardiac Death of the Europe. *Europace* **17**, 1601–1687 (2015).

49. Sallam, K., Li, Y., Sager, P. T., Houser, S. R. & Wu, J. C. finding the rhythm of sudden cardiac death: new opportunities using induced pluripotent stem cell-derived cardiomyocytes. *Circ. Res.* **116**, 1989–2004 (2015).

50. Offerhaus, J. A., Bezzina, C. R. & Wilde, A. A. M. Epidemiology of inherited arrhythmias. *Nat. Rev. Cardiol.* **17**, 205–215 (2020).

51. Hayashi, M., Shimizu, W. & Albert, C. M. The Spectrum of Epidemiology Underlying Sudden Cardiac Death. *Circ. Res.* **116**, 1887–1906 (2015).

52. Sanguinetti, M. C. & Tristani-Firouzi, M. hERG potassium channels and cardiac arrhythmia. *Nature* **440**, 463–469 (2006).

53. Wang, Q. *et al.* Positional cloning of a novel potassium channel gene: KVLQT1 mutations cause cardiac arrhythmias. *Nat. Genet.* **12**, 17–23 (1996).

54. Plaster, N. M. *et al.* Mutations in Kir2.1 cause the developmental and episodic electrical phenotypes of Andersen's Syndrome. *Cell* **105**, 511–519 (2001).

55. Calloe, K. *et al.* Characterizations of a loss-of-function mutation in the Kir3.4 channel subunit. *Biochem. Biophys. Res. Commun.* **364**, 889–895 (2007).

56. Neyroud, N. *et al.* A novel mutation in the potassium channel gene KVLQT1 causes the Jervell and Lange-Nielsen cardioauditory syndrome. *Nat. Genet.* **15**, 186–189 (1997).

57. Abbott, G. W. *et al.* MiRP1 forms I Kr potassium channels with HERG and is associated with cardiac arrhythmia. *Cell* **97**, 175–187 (1999).

58. Belardinelli, L., Giles, W. R., Rajamani, S., Karagueuzian, H. S. & Shryock, J. C. Cardiac late Na+ current: Proarrhythmic effects, roles in long QT syndromes, and pathological relationship to CaMKII and oxidative stress. *Hear. Rhythm* **12**, 440–448 (2015).

59. Giudicessi, J. R. & Ackerman, M. J. Calcium revisited. *Circ. Arrhythmia Electrophysiol.* **9**, 1–11 (2016).

60. Boczek, N. J. *et al.* Identification and functional characterization of a novel CACNA1C - mediated cardiac disorder characterized by prolonged QT intervals with hypertrophic cardiomyopathy, congenital heart defects, and sudden cardiac death. *Circ. Arrhythmia Electrophysiol.* **8**, 1122–1132 (2015).

61. Nomikos, M. *et al.* Altered RyR2 regulation by the calmodulin F90L mutation associated with idiopathic ventricular fibrillation and early sudden cardiac death. *FEBS Lett.* **588**,

2898–2902 (2014).

62. Sondergaard, M. T. *et al.* Arrhythmogenic calmodulin mutations affect the activation and termination of cardiac ryanodine receptor-mediated Ca2+ release. *J. Biol. Chem.* **290**, 26151–26162 (2015).

63. Altmann, H. M. *et al.* Homozygous/compound heterozygous triadin mutations associated with autosomal-recessive Long-QT Syndrome and Pediatric sudden cardiac arrest. *Circulation* **131**, 2051–2060 (2015).

64. Ichikawa, M. *et al.* Phenotypic variability of ANK2 mutations in patients with inherited primary arrhythmia syndromes. *Circ. J.* **80**, 2435–2442 (2016).

65. Kannankeril, P., Roden, D. M. & Darbar, D. Drug-Induced Long QT Syndrome. *Pharmacol. Rev.* **62**, 760–781 (2010).

66. Behr, E. R. & Roden, D. Drug-induced arrhythmia: pharmacogenomic prescribing? *Eur. Heart J.* **34**, 89–95 (2013).

67. Stillitano, F. *et al.* Modeling susceptibility to drug-induced long QT with a panel of subject-specific induced pluripotent stem cells. *Elife* **6**, 1–24 (2017).

68. Brugada, R. *et al.* Sudden death associated with Short-QT Syndrome linked to mutations in HERG. *Circulation* **109**, 30–35 (2004).

69. Bellocq, C. *et al.* Mutation in the KCNQ1 gene leading to the short QT-interval syndrome. *Circulation* **109**, 2394–2397 (2004).

70. Priori, S. G. *et al.* A novel form of Short QT Syndrome (SQT3) is caused by a mutation in the KCNJ2 gene. *Circ. Res.* **96**, 800–807 (2005).

71. Antzelevitch, C. *et al.* Loss-of-function mutations in the cardiac calcium channel underlie a new clinical entity characterized by ST-segment elevation, short QT intervals, and sudden cardiac death. *Circulation* **115**, 442–449 (2007).

72. Gaita, F. *et al.* Short QT Syndrome. *Circulation* **108**, 965–970 (2003).

73. Campuzano, O. *et al.* Recent advances in Short QT Syndrome. *Front. Cardiovasc. Med.* **5**, (2018).

74. Napolitano, C., Bloise, R., Monteforte, N. & Priori, S. G. Sudden cardiac death and genetic ion channelopathies: Long QT, Brugada, short QT, catecholaminergic polymorphic ventricular tachycardia, and idiopathic ventricular fibrillation. *Circulation* **125**, 2027–2034 (2012).

75. Al-Khatib, S. M. *et al.* 2017 AHA/ACC/HRS guideline for management of patients with ventricular arrhythmias and the prevention of sudden cardiac death: a report of the American College of Cardiology/American Heart Association Task Force on Clinical Practice Guidelines and the Hea. *J. Am. Coll. Cardiol.* **72**, e91–e220 (2018).

76. Lei, M., Wu, L., Terrar, D. A. & Huang, C. L. H. Modernized classification of cardiac antiarrhythmic drugs. *Circulation* **138**, 1879–1896 (2018).

77. Huang, C. L. H., Wu, L., Jeevaratnam, K. & Lei, M. Update on antiarrhythmic drug pharmacology. *J. Cardiovasc. Electrophysiol.* **31**, 579–592 (2020).

78. Crotti, L., Celano, G., Dagradi, F. & Schwartz, P. J. Congenital long QT syndrome. *Orphanet J. Rare Dis.* **3**, 18 (2008).

79. Tester, D. J. & Ackerman, M. J. Genetics of Long QT Syndrome. *Methodist Debakey Cardiovasc. J.* **10**, 29–33 (2014).

80. El-Battrawy, I. *et al.* Long-term follow-up of implantable cardioverter-defibrillators in Short QT syndrome. *Clin. Res. Cardiol.* **108**, 1140–1146 (2019).

81. Iyer, M. K. *et al.* The landscape of long noncoding RNAs in the human transcriptome.

Nat. Genet. **47**, 199–208 (2015).

82. Human Genome Sequencing Consortium. Finishing the euchromatic sequence of the human genome. *Nature* **431**, 931–945 (2004).
83. Venter, J. C. *et al.* The sequence of the human genome. *Science* **291**, 1–38 (2001).
84. Hon, C.-C. *et al.* An atlas of human long non-coding RNAs with accurate 5′ ends. *Nature* **543**, 199–204 (2017).
85. Bartel, D. P. Metazoan MicroRNAs. *Cell* **173**, 20–51 (2018).
86. Bartel, D. P. MicroRNAs: Target recognition and regulatory functions. *Cell* **136**, 215–233 (2009).
87. Bartel, D. P. MicroRNAs: Genomics, biogenesis, mechanism, and function. *Cell* **116**, 281–297 (2004).
88. Lee, R. C., Feinbaum, R. L. & Ambros, V. The C. elegans heterochronic gene lin-4 encodes small RNAs with antisense complementarity to lin-14. *Cell* **75**, 843–854 (1993).
89. Wightman, B., Ha, I. & Ruvkun, G. Posttranscriptional regulation of the heterochronic gene lin-14 by lin-4 mediates temporal pattern formation in C. elegans. *Cell* **75**, 855–862 (1993).
90. Reinhart, B. J. *et al.* The 21-nucleotide let-7 RNA regulates developmental timing in Caenorhabditis elegans. *Nature* **403**, 901–906 (2000).
91. Pasquinelli, A. E. *et al.* Conservation of the sequence and temporal expression of let-7 heterochronic regulatory RNA. *Nature* **408**, 86–89 (2000).
92. Lagos-Quintana, M., Rauhut, R., Lendeckel, W. & Tuschl, T. Identification of novel genes coding for small expressed RNAs. *Science* **294**, 853–858 (2001).
93. Lau, N. C. An abundant class of tiny RNAs with probable regulatory roles in Caenorhabditis elegans. *Science* **294**, 858–862 (2001).
94. Lee, R. C. An extensive class of small RNAs in Caenorhabditis elegans. *Science* **294**, 862–864 (2001).
95. Hinkel, R. *et al.* AntimiR-21 prevents myocardial dysfunction in a pig model of ischemia/reperfusion injury. *J. Am. Coll. Cardiol.* **75**, 1788–1800 (2020).
96. Sassi, Y. *et al.* Cardiac myocyte miR-29 promotes pathological remodeling of the heart by activating Wnt signaling. *Nat. Commun.* **8**, (2017).
97. Hullinger, T. G. *et al.* Inhibition of miR-15 protects against cardiac ischemic injury. *Circ. Res.* **110**, 71–81 (2012).
98. Lu, Y. *et al.* MicroRNA-328 contributes to adverse electrical remodeling in atrial fibrillation. *Circulation* **122**, 2378–2387 (2010).
99. Eding, J. E. C. *et al.* The efficacy of cardiac anti-miR-208a therapy is stress dependent. *Mol. Ther.* **25**, 694–704 (2017).
100. Zhang, Y. *et al.* Microrna profiling of atrial fibrillation in canines: miR-206 modulates intrinsic cardiac autonomic nerve remodeling by regulating SOD1. *PLoS One* **10**, e0122674 (2015).
101. Huang, C. K., Kafert-Kasting, S. & Thum, T. Preclinical and clinical development of noncoding rna therapeutics for cardiovascular disease. *Circ. Res.* 663–678 (2020) doi:10.1161/CIRCRESAHA.119.315856.
102. Baskerville, S. & Bartel, D. P. Microarray profiling of microRNAs reveals frequent coexpression with neighboring miRNAs and host genes. *Rna* **11**, 241–247 (2005).
103. CAI, X. Human microRNAs are processed from capped, polyadenylated transcripts that

can also function as mRNAs. *RNA* **10**, 1957–1966 (2004).

104. Lee, Y. *et al.* MicroRNA genes are transcribed by RNA polymerase II. *EMBO J.* **23**, 4051–4060 (2004).

105. Lee, Y. *et al.* The nuclear RNase III Drosha initiates microRNA processing. *Nature* **425**, 415–419 (2003).

106. Lee, Y. MicroRNA maturation: stepwise processing and subcellular localization. *EMBO J.* **21**, 4663–4670 (2002).

107. Lund, E. Nuclear export of microRNA precursors. *Science* **303**, 95–98 (2004).

108. Yi, R. Exportin-5 mediates the nuclear export of pre-microRNAs and short hairpin RNAs. *Genes Dev.* **17**, 3011–3016 (2003).

109. Grishok, A. *et al.* Genes and mechanisms related to RNA interference regulate expression of the small temporal RNAs that control C. elegans developmental timing. *Cell* **106**, 23–34 (2001).

110. Kawamata, T. & Tomari, Y. Making RISC. *Trends Biochem. Sci.* **35**, 368–376 (2010).

111. Hammond, S. M. An overview of microRNAs. *Adv. Drug Deliv. Rev.* **87**, 3–14 (2015).

112. Martinez, J., Patkaniowska, A., Urlaub, H., Lührmann, R. & Tuschl, T. Single-stranded antisense siRNAs guide target RNA cleavage in RNAi. *Cell* **110**, 563–574 (2002).

113. Agarwal, V., Bell, G. W., Nam, J.-W. & Bartel, D. P. Predicting effective microRNA target sites in mammalian mRNAs. *Elife* **4**, (2015).

114. Agarwal, V., Subtelny, A. O., Thiru, P., Ulitsky, I. & Bartel, D. P. Predicting microRNA targeting efficacy in Drosophila. *Genome Biol.* **19**, 152 (2018).

115. Bobbin, M. L. & Rossi, J. J. RNA interference (RNAi)-based therapeutics: delivering on the promise? *Annu. Rev. Pharmacol. Toxicol.* **56**, 103–122 (2016).

116. Jonas, S. & Izaurralde, E. Towards a molecular understanding of microRNA-mediated gene silencing. *Nat. Rev. Genet.* **16**, 421–433 (2015).

117. Filipowicz, W., Bhattacharyya, S. N. & Sonenberg, N. Mechanisms of post-transcriptional regulation by microRNAs: are the answers in sight? *Nat. Rev. Genet.* **9**, 102–114 (2008).

118. Friedman, R. C., Farh, K. K. H., Burge, C. B. & Bartel, D. P. Most mammalian mRNAs are conserved targets of microRNAs. *Genome Res.* **19**, 92–105 (2009).

119. Bosson, A. D., Zamudio, J. R. & Sharp, P. A. Endogenous miRNA and target concentrations determine susceptibility to potential ceRNA competition. *Mol. Cell* **56**, 347–359 (2014).

120. Denzler, R. *et al.* Impact of microRNA levels, target-site complementarity, and cooperativity on competing endogenous RNA-regulated gene expression. *Mol. Cell* **64**, 565–579 (2016).

121. Denzler, R., Agarwal, V., Stefano, J., Bartel, D. P. & Stoffel, M. Assessing the ceRNA Hypothesis with quantitative measurements of mirna and target abundance. *Mol. Cell* **54**, 766–776 (2014).

122. Khorshid, M., Hausser, J., Zavolan, M. & van Nimwegen, E. A biophysical miRNA-mRNA interaction model infers canonical and noncanonical targets. *Nat. Methods* **10**, 253–255 (2013).

123. Wessels, H.-H. *et al.* Global identification of functional microRNA-mRNA interactions in Drosophila. *Nat. Commun.* **10**, 1626 (2019).

124. Werfel, S., Leierseder, S., Ruprecht, B., Kuster, B. & Engelhardt, S. Preferential microRNA targeting revealed by in vivo competitive binding and differential Argonaute

immunoprecipitation. *Nucleic Acids Res.* **45**, 10218–10228 (2017).

125. Huang, Y. *et al.* A study of miRNAs targets prediction and experimental validation. *Protein Cell* **1**, 979–986 (2010).
126. Lennox, K. a & Behlke, M. a. Chemical modification and design of anti-miRNA oligonucleotides. *Gene Ther.* **18**, 1111–1120 (2011).
127. Esau, C. C. Inhibition of microRNA with antisense oligonucleotides. *Methods* **44**, 55–60 (2008).
128. Ebert, M. S. & Sharp, P. A. Emerging roles for natural microRNA sponges. *Curr. Biol.* **20**, R858–R861 (2010).
129. Stenvang, J., Petri, A., Lindow, M., Obad, S. & Kauppinen, S. Inhibition of microRNA function by antimiR oligonucleotides. *Silence* **3**, 1 (2012).
130. Davis, S. Improved targeting of miRNA with antisense oligonucleotides. *Nucleic Acids Res.* **34**, 2294–2304 (2006).
131. Thorsen, S. B., Obad, S., Jensen, N. F., Stenvang, J. & Kauppinen, S. The therapeutic potential of microRNAs in cancer. *Cancer J.* **18**, 275–284 (2012).
132. van Rooij, E. & Kauppinen, S. Development of microRNA therapeutics is coming of age. *EMBO Mol. Med.* **6**, 851–64 (2014).
133. Lu, D. & Thum, T. RNA-based diagnostic and therapeutic strategies for cardiovascular disease. *Nat. Rev. Cardiol.* **16**, 661–674 (2019).
134. Romaine, S. P. R., Tomaszewski, M., Condorelli, G. & Samani, N. J. MicroRNAs in cardiovascular disease: an introduction for clinicians. *Heart* **101**, 921–928 (2015).
135. Pang, J. K. S., Phua, Q. H. & Soh, B. S. Applications of miRNAs in cardiac development, disease progression and regeneration. *Stem Cell Res. Ther.* **10**, 1–11 (2019).
136. Colpaert, R. M. W. & Calore, M. MicroRNAs in cardiac diseases. *Cells* **8**, 737 (2019).
137. Samanta, S. *et al.* MicroRNA: A new therapeutic strategy for cardiovascular diseases. *Trends Cardiovasc. Med.* (2016) doi:10.1016/j.tcm.2016.02.004.
138. Siasos, G. *et al.* MicroRNAs in cardiovascular disease. *Hell. J. Cardiol.* **61**, 165–173 (2020).
139. Zhou, S. S. *et al.* MiRNAS in cardiovascular diseases: Potential biomarkers, therapeutic targets and challenges review-article. *Acta Pharmacol. Sin.* **39**, 1073–1084 (2018).
140. Lian, J. *et al.* miRNAs Regulate hERG. *J. Cardiovasc. Electrophysiol.* **27**, 1472–1482 (2016).
141. Luo, X., Zhang, H., Xiao, J. & Wang, Z. Regulation of human cardiac Ion channel genes by MicroRNAs: Theoretical perspective and pathophysiological implications. *Cell. Physiol. Biochem.* **25**, 571–586 (2010).
142. Luo, X., Yang, B. & Nattel, S. MicroRNAs and atrial fibrillation: mechanisms and translational potential. *Nat. Rev. Cardiol.* **12**, 80–90 (2015).
143. Nattel, S. Molecular and cellular mechanisms of atrial fibrosis in atrial fibrillation. *JACC Clin. Electrophysiol.* **3**, 425–435 (2017).
144. Jiang, S. *et al.* The integrative regulatory network of circRNA, microRNA, and mRNA in atrial fibrillation. *Front. Genet.* **10**, (2019).
145. Clauss, S., Sinner, M. F., Kääb, S. & Wakili, R. The role of microRNAs in antiarrhythmic therapy for atrial fibrillation. *Arrhythmia Electrophysiol. Rev.* **4**, 146 (2015).
146. Dawson, K. *et al.* MicroRNA29: A mechanistic contributor and potential biomarker in atrial fibrillation. *Circulation* **127**, 1466–1475 (2013).

147. Adam, O. *et al.* Role of miR-21 in the pathogenesis of atrial fibrosis. *Basic Res. Cardiol.* **107**, 278 (2012).

148. Morishima, M. *et al.* Atrial fibrillation-mediated upregulation of miR-30d regulates myocardial electrical remodeling of the G-Protein-Gated K(+) Channel, IK.ACh. *Circ J* **80**, 1346–1355 (2016).

149. Girmatsion, Z. *et al.* Changes in microRNA-1 expression and IK1 up-regulation in human atrial fibrillation. *Hear. Rhythm* **6**, 1802–1809 (2009).

150. Kim, G. H. MicroRNA regulation of cardiac conduction and arrhythmias. *Transl. Res.* **161**, 381–392 (2013).

151. Guzzolino, E. & Pitto, L. The pervasive role of microRNAs in arrhythmia: animal models and novel discoveries. *J. Transl. Sci.* **5**, 1–5 (2019).

152. Besser, J. *et al.* MiRNA-1/133a clusters regulate adrenergic control of cardiac repolarization. *PLoS One* **9**, e113449 (2014).

153. Matkovich, S. J. *et al.* MicroRNA-133a protects against myocardial fibrosis and modulates electrical repolarization without affecting hypertrophy in pressure-overloaded adult hearts. *Circ. Res.* **106**, 166–175 (2010).

154. Shan, H. *et al.* Upregulation of microRNA-1 and microRNA-133 contributes to arsenic-induced cardiac electrical remodeling. *Int. J. Cardiol.* **167**, 2798–2805 (2013).

155. Goldoni, D. *et al.* A novel dual-fluorescence strategy for functionally validating microRNA targets in 3′ untranslated regions: regulation of the inward rectifier potassium channel Kir2.1 by miR-212. *Biochem. J.* **448**, 103–113 (2012).

156. Benz, A. *et al.* Mir-19b regulates ventricular action potential duration in zebrafish. *Sci. Rep.* **6**, 36033 (2016).

157. Binas, S. *et al.* miR-221 and -222 target CACNA1C and KCNJ5 leading to altered cardiac ion channel expression and current density. *Cell. Mol. Life Sci.* **77**, 903–918 (2020).

158. MiRbase.org. miRbase: hsa-mir-365b. (2018).

159. RNAcentral.org: hsa-mir-365a precursor. *RNAcentral.org* (2018).

160. Kozomara, A. & Griffiths-Jones, S. MiRBase: Annotating high confidence microRNAs using deep sequencing data. *Nucleic Acids Res.* **42**, 68–73 (2014).

161. GTEx Consortium. Genetic effects on gene expression across human tissues. *Nature* **550**, 204–213 (2017).

162. Smith, S. S., Kessler, C. B., Shenoy, V., Rosen, C. J. & Delany, A. M. IGF-I 3′ untranslated region: strain-specific polymorphisms and motifs regulating IGF-I in osteoblasts. *Endocrinology* **154**, 253–262 (2013).

163. Franceschetti, T., Dole, N. S., Kessler, C. B., Lee, S.-K. & Delany, A. M. Pathway analysis of microRNA expression profile during murine osteoclastogenesis. *PLoS One* **9**, e107262 (2014).

164. Li, G. *et al.* Curcumin improves bone microarchitecture in glucocorticoid-induced secondary osteoporosis mice through the activation of microRNA-365 via regulating MMP-9. *Int. J. Clin. Exp. Pathol.* **8**, 15684–15695 (2015).

165. Xu, D., Gao, Y., Hu, N., Wu, L. & Chen, Q. miR-365 ameliorates dexamethasone-induced suppression of osteogenesis in MC3T3-E1 cells by targeting HDAC4. *Int. J. Mol. Sci.* **18**, 1–10 (2017).

166. Cheleschi, S. *et al.* Hydrostatic pressure regulates MicroRNA expression levels in osteoarthritic chondrocyte cultures via the Wnt/β-catenin pathway. *Int. J. Mol. Sci.* **18**, (2017).

167. Gaita, F. *et al.* Short QT syndrome: pharmacological treatment. *J. Am. Coll. Cardiol.* **43**, 1494–1499 (2004).

168. Guan, Y.-J., Yang, X., Wei, L. & Chen, Q. MiR-365: a mechanosensitive microRNA stimulates chondrocyte differentiation through targeting histone deacetylase 4. *FASEB J.* **25**, 4457–4466 (2011).

169. Mori, M. A. *et al.* Altered miRNA processing disrupts brown/white adipocyte determination and associates with lipodystrophy. *J. Clin. Invest.* **124**, 3339–3351 (2014).

170. Feuermann, Y. *et al.* MiR-193b and miR-365-1 are not required for the development and function of brown fat in the mouse. *RNA Biol.* **10**, 1807–1814 (2013).

171. Vienberg, S., Geiger, J., Madsen, S. & Dalgaard, L. T. MicroRNAs in metabolism. *Acta Physiol.* **219**, 346–361 (2017).

172. Wang, Y. *et al.* MicroRNA - 365 promotes lung carcinogenesis by downregulating the USP33 / SLIT2 / ROBO1 signalling pathway. *Cancer Cell Int.* 1–14 (2018) doi:10.1186/s12935-018-0563-6.

173. Zhou, L. *et al.* HOXA9 inhibits HIF-1α-mediated glycolysis through interacting with CRIP2 to repress cutaneous squamous cell carcinoma development. *Nat. Commun.* **9**, 1–17 (2018).

174. Zhou, L., Gao, R., Wang, Y., Zhou, M. & Ding, Z. Loss of BAX by miR-365 promotes cutaneous squamous cell carcinoma progression by suppressing apoptosis. *Int. J. Mol. Sci.* **18**, (2017).

175. Zhou, M. *et al.* A novel onco-miR-365 induces cutaneous squamous cell carcinoma. *Carcinogenesis* **34**, 1653–1659 (2013).

176. Zhou, M. *et al.* miR-365 promotes Cutaneous Squamous Cell Carcinoma (CSCC) through targeting Nuclear Factor I/B (NFIB). *PLoS One* **9**, (2014).

177. Moss, T. J. *et al.* Genome-wide perturbations by miRNAs map onto functional cellular pathways, identifying regulators of chromatin modifiers. *npj Syst. Biol. Appl.* **1**, 15001 (2015).

178. Tao, J. *et al.* Distinct anti-oncogenic effect of various microRNAs in different mouse models of liver cancer. *Oncotarget* **6**, 6977–6988 (2015).

179. Chen, Z. *et al.* Prognostic significance and anti-proliferation effect of microRNA-365 in hepatocellular carcinoma. *Int. J. Clin. Exp. Pathol.* **8**, 1705–1711 (2015).

180. Li, M. *et al.* MiR-365 induces hepatocellular carcinoma cell apoptosis through targeting Bcl-2. *Exp. Ther. Med.* **13**, 2279–2285 (2017).

181. Wang, Y., Xu, C., Wang, Y. & Zhang, X. MicroRNA-365 inhibits ovarian cancer progression by targeting Wnt5a. *Am. J. Cancer Res.* **7**, 1096–1106 (2017).

182. Seviour, E. G. *et al.* Functional proteomics identifies miRNAs to target a p27/Myc/phospho-Rb signature in breast and ovarian cancer. *Oncogene* **35**, 691–701 (2016).

183. Singh, R. & Saini, N. Downregulation of BCL2 by miRNAs augments drug-induced apoptosis - a combined computational and experimental approach. *J. Cell Sci.* **125**, 1568–1578 (2012).

184. Zhang, J., Zhang, Z., Wang, Q., Xing, X. J. & Zhao, Y. Overexpression of microRNA-365 inhibits breast cancer cell growth and chemo-resistance through GALNT4. *Eur. Rev. Med. Pharmacol. Sci.* **20**, 4710–4718 (2016).

185. Qi, J. *et al.* MiR-365 regulates lung cancer and developmental gene thyroid transcription factor 1. *Cell Cycle* **11**, 177–186 (2012).

186. Bai, J., Zhang, Z., Li, X. & Liu, H. MicroRNA-365 inhibits growth, invasion and metastasis of malignant melanoma by targeting NRP1 expression. *Cancer Biomark.* **15**, 599–608 (2015).

187. Guo, S. L. *et al.* Akt-p53-miR-365-cyclin D1/cdc25A axis contributes to gastric tumorigenesis induced by PTEN deficiency. *Nat. Commun.* **4**, 1–11 (2013).

188. Lin, B. *et al.* MiR-365 participates in coronary atherosclerosis through regulating IL-6. *Eur. Rev. Med. Pharmacol. Sci.* **20**, 5186–5192 (2016).

189. Song, Q., Li, H., Shao, H., Li, C. & Lu, X. MicroRNA-365 in macrophages regulates Mycobacterium tuberculosis-induced active pulmonary tuberculosis via interleukin-6. *Int. J. Clin. Exp. Med.* **8**, 15458–15465 (2015).

190. Pan, Z. *et al.* Hydroxymethylation of microRNA-365-3p regulates nociceptive behaviors via Kcnh2. *J. Neurosci.* **36**, 2769–2781 (2016).

191. Jentzsch, C. *et al.* A phenotypic screen to identify hypertrophy-modulating microRNAs in primary cardiomyocytes. *J. Mol. Cell. Cardiol.* **52**, 13–20 (2012).

192. Wu, H., Wang, Y., Wang, X., Li, R. & Yin, D. MicroRNA-365 accelerates cardiac hypertrophy by inhibiting autophagy via the modulation of Skp2 expression. *Biochem. Biophys. Res. Commun.* **484**, 304–310 (2017).

193. Kuehl, U. *et al.* Differential cardiac microRNA expression predicts the clinical course in human enterovirus cardiomyopathy. *Circ. Hear. Fail.* **8**, 605–618 (2015).

194. Akat, K. M. *et al.* Comparative RNA-sequencing analysis of myocardial and circulating small RNAs in human heart failure and their utility as biomarkers. *Proc. Natl. Acad. Sci. U. S. A.* **111**, 11151–11156 (2014).

195. Roden, D. M. & George, A. L. The cardiac ion channels: Relevance to management of arrhythmias. *Annu. Rev. Med.* **47**, 135–148 (1996).

196. Jin, H. *et al.* Mechanoelectrical remodeling and arrhythmias during progression of hypertrophy. *FASEB J.* **24**, 451–463 (2010).

197. Wang, Y. *et al.* β2 adrenergic receptor activation governs cardiac repolarization and arrhythmogenesis in a guinea pig model of heart failure. *Sci. Rep.* **5**, 7681 (2015).

198. Pogwizd, S. M., Qi, M., Yuan, W., Samarel, A. M. & Bers, D. M. Upregulation of Na + /Ca 2+ Exchanger expression and function in an arrhythmogenic rabbit model of heart failure. *Circ. Res.* **85**, 1009–1019 (1999).

199. Clauss, S. *et al.* Animal models of arrhythmia: classic electrophysiology to genetically modified large animals. *Nat. Rev. Cardiol.* **16**, 457–475 (2019).

200. CURTIS, M., MACLEOD, B. & WALKER, M. Models for the study of arrhythmias in myocardial ischaemia and infarction: the use of the rat. *J. Mol. Cell. Cardiol.* **19**, 399–419 (1987).

201. Hundahl, L. A., Tfelt-Hansen, J. & Jespersen, T. Rat models of ventricular fibrillation following acute myocardial infarction. *J. Cardiovasc. Pharmacol. Ther.* **22**, 514–528 (2017).

202. Lacroix, D. *et al.* Repolarization abnormalities and their arrhythmogenic consequences in porcine tachycardia-induced cardiomyopathy. *Cardiovasc. Res.* **54**, 42–50 (2002).

203. Choy, L., Yeo, J. M., Tse, V., Chan, S. P. & Tse, G. Cardiac disease and arrhythmogenesis: Mechanistic insights from mouse models. *IJC Hear. Vasc.* **12**, 1–10 (2016).

204. Huang, C. L. H. Murine electrophysiological models of cardiac arrhythmogenesis. *Physiol. Rev.* **97**, 283–409 (2017).

205. Sallam, K., Kodo, K. & Wu, J. C. Modeling inherited cardiac disorders. *Circ. J.* **78**, 784–

794 (2014).

206. Sallam, K., Li, Y., Sager, P. T., Houser, S. R. & Wu, J. C. Tissue and animal models of sudden cardiac death. *Circ Res* **116**, 1989–2004 (2015).

207. Nerbonne, J. M. Studying Cardiac arrhythmias in the mouse—a reasonable model for probing mechanisms? *Trends Cardiovasc. Med.* **14**, 83–93 (2004).

208. Baczkó, I., Hornyik, T., Brunner, M., Koren, G. & Odening, K. E. Transgenic rabbit models in proarrhythmia research. *Front. Pharmacol.* **11**, 1–18 (2020).

209. Odening, K. E., Baczko, I. & Brunner, M. Animals in cardiovascular research: important role of rabbit models in cardiac electrophysiology. *Eur. Heart J.* **41**, 2036–2036 (2020).

210. Jost, N. *et al.* Ionic mechanisms limiting cardiac repolarization reserve in humans compared to dogs. *J. Physiol.* **591**, 4189–4206 (2013).

211. Takahashi, K. *et al.* Induction of pluripotent stem cells from adult human fibroblasts by defined factors. *Cell* **131**, 861–872 (2007).

212. Liu, G., David, B. T., Trawczynski, M. & Fessler, R. G. Advances in pluripotent stem cells: history, mechanisms, technologies, and applications. *Stem Cell Rev. Reports* **16**, 3–32 (2020).

213. Machiraju, P. & Greenway, S. C. Current methods for the maturation of induced pluripotent stem cell-derived cardiomyocytes. *World J. Stem Cells* **11**, 33–43 (2019).

214. Burridge, P. *et al.* Chemically defined and small molecule-based generation of human cardiomyocytes. *Nat. Methods* **58**, 855–860 (2014).

215. Cyganek, L. *et al.* Deep phenotyping of human induced pluripotent stem cell–derived atrial and ventricular cardiomyocytes. *JCI Insight* **3**, (2018).

216. Karakikes, I., Ameen, M., Termglinchan, V. & Wu, J. C. Human induced pluripotent stem cell-derived cardiomyocytes: insights into molecular, cellular, and functional phenotypes. *Circ. Res.* **117**, 80–88 (2015).

217. Heuvel, N. H. L. Van Den, Veen, T. A. B. Van, Lim, B. & Jonsson, M. K. B. Lessons from the heart : Mirroring electrophysiological characteristics during cardiac development to in vitro differentiation of stem cell derived cardiomyocytes. *J. Mol. Cell. Cardiol.* **67**, 12–25 (2013).

218. Chen, Z. *et al.* Subtype-specific promoter-driven action potential imaging for precise disease modelling and drug testing in hiPSC-derived cardiomyocytes. *Eur. Heart J.* **38**, 292-301 (2016).

219. Koivumäki, J. T. *et al.* Structural immaturity of human iPSC-derived cardiomyocytes: In silico investigation of effects on function and disease modeling. *Front. Physiol.* **9**, 1–17 (2018).

220. Tranquillo, J. & Sunkara, A. Can we trust the transgenic mouse? insights from computer simulations. in *Functional imaging and modeling of the heart* 210–219 (Springer Berlin Heidelberg, 2007).

221. Moretti, A. *et al.* Patient-specific induced pluripotent stem-cell models for Long-QT syndrome. *N. Engl. J. Med.* **363**, 1397–1409 (2010).

222. Yazawa, M. *et al.* Using induced pluripotent stem cells to investigate cardiac phenotypes in Timothy syndrome. *Nature* **471**, 230–236 (2011).

223. Liang, P. *et al.* Patient-specific and genome-edited induced pluripotent stem cell–derived cardiomyocytes elucidate single-cell phenotype of Brugada syndrome. *J. Am. Coll. Cardiol.* **68**, 2086–2096 (2016).

224. Bellin, M. *et al.* Isogenic human pluripotent stem cell pairs reveal the role of a KCNH2 mutation in long-QT syndrome. *EMBO J.* **32**, 3161–3175 (2013).

225. El-Battrawy, I. *et al.* Modeling Short QT syndrome using human-induced pluripotent stem cell-derived cardiomyocytes. *J. Am. Heart Assoc.* **7**, (2018).

226. Yamamoto, W. *et al.* Electrophysiological characteristics of human iPSC-derived cardiomyocytes for the assessment of drug-induced proarrhythmic potential. *PLoS One* **11**, 1–14 (2016).

227. Navarrete, E. G. *et al.* Screening drug-induced arrhythmia events using human induced pluripotent stem cell-derived cardiomyocytes and low-impedance microelectrode arrays. *Circulation* **128**, (2013).

228. Martin, U. *Engineering and Application of Pluripotent Stem Cells*. vol. 163, 169-186 (Springer International Publishing, 2018).

229. Li, J. *et al.* Human pluripotent stem cell-derived cardiac tissue-like constructs for repairing the infarcted myocardium. *Stem Cell Reports* **9**, 1546–1559 (2017).

230. Fischer, C. *et al.* Long-term functional and structural preservation of precision-cut human myocardium under continuous electromechanical stimulation in vitro. *Nat. Commun.* **10**, 1–12 (2019).

231. Brandenburger, M. *et al.* Organotypic slice culture from human adult ventricular myocardium. *Cardiovasc. Res.* **93**, 50–59 (2012).

232. Watson, S. A. *et al.* Preparation of viable adult ventricular myocardial slices from large and small mammals. *Nat. Protoc.* **12**, 2623–2639 (2017).

233. Pitoulis, F. G., Watson, S. A., Perbellini, F. & Terracciano, C. M. Myocardial slices come to age: an intermediate complexity in vitro cardiac model for translational research. *Cardiovasc. Res.* **116**, 1275–1287 (2020).

234. Laurila, E., Ahola, A., Hyttinen, J. & Aalto-Setälä, K. Methods for in vitro functional analysis of iPSC derived cardiomyocytes — Special focus on analyzing the mechanical beating behavior. *Biochim. Biophys. Acta - Mol. Cell Res.* **1863**, 1864–1872 (2016).

235. Zhu, H. *et al.* Two dimensional electrophysiological characterization of human pluripotent stem cell-derived cardiomyocyte system. *Sci. Rep.* **7**, 43210 (2017).

236. Koopman, C. D., Zimmermann, W. H., Knöpfel, T. & de Boer, T. P. Cardiac optogenetics: using light to monitor cardiac physiology. *Basic Res. Cardiol.* **112**, (2017).

237. St-Pierre, F. *et al.* High-fidelity optical reporting of neuronal electrical activity with an ultrafast fluorescent voltage sensor. *Nat. Neurosci.* **17**, 884–889 (2014).

238. Kaestner, L. *et al.* Genetically encoded voltage indicators in circulation research. *Int. J. Mol. Sci.* **16**, 21626–21642 (2015).

239. St-Pierre, F., Chavarha, M. & Lin, M. Z. Designs and sensing mechanisms of genetically encoded fluorescent voltage indicators. *Curr. Opin. Chem. Biol.* **27**, 31–38 (2015).

240. Gramlich, M. *et al.* Antisense-mediated exon skipping: a therapeutic strategy for titin-based dilated cardiomyopathy. *EMBO Mol. Med.* **7**, 562–576 (2015).

241. Bindea, G. *et al.* ClueGO: a Cytoscape plug-in to decipher functionally grouped gene ontology and pathway annotation networks. *Bioinformatics* **25**, 1091–1093 (2009).

242. Shannon, P. Cytoscape: A software environment for integrated models of biomolecular interaction networks. *Genome Res.* **13**, 2498–2504 (2003).

243. Love, M. I., Huber, W. & Anders, S. Moderated estimation of fold change and dispersion for RNA-seq data with DESeq2. *Genome Biol.* **15**, 550 (2014).

244. Afgan, E. *et al.* The Galaxy platform for accessible, reproducible and collaborative biomedical analyses: 2018 update. *Nucleic Acids Res.* **46**, W537–W544 (2018).

245. Friedländer, M. R., Mackowiak, S. D., Li, N., Chen, W. & Rajewsky, N. miRDeep2

accurately identifies known and hundreds of novel microRNA genes in seven animal clades. *Nucleic Acids Res.* **40**, 37–52 (2012).

246. Stuart, T. *et al.* Comprehensive integration of single-cell data. *Cell* **177**, 1888-1902.e21 (2019).

247. Butler, A., Hoffman, P., Smibert, P., Papalexi, E. & Satija, R. Integrating single-cell transcriptomic data across different conditions, technologies, and species. *Nat. Biotechnol.* **36**, 411–420 (2018).

248. Dobin, A. *et al.* STAR: ultrafast universal RNA-seq aligner. *Bioinformatics* **29**, 15–21 (2013).

249. Pertea, M., Kim, D., Pertea, G. M., Leek, J. T. & Salzberg, S. L. Transcript-level expression analysis of RNA-seq experiments with HISAT, StringTie and Ballgown. *Nat. Protoc.* **11**, 1650–1667 (2016).

250. Burridge, P. W., Holmström, A. & Wu, J. C. Chemically defined culture and cardiomyocyte differentiation of human pluripotent stem cells. *Curr. Protoc. Hum. Genet.* 21.3.1-21.3.15 (2015).

251. Lam, A. J. *et al.* Improving FRET dynamic range with bright green and red fluorescent proteins. *Nat. Methods* **9**, 1005–12 (2012).

252. Hafemeister, C. & Satija, R. Normalization and variance stabilization of single-cell RNA-seq data using regularized negative binomial regression. *Genome Biol.* **20**, 296 (2019).

253. Kuleshov, M. V. *et al.* Enrichr: a comprehensive gene set enrichment analysis web server 2016 update. *Nucleic Acids Res.* **44**, W90–W97 (2016).

254. Subramanian, A. *et al.* Gene set enrichment analysis: A knowledge-based approach for interpreting genome-wide expression profiles. *Proc. Natl. Acad. Sci.* **102**, 15545–15550 (2005).

255. Cyganek, L. *et al.* Deep phenotyping of human induced pluripotent stem cell–derived atrial and ventricular cardiomyocytes. *JCI Insight* **3**, e99941 (2018).

256. Esfandyari, D. *et al.* MicroRNA-365 regulates human cardiac action potential duration. *Nat. Commun.* **13**, 220 (2022).

257. Yang, K. C. *et al.* Deep RNA sequencing reveals dynamic regulation of myocardial noncoding RNAs in failing human heart and remodeling with mechanical circulatory support. *Circulation* **129**, 1009–1021 (2014).

258. The UniProt Consortium. UniProt: a worldwide hub of protein knowledge. *Nucleic Acids Res.* **47**, D506–D515 (2019).

259. Thomson, D. W., Bracken, C. P., Szubert, J. M. & Goodall, G. J. On measuring miRNAs after transient transfection of mimics or antisense inhibitors. *PLoS One* **8**, e55214 (2013).

260. Lam, A. J. *et al.* Improving FRET dynamic range with bright green and red fluorescent proteins. *Nat. Methods* **9**, 1005–1012 (2012).

261. Li, G. *et al.* Transcriptomic profiling maps anatomically patterned subpopulations among single embryonic cardiac cells. *Dev. Cell* **39**, 491–507 (2016).

262. Sahara, M. *et al.* Population and single-cell analysis of human cardiogenesis reveals unique LGR5 ventricular progenitors in embryonic outflow tract. *Dev. Cell* **48**, 475–490 (2019).

263. Bedada, F. B., Wheelwright, M. & Metzger, J. M. Maturation status of sarcomere structure and function in human iPSC-derived cardiac myocytes. *Biochim. Biophys. Acta - Mol. Cell Res.* **1863**, 1829–1838 (2016).

264. Linderman, G. C. *et al.* Zero-preserving imputation of single-cell RNA-seq data. *Nat.*

Commun. **13**, 192 (2022).

265. El-Battrawy, I. *et al.* Modeling short QT syndrome using human-induced pluripotent stem cell–derived cardiomyocytes. *J. Am. Heart Assoc.* **7**, e007394 (2018).
266. Becker, W. R. *et al.* High-throughput analysis reveals rules for target rna binding and cleavage by AGO2. *Mol. Cell* **75**, 741-755.e11 (2019).
267. Litviňuková, M. *et al.* Cells of the adult human heart. *Nature* **588**, 466–472 (2020).
268. Tucker, N. R. *et al.* Transcriptional and cellular diversity of the human heart. *Circulation* **142**, 466–482 (2020).
269. Donovan, M. K. R., D'Antonio-Chronowska, A., D'Antonio, M. & Frazer, K. A. Cellular deconvolution of GTEx tissues powers discovery of disease and cell-type associated regulatory variants. *Nat. Commun.* **11**, 1–14 (2020).
270. Hua, X. *et al.* Multi-level transcriptome sequencing identifies COL1A1 as a candidate marker in human heart failure progression. *BMC Med.* **18**, 1–16 (2020).
271. Liao, C., Gui, Y., Guo, Y. & Xu, D. The regulatory function of microRNA-1 in arrhythmias. *Mol. Biosyst.* **12**, 328–333 (2016).
272. Luo, X. *et al.* MicroRNA-26 governs profibrillatory inward-rectifier potassium current changes in atrial fibrillation. *J. Clin. Invest.* **123**, 1939–1951 (2013).
273. Heidersbach, A. *et al.* microRNA-1 regulates sarcomere formation and suppresses smooth muscle gene expression in the mammalian heart. *Elife* **2**, e01323 (2013).
274. Spengler, R. M. *et al.* Elucidation of transcriptome-wide microRNA binding sites in human cardiac tissues by Ago2 HITS-CLIP. *Nucleic Acids Res.* **44**, 7120–7131 (2016).
275. Garcia, D. M. *et al.* Weak seed-pairing stability and high target-site abundance decrease the proficiency of lsy-6 and other microRNAs. *Nat. Struct. Mol. Biol.* **18**, 1139–1146 (2011).
276. Lang, S. E. & Westfall, M. V. Gene transfer into cardiac myocytes. *Methods in Mol Biol.*, **1299**, 177–190 (2015). doi:10.1007/978-1-4939-2572-8_15.
277. Khvorova, A. & Watts, J. K. The chemical evolution of oligonucleotide therapies of clinical utility. *Nat. Biotechnol.* **35**, 238–248 (2017).
278. Colatsky, T. *et al.* The comprehensive in vitro proarrhythmia assay (CiPA) initiative — update on progress. *J. Pharmacol. Toxicol. Methods* **81**, 15–20 (2016).
279. Casini, S., Verkerk, A. O. & Remme, C. A. Human ipsc-derived cardiomyocytes for investigation of disease mechanisms and therapeutic strategies in inherited arrhythmia syndromes: strengths and limitations. *Cardiovasc. Drugs Ther.* **31**, 325–344 (2017).
280. Pan, Z. *et al.* Hydroxymethylation of microRNA-365-3p regulates nociceptive behaviors via Kcnh2. *J. Neurosci.* **36**, 2769–2781 (2016).
281. Lemoine, M. D. *et al.* Human induced pluripotent stem cell-derived engineered heart tissue as a sensitive test system for QT prolongation and arrhythmic triggers. *Circ. Arrhythmia Electrophysiol.* **11**, 1–15 (2018).
282. Denning, C. *et al.* Cardiomyocytes from human pluripotent stem cells: From laboratory curiosity to industrial biomedical platform. *Biochim. Biophys. Acta - Mol. Cell Res.* **1863**, 1728–1748 (2016).
283. Feyen, D. A. M. *et al.* Metabolic maturation media improve physiological function of human iPSC-derived cardiomyocytes. *Cell Rep.* **32**, (2020).
284. Abulaiti, M. *et al.* Establishment of a heart-on-a-chip microdevice based on human iPS cells for the evaluation of human heart tissue function. *Sci. Rep.* **10**, 1–12 (2020).
285. Song, Y., Xu, Z. & Wang, F. Genetically encoded reporter genes for microRNA imaging

in living cells and animals. *Mol. Ther. - Nucleic Acids* **21**, 555–567 (2020).

286. Yamada, S. & Nomura, S. Review of single-cell RNA sequencing in the heart. *Int. J. Mol. Sci.* **21**, 1–15 (2020).

287. Chen, G., Ning, B. & Shi, T. Single-cell RNA-seq technologies and related computational data analysis. *Front. Genet.* **10**, 1–13 (2019).

288. Tyan, L. *et al.* Long QT syndrome caveolin-3 mutations differentially modulate K v 4 and Ca v 1.2 channels to contribute to action potential prolongation. *J. Physiol.* **597**, 1531–1551 (2019).

289. Giudicessi, J. R., Wilde, A. A. M. & Ackerman, M. J. The genetic architecture of long QT syndrome: A critical reappraisal. *Trends Cardiovasc. Med.* **28**, 453–464 (2018).

290. Varró, A. & Baczkó, I. Cardiac ventricular repolarization reserve: a principle for understanding drug-related proarrhythmic risk. *Br. J. Pharmacol.* **164**, 14–36 (2011).

291. Moretti, A. *et al.* Somatic gene editing ameliorates skeletal and cardiac muscle failure in pig and human models of Duchenne muscular dystrophy. *Nat. Med.* **26**, 207–214 (2020).

292. Kang, C. *et al.* Human organotypic cultured cardiac slices : new platform for high throughput preclinical human trials. Sci. Rep. **6** 1–13 (2016).

293. Schneider, C. *et al.* Primate heart regeneration via migration and fibroblast repulsion by human heart progenitors. *bioRxiv* 1–46 (2020).

294. Thomas, R. C. *et al.* A Myocardial slice culture model reveals alpha-1a-adrenergic receptor signaling in the human heart. *JACC Basic to Transl. Sci.* **1**, 155–167 (2016).

295. Odening, K. E. *et al.* Transgenic short-QT syndrome 1 rabbits mimic the human disease phenotype with QT/action potential duration shortening in the atria and ventricles and increased ventricular tachycardia/ventricular fibrillation inducibility. *Eur. Heart J.* **40**, 842–853 (2019).

296. Perleberg, C., Kind, A. & Schnieke, A. Genetically engineered pigs as models for human disease. *DMM Dis. Model. Mech.* **11**, (2018).

297. Brendorp, B., Pedersen, O., Torp-Pedersen, C., Sahebzadah, N. & Kober, L. A benefit-risk assessment of class III antiarrhythmic agents. *Drug Saf.* **25**, 847–865 (2002).

298. Aguet, F. *et al.* Genetic effects on gene expression across human tissues. *Nature* **550**, 204–213 (2017).

299. Mo, J.-L. *et al.* MicroRNA-365 modulates astrocyte conversion into neuron in adult rat brain after stroke by targeting Pax6. *Glia* **66**, 1346–1362 (2018).

300. Wang, X. *et al.* Up-regulation of miR-365 promotes the apoptosis and restrains proliferation of synoviocytes through downregulation of IGF1 and the inactivation of the PI3K/AKT/mTOR pathway in mice with rheumatoid arthritis. *Int. Immunopharmacol.* **79**, 106067 (2020).

301. Lip, G. Y. H. *et al.* European Heart Rhythm Association/Heart Failure Association joint consensus document on arrhythmias in heart failure, endorsed by the Heart Rhythm Society and the Asia Pacific Heart Rhythm Society. *Eur. J. Heart Fail.* **17**, 848–874 (2015).

302. Donahue, J. K. Current state of the art for cardiac arrhythmia gene therapy. *Pharmacol. Ther.* **176**, 60–65 (2017).

303. Mellis, D. & Caporali, A. MicroRNA-based therapeutics in cardiovascular disease: screening and delivery to the target. *Biochem. Soc. Trans.* **46**, 11–21 (2018).

304. Zhang, Y., Du, W. & Yang, B. Long non-coding RNAs as new regulators of cardiac electrophysiology and arrhythmias: Molecular mechanisms, therapeutic implications

and challenges. *Pharmacol. Ther.* **203**, 107389 (2019).

305. Long, Q. *et al.* Long noncoding RNA Kcna2 antisense RNA contributes to ventricular arrhythmias via silencing Kcna2 in rats with congestive heart failure. *J. Am. Heart Assoc.* **6**, (2017).

306. Shen, C. *et al.* YY1-induced upregulation of lncRNA KCNQ1OT1 regulates angiotensin II-induced atrial fibrillation by modulating miR-384b/CACNA1C axis. *Biochem. Biophys. Res. Commun.* **505**, 134–140 (2018).

307. Zhang, H. *et al.* Long noncoding RNA-mediated intrachromosomal interactions promote imprinting at the Kcnq1 locus. *J. Cell Biol.* **204**, 61–75 (2014).

8 Acknowledgments

At this point, I would like to warmly thank all the people who made this journey possible:

first of all, I'm truly grateful to my supervisor Prof. Stefan Engelhardt, because of whom I was able to step into a new chapter and work in such an excellent team. Thanks for your support throughout my PhD, and for believing in me and letting me challenge and raise my limits.

Special thanks to my second supervisor Prof. Angelika Schnieke, an inspirational woman in science, who agreed to be a part of my thesis committee.

I'm thankful to all my collaborators, especially Prof. Alessandra Moretti, for her support throughout the project and for numerous iPS cell lines; Prof. Andreas Dendorfer, for introducing the cardiac slice technology to us and for his enthusiasm for science; Prof. Stefanie Fenske and Konstantin Hennis for fruitful collaboration during the revision of my manuscript.

Thanks to all my friends and colleagues at IPT: Petros for being behind me, literally, for the past 6 years; Gheo, who started as my master students and grew to be my fellow PhD candidate and my partner in crime to find a treatment for arrhythmia; Anne, for sharing the enthusiasm in fantasy novels and transcriptomics; Deepak for his friendship as well as the mentorship of this work; Giulia for her bright personality and Italian cuisine experiences; Yassine, for the short but nice time he was my mentor; and Reyhaneh for increasing the team-Iran in the lab from 1 to 2. To Ulla for constant support with the cells; Sabine for numerous AAVs; Mr. Ertl for various handiworks that made many of the experiments possible; Michaela and Violetta, for all the help with organizational work and their friendliness; To Andrea Welling, Andrea Lang, Toni, Memo, Selahattin, Sandra, Julia, Karin, Lulu, Regi, and Bernhard.

I owe it to all the people who made the 4 years of my bachelor studies at the University of Tehran a true joy: my friends Marzieh, Sima, Hana, Mehraban, Susan, Bahar and Elnaz; my supervisor Prof. Motamed and my tutor Ms. Minaei, with whom I kicked off the research and wet lab work. To Bahareh and Bahareh, who were by my side during my master studies at NIGEB; For their kind and positive personalities and for giving me a head start in cell culture. A warm thanks to Ms. Shahidi, my biology teacher, for the tiny doodles of eukaryotic cells she drew without being aware of her impact on the fascination that I have for biology today.

Finally, a special thanks to the ones whose presence and support never was and never will be limited to time or distance: my family; Thanks, mom and dad, for your endless love, support and encouragement, from the little red microscope you gifted me when I was 5, up until now; Thanks, Donya and Alborz, for being a continuous source of motivation for me to be a better big sister every day;

And thank you Behdad, simply for being.